Interaction Reconstruction in Digital 3-D CdZnTe Under Various Circumstances

by

Jiawei Xia

A dissertation submitted in partial fulfillment
of the requirements for the degree of
Doctor of Philosophy
(Nuclear Engineering and Radiological Sciences)
in The University of Michigan
2019

Doctoral Committee:

Professor Zhong He, Chair
Professor Igor Jovanovic
Associate Professor Susan Lepri
Dr. Yuefeng Zhu

Jiawei Xia

jiaweix@umich.edu

ORCID iD: 0000-0003-3903-5975

To my family

ACKNOWLEDGEMENTS

First of all, I want to express my deepest gratitude to Prof. Zhong He. Throughout my Ph.D. studies he has always set a high standard in the team and made the best example of hard-working and critical-thinking. Without his guidance and encouragement I would not have made this so far.

I am very thankful to Prof. Jovanovic and Prof. Lepri for being in my thesis committee. They provided invaluable suggestions to me during my thesis formation and studies.

To me, Dr. Yuefeng Zhu was both a great advisor and an outstanding colleague. I could not thank him more for benefiting from working with him on some of the most challenging and interesting experiments.

In the beginning of my studies I was very lucky to have received suggestions and guidance from all the senior team members. Dr. Feng Zhang introduced me to the BNL ASIC systems as well as the logics behind it. To date, our whole group still benefit significantly from his software frameworks. I spent most of my learning time sitting next to Dr. Michael Streicher, and I enjoyed all our discussions and collaborations. I will always be thankful to Dr. Hao Yang and Dr. Jiyang Chu for their suggestions not only in studies but also in life. I am equally thankful to all the other senior members: Jim Berry, Dr. Josh Mann, Dr. William Koehler and Dr. Sean O'Neal. The results presented in this thesis were improved from your help and "grilling" in my studies.

Dr. David Goodman and Dr. Bennett Williams are the best colleagues one could

expect. I was extremely fortunate to have worked for five years with both of them side-by-side. The teamwork, intelligence and creativity they showed will always inspire me.

I am also very thankful to Daniel Shy, Charles Leak, Valerie Nwadeyi, Zhuo Chen, Matthew Petryk and Sara Abraham. Every single critic in all our past discussions made this thesis better.

I want to thank all my friends everywhere in this world for making my life more colorful in the past five years. Some of you were roommates with me while the others were thousands of miles away, yet I could not imagine what it would be without any of you.

Thanks to Haining Zhou specifically, for being a life partner as well as a friend with me. You not only encouraged me through my Ph.D. studies. Every single day, you made me a better person than before.

Last but certainly not least, I am thankful to my parents and all my other family members. Though they have not always been with me in the past yearsw, it was their unanimous support that kept me going.

TABLE OF CONTENTS

LIST OF FIGURES

Figure

LIST OF TABLES

Table

LIST OF ABBREVIATIONS

CdZnTe Cadmium Zinc Telluride

HPGe High Purity Germanium

SNR Signal-to-Noise Ratio

ASIC Application-Specific Integrated Circuit

IDEAS Integrated Detector Electronics AS

BNL Brookhaven National Laboratory

FWHM Full Width at Half Maximum

FPGA Field-Programmable Gate Array

DAQ Data Acquisition

CAR Cathode-to-Anode Signal Amplitude Ratio

SN Side-Neighbor

DN Diagonal-Neighbor

SSE Summed Square Error

MSE Mean Square Error

SRF System Response Function

WPCT Weighting Potential Cross-Talk

STD Standard Deviation

MLE Maximum Likelihood Estimation

EM Expectation Maximization

LET Linear Energy Transfer

SE Single-escape

DE Double-escape

ABSTRACT

Cadmium zinc telluride (CdZnTe) is a semiconductor material that has attracted wide attention in the field of radiation detector in recent years. With the improvements in crystal growth, electrode design and readout electronics, the performance of CdZnTe detectors has been improving and approaching HPGe detectors without the requirements of cryogenic cooling. This work attempts to extend the application of CdZnTe detectors in multiple dimensions by addressing different challenges.

The advancements in digital readout systems enables more accurate information extraction from the CdZnTe detectors. Improvements were made on the measurement of electron mobility-lifetime product in 3-D CdZnTe detectors using more suitable filtering methods.

Though CdZnTe detectors can be operated at room temperature, the front-end devices still need to be temperature-regulated because the electronic gain as well as the electron transport property changes with temperature. The regulation requires extra power consumption, and impedes development of hand-held CdZnTe detector devices. In this work, the effect of temperature change on digital CdZnTe systems was studied in detail. In addition, practical algorithms were developed to correct for the systematic changes with varying temperature in both material and electronics.

Fast neutron damage in high-performance, 3-D sensitive CdZnTe detectors were studied. 3-D CdZnTe detectors showed significant performance degradation after neutron damage. The annealing process of neutron damage was studied both at room temperature and 80 ^{o}C. The annealing was significantly accelerated at higher temperatures. The detectors' performance was recoverable after annealing.

The usage of digital CdZnTe detector systems was extended to measurement of gamma rays in the above-3 MeV range. Pair-production double-escape event peaks were clearly resolved. Resolution degradation mechanisms in 3-D CdZnTe for gamma-ray interactions in this energy range were studied.

An algorithm was developed that estimates the distribution of electron cloud from gamma-ray interactions in digital readout, 3-D CdZnTe detector. Promising results were acquired for muon events which have high signal-to-noise ratio (SNR).

CHAPTER I

Introduction

1.1 CdZnTe Detector

Cadmium zinc telluride, or CdZnTe, is a semiconductor material that has attracted wide attention in the field of radiation detector in recent years. It is also known as a "wide-bandgap" detector because its bandgap of about 1.6 eV, which is much larger than the value of 0.72 eV for high purity germanium (HPGe), a commonly-used semiconductor detector that provides the best performance for the detection of gamma rays up to several MeV. Compared with HPGe detector, a significant advantage of the CdZnTe detector is that it does not require cryogenic cooling. With the improvements in crystal growth, electrode design and readout electronics, the performance of CdZnTe detectors has been improving and approaching HPGe detectors.

1.2 Introductory Shockley Ramo Theorem

The Shockley-Ramo theorem [1–3] is the theoretical foundation behind many semiconductor detectors' electrode designs [4–6], including the pixelated CdZnTe detector that will be introduced in Section 1.3. The theorem states that in a charge-sensitive device, the current i induced on an electrode from the movement of a point charge q

can be calculated by

$$i = q\vec{v} \cdot \overrightarrow{E_0(\vec{x})} \tag{1.1}$$

where $\vec{v}$ represents the velocity of the point charge, and $\overrightarrow{E_0(\vec{x})}$ represents the "weighting field" of the electrode of interest. An "electrode of interest" is defined as the electrode on which one hopes to calculate the induced signal. Equation 1.1 has a counterpart in integral form

$$Q = -q\Delta\varphi_0 \tag{1.2}$$

where Q represents the induced charge on the electrode, and $\Delta(\varphi_0)$ represents the change of "weighting potential" when the point charge moves from the initial location to the end location:

$$\Delta(\varphi_0) = \varphi_0(\vec{x_1}) - \varphi_0(\vec{x_0}). \tag{1.3}$$

It should be noted that in Equation 1.1 and Equation 1.2, only the velocity $\vec{v}$ is related to the actual electric field in the device. The weighting field $E_0(\vec{x})$ and weighting potential $\varphi_0(\vec{x_0})$ are not the true electric field or potential applied on the device. Instead, they are only affected by the geometrical layout of electrodes, and the dielectric constant of the material between the electrodes. This implies that when a point charge drifts in a charge-sensitive radiation detector, one could easily calculate the induced signal amplitude (i.e. Q), without knowing the exact electric field that affects the path of the charge. In a radiation detector with isotropic material, the weighting potential for the electrode of interest can be calculated by solving the Poisson equation [3]

$$\nabla^2\varphi_0 = 0 \tag{1.4}$$

with boundary conditions that (1) the weighting potential on the electrode of interest is unit 1 and (2) the weighting potentials on all other electrodes are zero.

In reality, a radiation interaction deposits energies and generates one or more "clouds" of charge carrier, instead of a point charge. However, based on superposition principle, the clouds can be divided into many point charges. The signal for each point charge can be calculated and summed together as the result from the cloud of charges [3]. It needs to be emphasized that although the total induced charge can be calculated conveniently using the Shockley-Ramo theorem, the actual induced waveform on an electrode is still affected by the velocity of the charge. To predict the expected waveform, instead of the signal amplitude from the drift of a point charge, one needs to combine the weighting potential profiles calculated from Equation 1.4, and the actual electric field in the detector.

1.3 3-D CdZnTe Detector

One of the biggest challenges in the development of CdZnTe detectors is that the mobility-lifetime products of electrons and holes in CdZnTe are drastically different from each other [7]. Electrons in CdZnTe drift at a speed of about two orders of magnitude larger than holes. Using the conventional planar electrodes design, it is very challenging to fully collect signal amplitudes from the drift of both electrons and holes.

Different modifications were made to the electrodes in CdZnTe detectors to make the induced signals easier for subsequent readout and processing. These modifications include coplanar grid [8, 9], virtual Frisch grid [10] and pixelated anodes [11]. All the modifications were indented to make the induced signal on the anode almost independent of the position of interaction. These detectors are also referred to as "single-polarity" sensing detectors. The pixelated CdZnTe detectors are the focus of work in this thesis and will be described in detail.

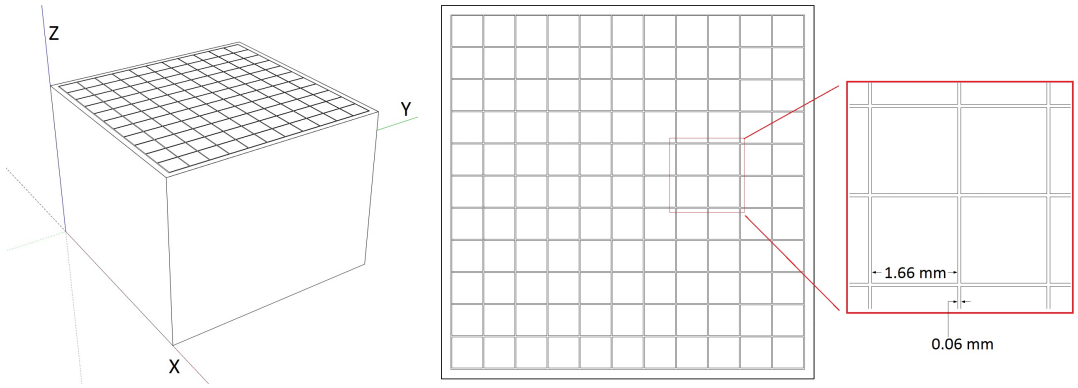

(a) 3-D view. (b) Top view.

Figure 1.1: Simplified scheme of a pixelated CdZnTe detector and its anode electrodes.

Figure 1.1 shows the scheme of a pixelated CdZnTe detector commonly used at the University of Michigan. Its size is $2 \times 2 \times 1.5\,\mathrm{cm}^3$. The detector has one common planar cathode, and 121 anode pixels arranged in a 11 × 11 array. The distance between the centers of two adjacent anode pixels, also known as the "pixel pitch", is 1.72 cm. A 60-µm gap exists between each pair of adjacent pixels. A guard ring with 500 µm width surrounds the peripheral pixels to regulate the electric field in the peripheral region. Most of these detectors are manufactured by Redlen Technologies [12]. In operation, the cathode electrode is usually biased at -3000 V while the anodes are at zero bias. A bias difference lower than 3000 V is undesirable as it causes more electrons to get trapped as they drift towards the collecting anode. On the other hand, higher voltage difference poses more challenges in the design of electronics. In subsequent discussions, all the CdZnTe detectors are operated with -3000 V on the cathode, unless declared otherwise. In subsequent discussions, the Z-axis direction is always used to represent the "depth" direction, unless declared otherwise.

The size of $2 \times 2 \times 1.5\,\mathrm{cm}^3$ is considered "large-volume" for CdZnTe detectors because of the difficulties in crystal growth. Prior to the "standard" shown in Figure 1.1, the University of Michigan used to work with $1 \times 1 \times 1\,\mathrm{cm}^3$, $1.5 \times 1.5 \times 1\,\mathrm{cm}^3$, $2 \times 2 \times 0.5\,\mathrm{cm}^3$ and $2 \times 2 \times 1\,\mathrm{cm}^3$ detectors [13]. The large-volume, high-quality

and affordable crystals were made possible by the development of travelling heater method [14]. In addition to the size of the detector, the electrode design was also improved over the years.

The pixelated anode design for CdZnTe detectors has several advantages over the other single-polarity charge sensing semiconductor detectors. First, the leakage current and capacitance on each anode are small, as a result the electronic noise in each anode channel is limited. Second, signals read from an anode pixel can only come from the material over that anode. Hence, the channel number of the anode implicitly carries the position information in X- and Y-axes directions. In subsequent reconstructions, potential non-uniformity of the detector's response can be corrected to a precision no worse than the pixel pitch. In addition, multiple interactions taking place at the same time in the same detector under different pixels can be reconstructed. This provides an advantage in pixelated CdZnTe detector for Compton imaging [15].

Using the Shockley-Ramo theorem, the weighting potential profile for each electrode can be calculated. In this study, the weighting potentials are calculated using ANSYS Maxwell [16]. Figure 1.2 presents a cross-sectional view of the weighting potential when the anode pixel in the center of the detector is the electrode of interest. The spatial resolution of the calculation is 0.2 mm.

The most interesting observation in Figure 1.2 is that the weighting potential is almost always zero, except for regions very close to the anode pixel of interest. This phenomenon is also called "small pixel effect" [17]. The weighting potential when the cathode is of interest can also be calculated. In Figure 1.2, a line $x = 10$ mm is drawn. The weighting potentials along this line are compared and shown in Figure 1.3 when the center anode and the cathode are of interest, respectively.

Since holes move much more slowly than electrons in CdZnTe, the induced signals on the electrodes can neglect the contribution of hole movements. This assumption is

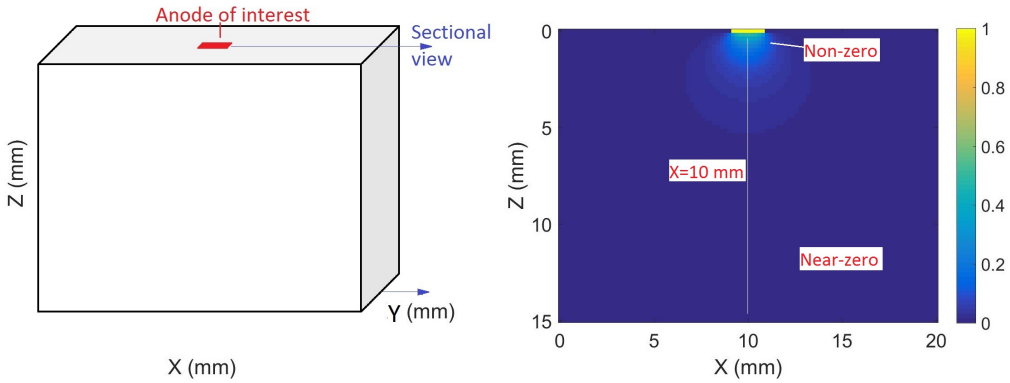

Figure 1.2: Sectional view of weighting potential when the center anode pixel is of interest. The location of the anode of interest is highlighted in the left plot.

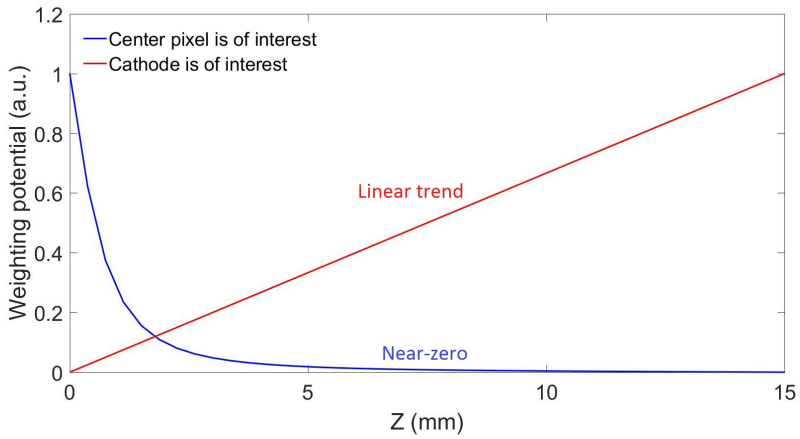

Figure 1.3: Weighting potential calculated when the center anode pixel and the cathode are of interest respectively. The weighting potentials along the $x = 10$ mm line in Figure 1.2 are shown.

used throughout this thesis unless stated otherwise. Assuming radiation interactions generate electron clouds with negligible sizes, and the clouds always drift perpendicularly towards the collecting anodes with a constant speed, the expected signal waveform as a function of depth can be easily predicted based on the calculated weighting potential profiles. In an event with a single interaction, the cathode signal will have a constant slope. On the other hand, the collecting anode's signal almost does not change when the electrons are drifting in the bulk of the detector, until when the electrons are very close to the collecting anode, and the anode signal will increase drastically. Examples of the measured waveforms will be shown in Chapter II.

The small pixel effect is one of the methods that enable the depth-sensing techniques. As will be discussed in Chapter II, both timing and amplitude information can be used to estimate the depth of detected radiation interactions. The estimated depth, combined with the X- and Y-axes positions encoded in the anode channel number, enabled the 3-D position sensing of every interaction. This technique is called "3-D position sensing technique". Pixelated CdZnTe detectors combined with this technique are called "3-D position sensitive CdZnTe detectors", or "3-D CdZnTe" for short.

In addition to signals in the collecting anode, signals in non-collecting anodes also carry very useful information. Figure 1.4 presents the weighting potential values along several lines which are in parallel with the Z-axis direction, located in an adjacent anode pixel. One could imagine if a negative unit point charge is generated on the cathode surface and drifts along one of these lines at a constant speed, a signal with shape and amplitude similar to the corresponding weighting potential values in Figure 1.4 will be induced in the anode of interest, even if it does not ultimately collect any charge. Such signals are called "transient signals" [18]. The transient signals carry useful information about the lateral position of the electron clouds. The "sub-pixel sensing technique" that estimates the lateral position of interactions based on the

transient signals will be introduced in 2.2.

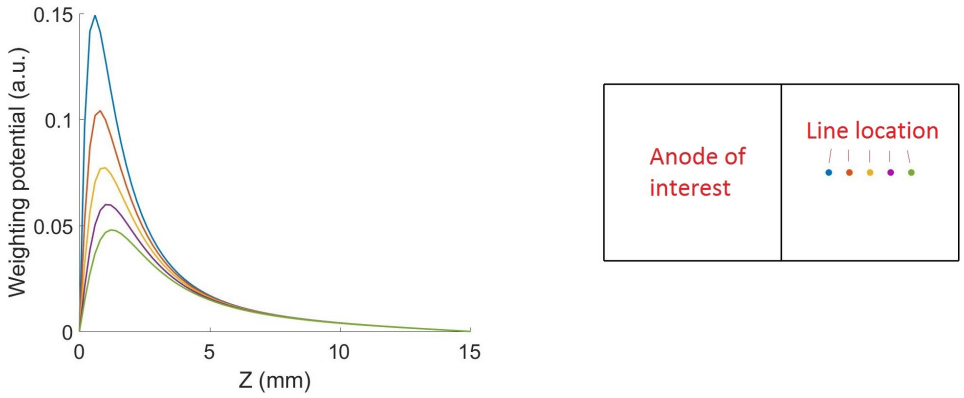

Figure 1.4: Weighting potential in the anode of interest along perpendicular lines at different locations in an adjacent pixel.

1.4 Overview in This Work

In this work, improvements and developments of reconstruction algorithms are made for radiation interaction detection and measurement in 3-D CdZnTe detectors, using digital readout systems. Chapter II gives a brief introduction to the digital readout system. It also describes the algorithms used to process the waveforms, as well as subsequent events reconstruction algorithms that were developed previously.

The digital readout system reads out waveforms that allow flexible processing methods. Chapter III discusses an improvement made on the measurement of electron mobility-lifetime product in 3-D CdZnTe detectors using the digital readout system.

Though CdZnTe detectors can be operated at room temperature, the front-end devices still need to be temperature-regulated because the electronic gain as well as the electron transport property change with temperature. The regulation requires extra power consumption, and impedes development of hand-held CdZnTe detector devices. Chapter IV describes experiments that study the effect of temperature change on digital CdZnTe systems in detail. In addition, practical algorithms are developed to correct for the systematic changes with varying temperature in both material and

electronics.

Fast neutron damage in high-performance, 3-D sensitive CdZnTe detectors were studied with multiple experiments. The annealing process of neutron damage was studied both at room temperature and 80 ^{o}C. The results are shown in Chapter V.

Multi-MeV gamma-ray interactions in CdZnTe detectors are becoming more and more interesting thanks to improvements in CdZnTe crystal volume. Chapter VI describes experiments using digital CdZnTe detector systems to measure gamma rays in the range of 3 to 7 MeV. Resolution degradation mechanisms for gamma-ray interactions in this energy range are studied.

Compared to analog systems, the digital CdZnTe detector systems read out waveforms that carry very rich information. Chapter VII describes the development of an algorithm that estimates the distribution of electron cloud from gamma-ray interactions in digital readout, 3-D CdZnTe detector. Promising results were acquired for muon events which have high signal-to-noise ratio (SNR).

CHAPTER II

Digital CdZnTe Detectors and Event Reconstruction

2.1 Digital Readout System

2.1.1 VAD_UM ASICs

A challenge for pixelated CdZnTe detector development is that each anode pixel reqiures one ASIC or electronic channel to read out signals. At University of Michigan, Application-Specific Integrated Circuits (ASICs) are developed and used to read out signals in pixelated CdZnTe detectors. Compared to general-purpose electronics, ASICs usually demonstrate greater functionality, including faster speed, less space and weight requirements, and lower power consumption. However, the design and development of ASICs are very expensive and time consuming.

Over the past twenty years, several generations of ASICs have been developed by University of Michigan. These ASICs share some common features. Each ASIC has 128 anode channels to read out the signals from all the 121 anode pixels in the detector, and a cathode channel to read out signals from the cathode electrode. In 1998, the first ASIC readout system for pixelated CdZnTe was delivered. The system demonstrated 1.75% FWHM energy resolution for single-pixel events at 662 keV [19]. The ASICs, named VAS series, were developed by the collaboration between

University of Michigan and Integrated Detector Electronics AS (IDEAS) [20]. In subsequent developments, the electronic noise of the ASICs was decreased and below-0.8% FWHM single-pixel events resolution at 662 keV was achieved [21–23]. In the meantime, the University of Michigan also collaborated with Brookhaven National Laboratory (BNL) and developed BNL-H3D ASICs. Systems composed of these ASICs demonstrated below-0.5% FWHM resolution for single-pixel events at 662 keV [24].

The ASICs mentioned above are "analog ASICs" because they have on-board shapers following the pre-amplifier for each channel. Signals from pre-amplifiers are filtered by these shapers and only limited information such as amplitude and timing of trigger is read out by subsequent electronics. Limited information hindered further analyses of the signals, as well as the development of event reconstruction. In recent years, the University of Michigan started to collaborate with both IDEAS and BNL to develop next generation, digital readout ASICs. The collaboration between the University of Michigan and IDEAS delivered the VAD_UM ASICs. These ASICs showed about 0.4% FWHM resolution for 662 keV, single-pixel events. In latest developments, the latest version, VAD_UM v2.2 ASICs, were directly connected to Redlen $2\times2\times1.5\text{cm}^3$ CdZnTe detectors to reduce the input capacitance. The electronic noise was reduced to about 1.5 keV (equivalent FWHM). With this very low electronic noise, the single-pixel events reached 0.35% FWHM resolution at 661.7 keV [13]. In addition to reduced electronic noise, the VAD_UM v2.2 ASICs can also work in four dynamic ranges: 700 keV, 3 MeV, 7 MeV and 9 MeV. A larger dynamic range comes with a price of increased electronic noise due to the reduction of electronic gain, thus signal-to-noise ratio. In this chapter, energy resolution achieved on VAD_UM ASICs used 700 keV dynamic range, unless stated otherwise. For simplicity, each pair of connected ASIC and CdZnTe detector is referred to as a CdZnTe module hereafter. If a module uses directly-attached ASIC and detector, it is referred to as a direct-

attachment module. Otherwise, the module is referred to as a standard-attachment module. Figure 2.1 presents an image of VAD_UM ASIC modules, with and without CdZnTe detectors attached. Figure 2.2 compares the measured average anode electronic noise on a direct-attachment module and a standard-attachment module in different dynamic ranges. Both detectors were biased to -3000 V on the cathode. The noise was measured as 2.35 times the standard deviation of the preamplifier baseline in each anode channel. It should be noted that two different CdZnTe detectors were used because the crystal is permanently connected in a direct-attachment module.

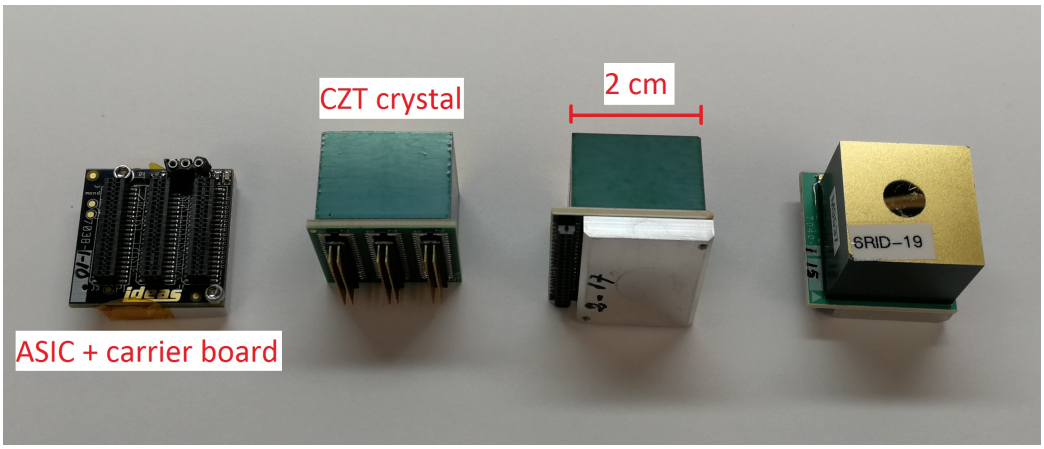

Figure 2.1: Left to right: a VAD_UM ASIC with the carrier board, a $2 \times 2 \times 1.5$ CdZnTe detector, a direct-attachment module side view and a direct-attachment module top view. Each ASIC is connected to a carrier board.

Most work discussed in this thesis is based on systems developed with the VAD_UM ASICs. One or more ASICs are configured by a field-programmable gate array (FPGA), which is controlled by a data acquisition (DAQ) computer. Each set of CdZnTe detectors, VAD_UM ASICs, FPGA and subsequent readout electronics is called a digital CdZnTe system. Examples of some digital CdZnTe systems will be introduced in 2.1.2.

The VAD_UM ASICs do not use shapers to extract information from the signals. Instead, digitized waveforms after pre-amplifiers are directly read out from the systems. In operation, each channel has 160 sample cells constantly sampling and storing

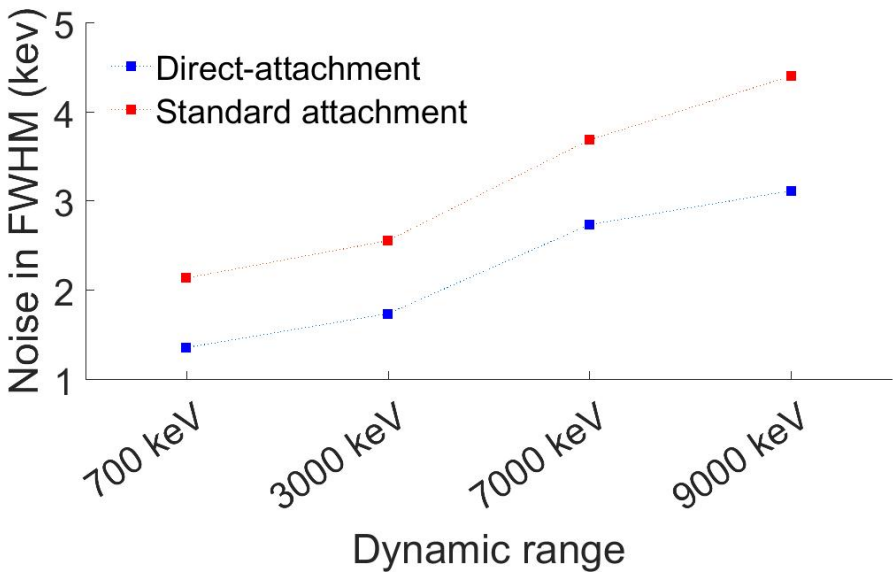

Figure 2.2: Average anode channel noise in each dynamic range setting on two different detectors.

the signal on a rotational basis. The sampling frequency could be set to 10, 20, 40 or 80 MHz. Hence, the maximum sampling window is 16 µs for each channel. With these waveforms read out, sophisticated analyses and reconstruction algorithms can be carried out.

The VAD_UM ASIC can be operated on two different modes: forced readout mode and triggered readout mode. In forced readout mode, cell samples from the channels are periodically read out, regardless of radiation interactions in the detector system. This mode is usually needed for electronic noise measurement, baseline measurement or other debugging purposes.

In triggered readout mode, the cell samples are read out only when the system is triggered by radiation interactions. Though VAD_UM ASICs do not use shapers to extract information, they still compare shaped waveforms with a user-set threshold. When a shaped waveform exceeds the threshold, a trigger signal is sent to the FPGA. Within a user-set "delay time", the readout is started. The triggered readout mode can be further divided into triggered only, triggered + 4 and triggered + 8 modes.

Cathode waveform is always read out in the three modes and the difference lies in how many anode channels are read out. In triggered only mode, waveforms from only the triggered anodes are read out. In triggered + 4 mode, waveforms from each triggered anode as well as the four anode pixels adjacent to the triggered anode are read out. In triggered + 8 mode, waveforms from each triggered anode as well as the eight anode pixels surrounding the triggered anode are read out. Waveforms from an example single-pixel, trigger + 8 event are presented in Figure 2.3. Triggered readout mode with more neighbor pixels read out deliver more information. However, this usually comes with a price of increased storage space and higher dead time fraction [25] in the measurement. For each anode pixel, the four adjacent pixels are called side-neighbor (SN) pixels, while the other four pixels sharing corners with the center pixel anode are called diagonal-neighbor (DN) pixels.

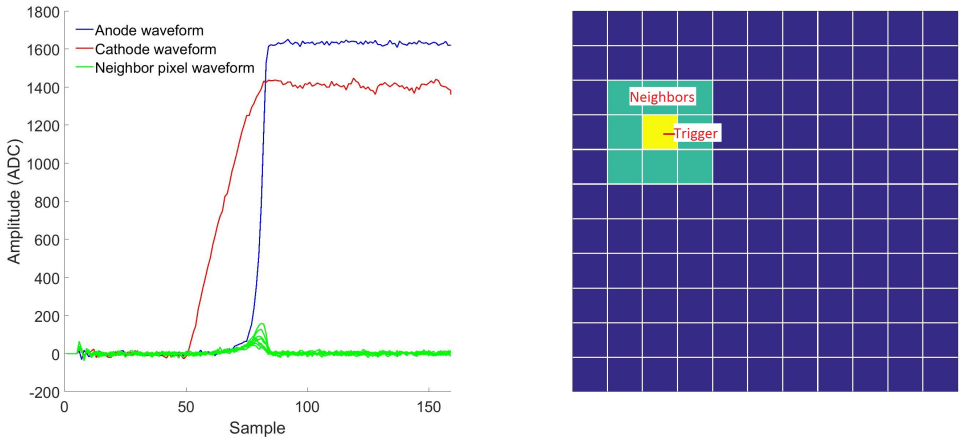

Figure 2.3: (Left) Example waveforms from a single-pixel event in trigger + 8 mode. (Right) Corresponding map of triggered and neighbor pixels colored in yellow and green.

2.1.2 Digital CdZnTe Systems

Two types of digital CdZnTe systems were used in the work discussed in this thesis: VAD_UM systems, and Orion systems.

Both the VAD_UM system and the Orion system can house up to a 3×3 ar-

ray of modules using VAD_UM v2.2 ASICs. The VAD_UM system can house either standard-attachment or direct-attachment modules. The readout electronics in this system are designed by IDEAS. Figure 2.4 presents an image of a VAD_UM system. The motherboard has three sets of receivers and analog-to-digital converters (ADCs), and each set reads out signals from three CdZnTe modules. The Zed board is used to buffer and communicate signals between the motherboard and the DAQ computer. The high-voltage (HV) distribution board applies up to -3000 V to the planar cathode of each CdZnTe detector. In operation, the chamber containing the modules is closed and sealed. A combination of fan and Peltier is used to regulate the ambient temperature in the chamber. The VAD_UM system consumes a large space (more than half a meter in length), and requires several external bias supplies for the motherboard, Zed board, Peltier and high voltage.

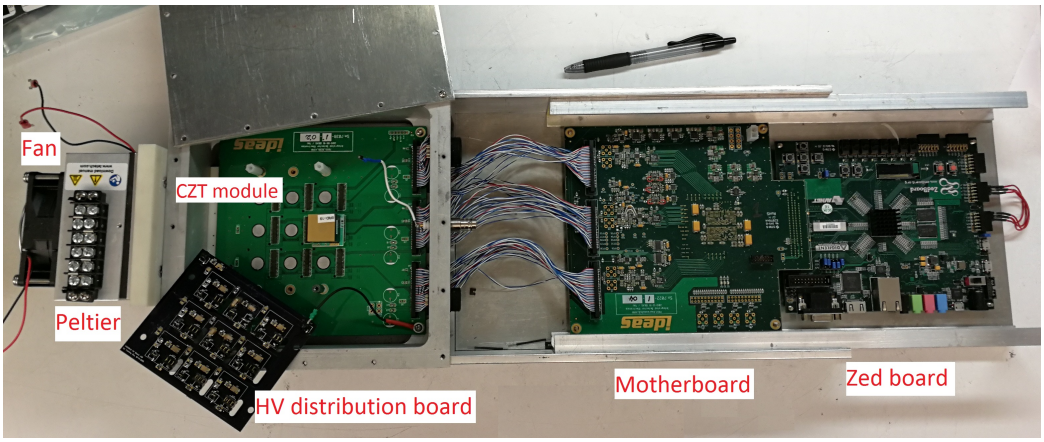

Figure 2.4: Image of the VAD_UM system. Only one CdZnTe module is seeded. A pen is used for scale.

The Orion systems were developed by Dr. Yuefeng Zhu at University of Michigan. It compresses the electronics components together and only requires a 12 V power supply. All the biases are generated on-board. With these advances, the system is almost hand-held. The Orion systems used identical components and are named Orion-α, Orion-β, etc for distinguishment. An image of the Orion-β system is presented in Figure 2.5. These systems have demonstrated 0.35% FWHM energy resolution for

662 keV, for single-pixel events from all nine modules.

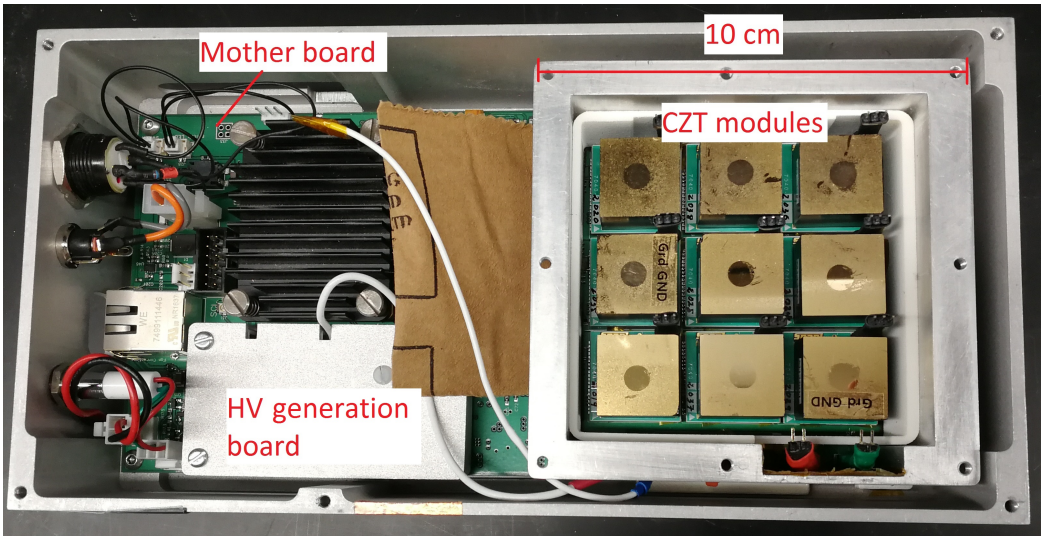

Figure 2.5: Image of the Orion-β system.

2.2 Waveform Processing

As discussed in Section 2.1, digitized waveforms are read out from the cell samples in a digital CdZnTe system. However, each amplitude from a cell sample does not just contain the true signal from a radiation interaction. It also contains the noise, and the baseline value in that cell. A sample from a cell can be modelled as

$$s'_i = s_i + c_i + n_i \tag{2.1}$$

where s'_i represents the sample, s_i represents the true signal amplitude, c_i represents the baseline value for the i-th cell sample in a channel, and n_i represents the random noise. To measure the true signals, the cell baseline values must be measured and subtracted.

The measurement of cell baseline is referred to as "cell calibration" hereafter. In this process, a VAD_UM ASIC is configured to work in forced readout mode and constantly reads out digitized waveforms in every channel. A number of samples are

accumulated for each cell in each channel. Assuming no true signals are present in the process, the average value for samples in each cell is expected to approximate the true cell baseline, based on the Law of Large Numbers [26]. In practice, it was found that 10000 samples for each cell can provide an accurate estimation of the cell baseline. Figure 2.6 presents an example of the calibration for one cell.

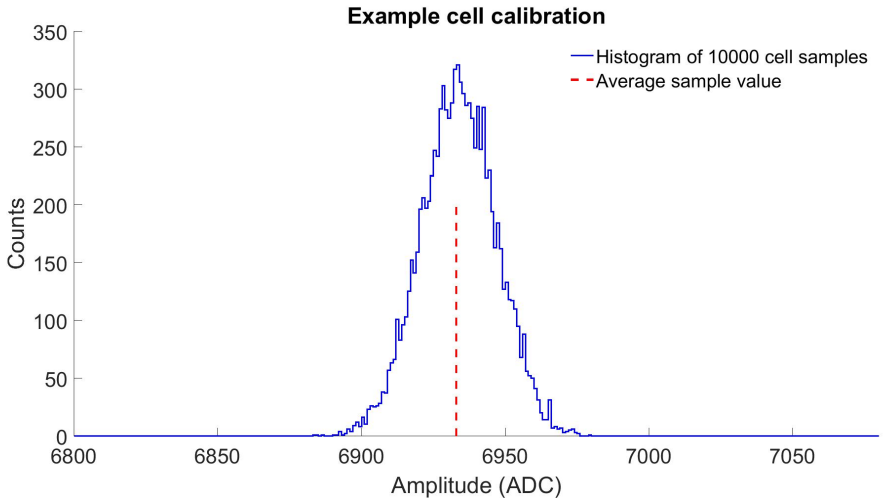

Figure 2.6: Example histogram of 10000 samples from one cell. The average of the samples is also shown by a red dashed line.

The cell baseline values from cell calibration are subtracted from the waveforms on an event-by-event basis. As mentioned in 2.1, the signal in each channel is sampled and stored on a rotational basis until a trigger happens. Since the trigger can happen at any time, the measured waveform on a channel in operation should be modelled as

$$\vec{s'} = \vec{s} + \vec{c_\tau} + \vec{n} + a\vec{1} \tag{2.2}$$

where $\vec{s}$ and $\vec{s'}$ represent the true signal and measured signal respectively, $\vec{n}$ represents the noise, and $\vec{c_\tau}$ represents the cell baselines in that channel with a cyclic offset τ. This equation is different from Equation 2.1 in that a vector with a constant value $a\vec{1}$ is added. Because of leakage current, interference and relatively long pre-amplifier

decay time constant, low-frequency variations are expected in waveforms from all the channels. Since this variation's frequency is usually much longer than the sampling window, its contribution to the signal can be approximated as a contant value for all recorded cell samples in each channel. For each waveform, the value of a is estimated by taking the average of the initial 40 samples, then subtracted from the original waveform. In triggered readout mode, the "delay time" of the ASIC ensures that these samples in the beginning of each waveform do not carry true signals, hence the estimation is unbiased. Unless stated otherwise, this constant part in each waveform is neglected hereafter.

The value of τ is a random number, ranging from 0 to 159 because the trigger can happen at any time. To determine the value of τ, a "reference channel" is read out each time a trigger happens. This channel is not connected to an electrode and does not carry any true signals. The measured waveform from this channel is compared with the cell baseline values for the same channel, with the value of τ incremented iteratively from 0 to 159. In each iteration, the summed square error (SSE) is recorded and the τ value with the smallest SSE ($\tilde{\tau}$) is regarded as the true cyclic time offset. The design of the ASIC ensures that the channels are synchronized, hence the true time offset $\tilde{\tau}$ is the same for all channels. In each channel, the cell baselines with cyclic offset $\tilde{\tau}$ are subtracted from the waveform to acquire the cell-calibration-corrected waveform. Figure 2.7 presents an example waveform with and without cell calibration correction. It could be seen that the cell calibration largely reduces the variations in the waveform and the result is very smooth. It should be noted that the sampling frequency of the waveform is 40 MHz. All the measurements in this thesis used this sampling frequency, unless stated otherwise.

As will be discussed in 2.3, position and energy of each radiation interaction in pixelated CdZnTe detectors rely on two types of inputs: amplitude and timing of trigger in each waveform (including the anodes and cathode). Zhu developed and

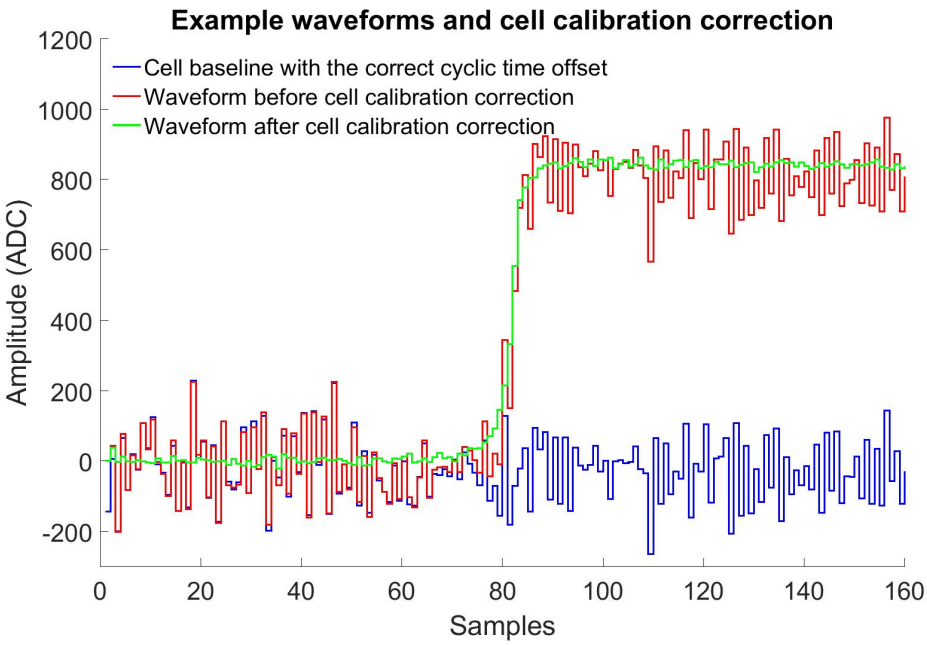

Figure 2.7: Example waveform before and after correction using cell calibration. The cell baselines with the correct cyclic time offset are also presented.

optimized three different methods to extract the information: digital filtering, simple subtraction and system response function (SRF) fitting [18]. For simplicity, timing of trigger is referred to as timing hereafter. The advantages and disadvantages of the three methods are compared in the following sections.

2.2.1 Digital Filtering

The signal amplitude for a waveform can be extracted by feeding the waveform through a digital filter, and looking for the maximum value in the output. This method is very similar to the analog ASICs, however the filter can be chosen arbitrarily and optimized by the user. Zhu found that trapezoidal filters have the best performance for waveforms from pixelated CdZnTe detectors [18]. The name "trapezoidal filter" comes from the fact that the step function response from this filter is a trapezoid. Figure 2.8 presents the impulse response and step function response from the trapezoidal function commonly used for anode channel waveforms in pixelated

CdZnTe detectors. Both the rising and falling edges of the trapezoid are 1600 ns in length, and the top stage lasts 400 ns. It should be noted though the maximum value in the presented step function response is 1, this gain could be set arbitrarily as long as the same filter is applied to all the anode channels. The two responses for the cathode channel are presented in Figure 2.9. It could be seen that the time lengths for the rising edge, falling edge and top stage are changed to 1400 ns, 1400 ns and 800 ns. Figure 2.10 presents the anode and cathode waveforms in a single-pixel event and the estimated waveform amplitudes from trapezoid filters.

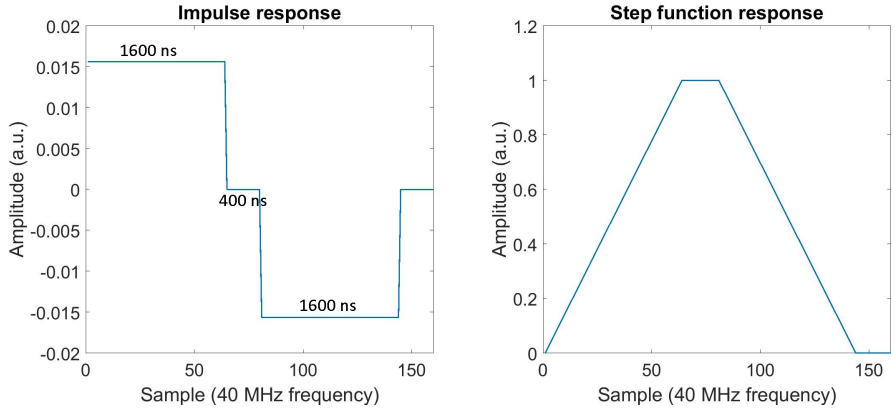

Figure 2.8: Impulse and step function response of default anode channel trapezoidal filter.

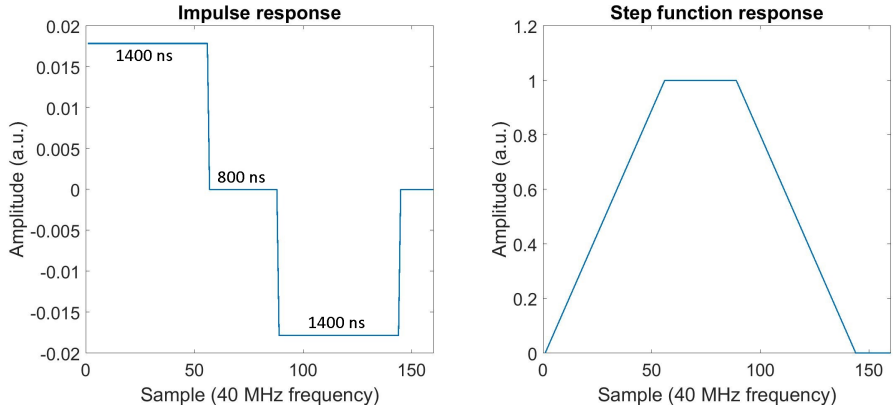

Figure 2.9: Impulse and step function response of default cathode channel trapezoidal filter.

The timing of each waveform can also be determined by digital filter shaping.

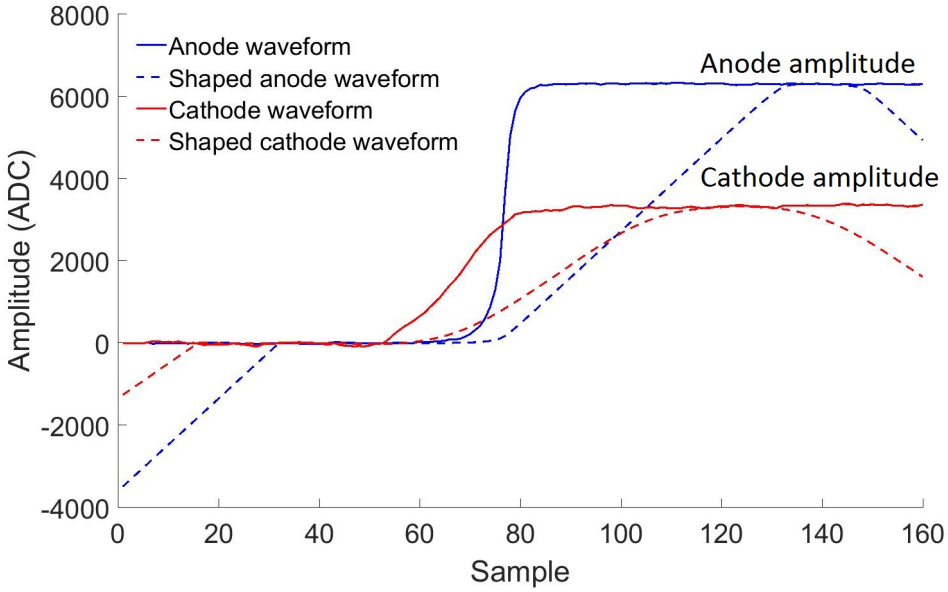

Figure 2.10: Single-pixel event waveform amplitude estimation by trapezoidal filter.

The shaping time constants of filters intended to determine timing are usually much shorter than those intended to determine depths. Zhu's studies showed that in pixelated CdZnTe detectors, CR-RC^4 filters with shaping time constants of 100 and 250 ns for the anode and cathode channels show the best performance [18]. In each shaped waveform, the timing is determined by looking for the sample that surpasses 50% of the maximum value in the waveform. Figure 2.11 presents the process of timing determination for the same single-pixel event that is shown in Figure 2.10.

Ideally, the timing for the waveforms, especially the cathode waveforms, should be determined by detecting the beginning of the rising edges. By definition, 10% of the maximum waveform amplitude should be more accurate than 50% of the maximum amplitude in determining the cathode timing. However, in reality, noise can play a non-negligible role. A low threshold makes the timing detection error-prone, especially for low-energy, or near-anode interactions. In these interactions the cathode waveform amplitudes are very small. For example, Figure 2.12 presents the detected cathode-to-anode waveform timing difference spectra in single-pixel events from a measurement

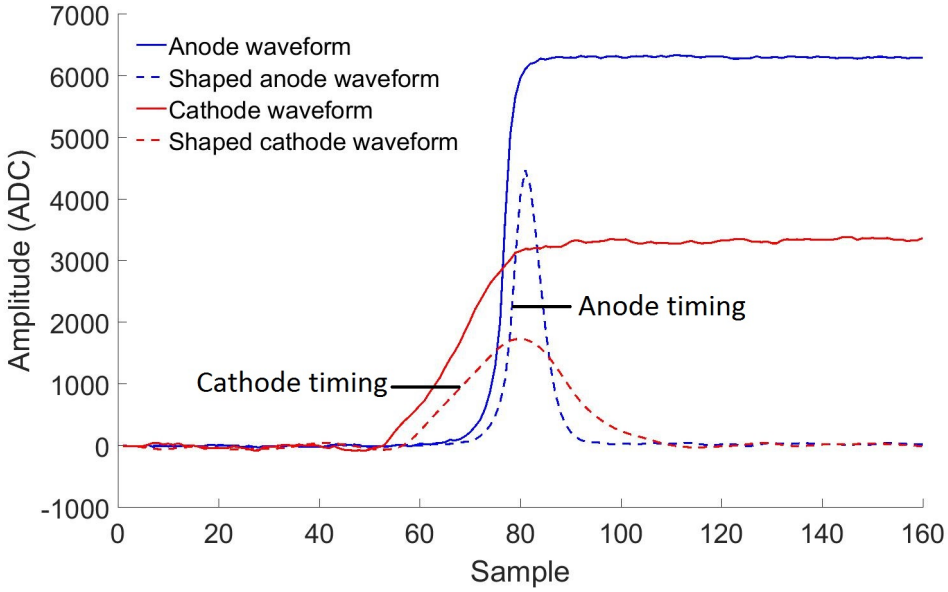

Figure 2.11: Single-pixel event waveform timing estimation by CR-RC^4 filter.

of a ^{137}Cs source. The dynamic range was 700 keV. When 10% maximum amplitude threshold is used, about 20% of the single-pixel events can be lost due to incorrect cathode timing detection. In contrast, with 50% relative threshold, the lost events number due to incorrect cathode timing is negligible.

An alternative method to determine the waveform timing is by waveform shape fitting. This method is more accurate and discussed in detail in Section 2.2.3.

2.2.2 Simple Subtraction

A main drawback of trapezoidal filter is that transient signals due to weighting potential cross-talk can cause non-negligible errors in amplitude estimation. As discussed in Chapter I, transient signals appear in SN and DN anode pixels of the collecting pixel. In two- or more-pixel events, many events can have one or more pairs of SN pixels triggered at the same time, mostly due to charge sharing. As Figure 2.13 presents, estimated signal amplitudes from digital filters can be biased due to these transient signals.

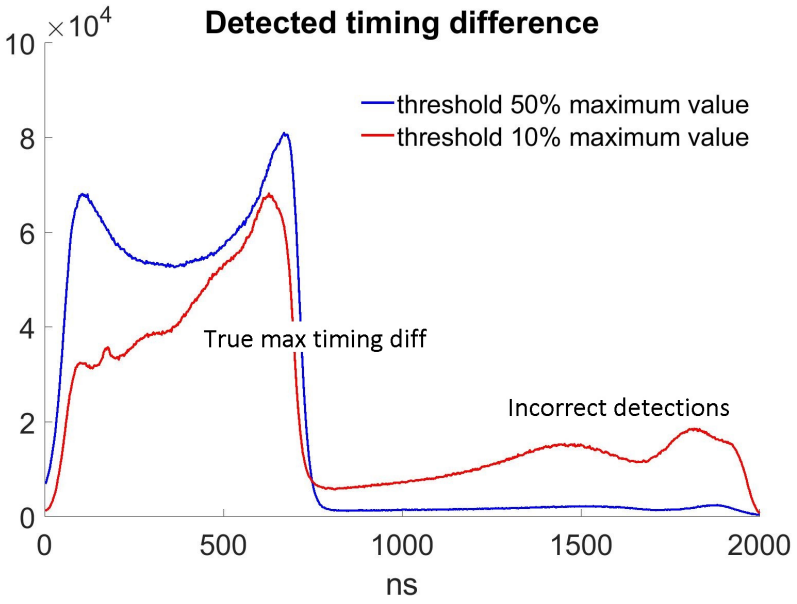

Figure 2.12: Single-pixel event cathode-to-anode signal timing difference detected using different thresholds. The maximum timing difference is about 750 ns. Values larger than this are due to incorrect timing detection.

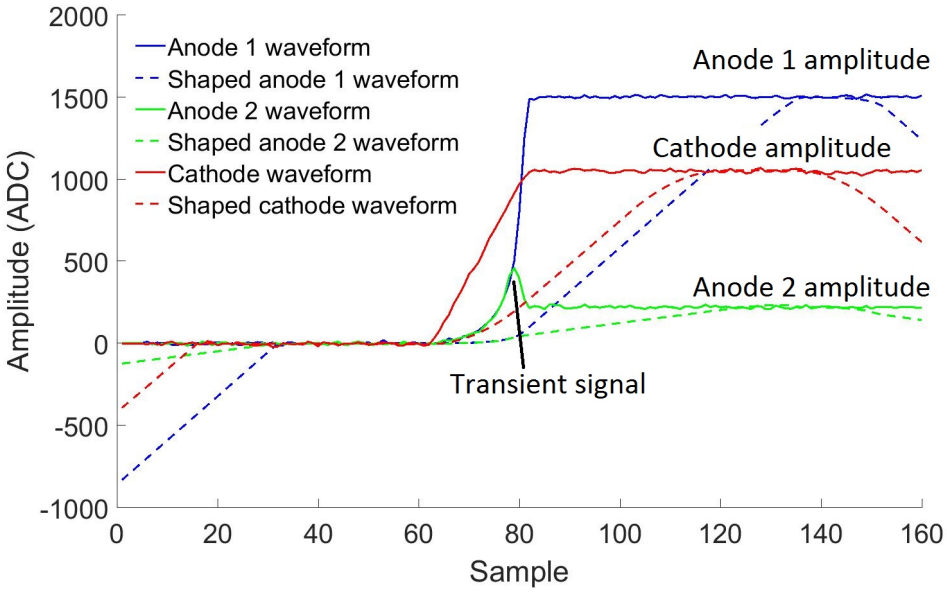

Figure 2.13: Two-pixel event waveform amplitude estimation by trapezoidal filter. In this example, a very strong transient signal is observed in anode 2 and the estimated amplitude is affected.

The simple subtraction method is more advantageous for multi-pixel events with SN pixel pairs. This method is named "simple-subtraction" because the signal amplitude for each waveform is determined by taking the difference between the average values in the "tail region" and "baseline region". The two regions can be arbitrarily chosen by the user. By default, the baseline and tail regions for an anode waveform are the 3-rd to the 61-th samples, and the 120-th to the 158-th samples, respectively. For a cathode waveform, the default tail and baseline regions are the 3-rd to the 21-th samples, and the 120-th to the 158-th samples. Figure 2.14 presents the process of amplitudes measurement using simple subtraction with the default tail and baseline regions settings. The waveforms are the same as those in Figure 2.13. Because the "rising edges" in the waveforms are not included in either the tail or the baseline region, the amplitudes are more accurately measured.

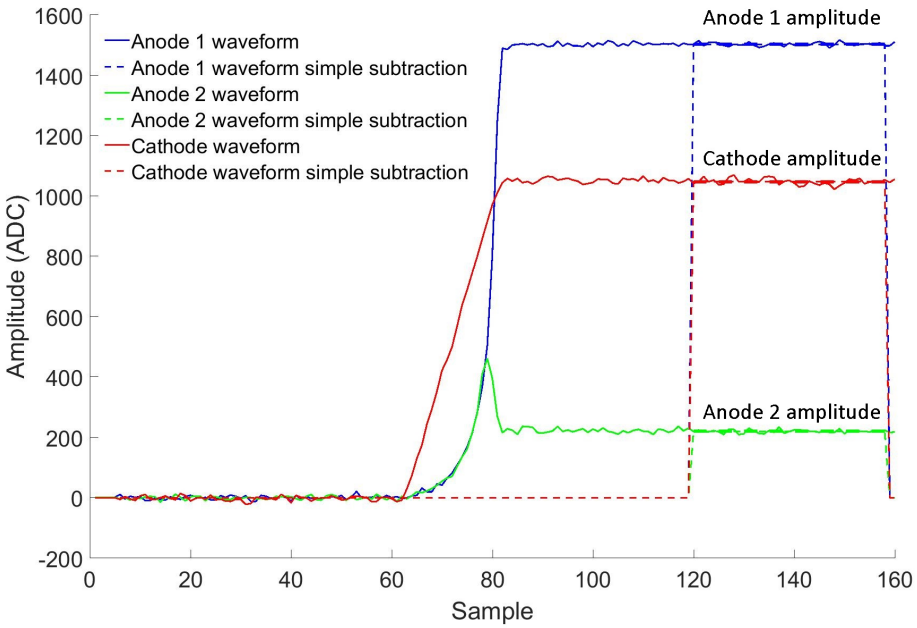

Figure 2.14: Two-pixel event waveform amplitude estimation by simple subtraction. In this example, a very strong transient signal is observed in anode 2, but the estimated amplitude is not affected.

It should be noted the default tail and baseline regions settings are optimized for waveforms from a $2 \times 2 \times 1.5\text{cm}^3$ CdZnTe detector, with the cathode biased at -3000

V and read out with 40 MHz sampling frequency. The lengths of tail and baseline regions should be as long as possible to improve the precision of the mean values, but not too long to avoid including any true signal and decrease the accuracy. If the detector material, thickness, electric field or sampling frequency changes, the optimal tail and baseline regions will need to be adjusted accordingly.

Simple subtraction works better for multi-pixel events with SN pixel pairs. However, for other multi-pixel events, simple subtraction is usually worse than trapezoidal filter. These events are mostly Compton scatter or pair-production events, instead of charge sharing events. As a result, the true timing of each anode waveform differs from each other. An example two-pixel event with different true timings in the anodes is given in Figure 2.15. As Figure 2.16 shows, pixelated CdZnTe anode waveforms have "slow turning" due to de-trapping [18]. In addition, pre-amplifier decay can cause a small, negative slope in the tail region. In simple subtraction, these two issues can cause deficit of estimated amplitude. This deficit is a function of the relative relationship (in time) between the tail region sampling window and the true timing of the anode waveform. In events similar to that in Figure 2.15, the two anode waveforms have different true timings. A universal tail region sampling window has different time difference compared to the two anode waveforms. As a result, the relative deficits in amplitude will be different in the estimated amplitudes for the two anode waveforms. This poses a challenge for subsequent events energy reconstructions.

2.2.3 System Response Function Fitting

SRF fitting has good performance for all multi-pixel events, regardless of whether or not SN pixel pairs are present. In addition, it also provides the most accurate definition of timing information compared to digital shaping. It achieves the optimal performance by dynamically "aligning" the tail region sampling window to the estimated timing of each anode waveform on an event-by-event basis. The alignment is

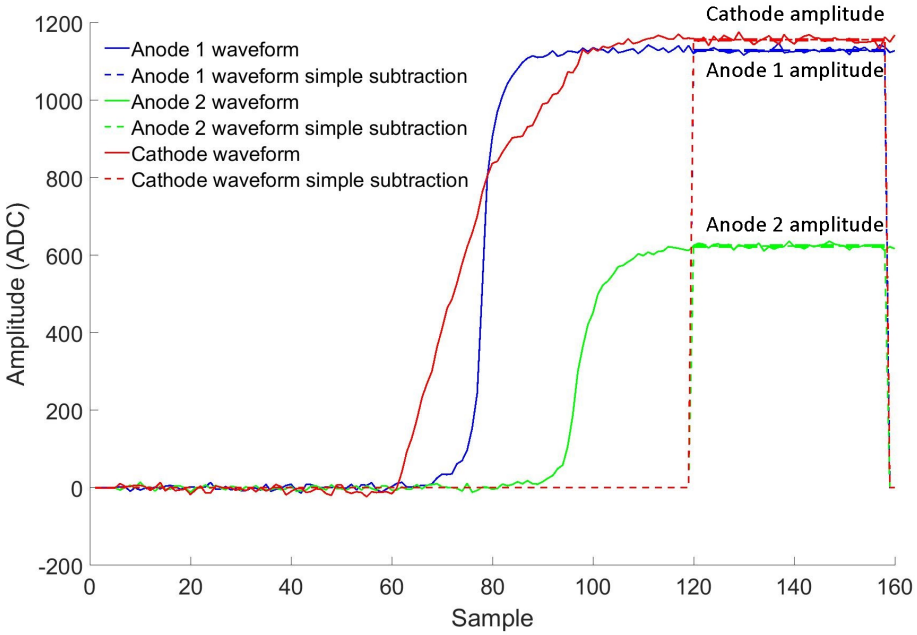

Figure 2.15: Two-pixel event waveform amplitude estimation by simple subtraction. In this example, the same simple subtraction sampling window is applied to two anode waveforms with different timings.

done by looking for the best "fit" of SRFs to the measured waveforms.

SRF is measured by taking the average of 661.7 keV, single-pixel, photoelectric interaction event waveforms from every voxel in a pixelated CdZnTe detector. A voxel is a 3-D cuboid space in the detector. In a $2 \times 2 \times 1.5$ cm^3 CdZnTe detector, the material under an anode pixel is usually uniformly partitioned into 40 artificial voxels in depth [27]. The total number of partitions is limited by the spatial resolution of radiation interactions in pixelated CdZnTe detectors. In this thesis, an artificial voxel's size is $1720 \times 1720 \times 375$ µm^3, unless stated otherwise. The lengths of 1720 µm in the X- and Y-axis directions are equal to the pixel pitch (see Chapter I), and the length of 375 µm is equal to the thickness (15 mm) of the detector equally divided by 40. For simplicity, the depth of interaction will be expressed by number of voxels between the interaction and the collecting anode pixel hereafter. For example, an interaction happening on the cathode surface has a depth of 40. Example SRFs from

a pixel in the center of a detector are presented in Figure 2.16. It could be seen that for interactions with smaller depths, both the CAR and the timing difference between the anode and cathode waveforms decrease. Another interesting phenomenon is that anode SRFs for interactions further away from the collecting anode show slower turnings in the rising edges. This is caused by de-trapping of some trapped electrons as they drift towards the collecting anode. The trapping and de-trapping process effectively slows down these electrons and make the rising edge slower. This mechanism was investigated in detail in [18].

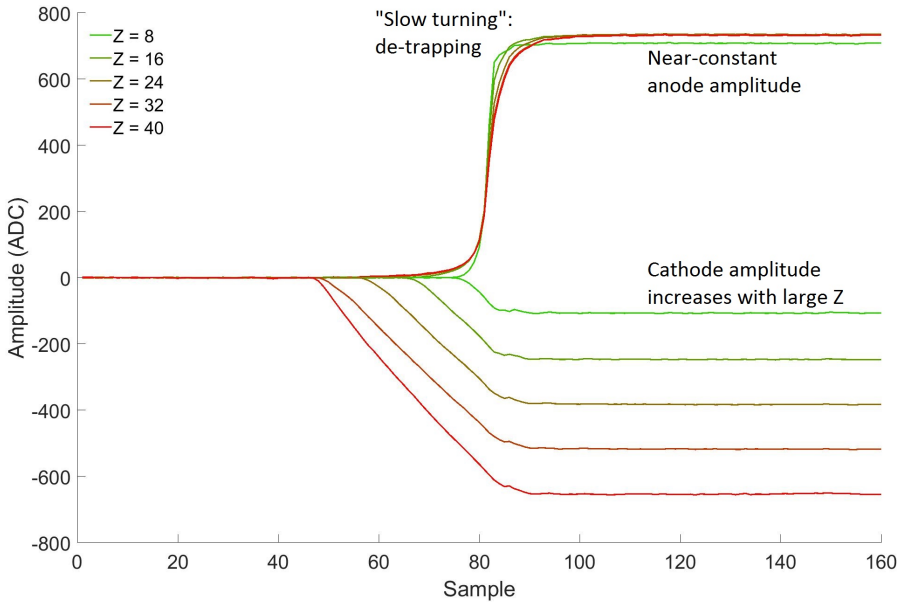

Figure 2.16: Anode and cathode SRFs with depth intervals of 8. The anode SRFs have positive amplitudes and cathode SRFs have negative amplitudes.

Assuming that electron cloud size does not affect the waveform shapes significantly, the measured single-pixel events SRFs can be used to predict noise-free waveforms from radiation interactions with arbitrary number of triggered anode pixels. The predicted waveforms can be expressed as

$$\overrightarrow{\tilde{wa}_i} = \overrightarrow{A_i(ch_i, E_i, \tau_i, z_i)}, i \in [1, k] \tag{2.3}$$

$$\tilde{\overrightarrow{wc}} = \sum_{i=1}^{k} \overrightarrow{C_i(ch_i, E_i, \tau_i, z_i)} \tag{2.4}$$

where k is the number of triggered anode pixels, $\tilde{\overrightarrow{wa_i}}$ is the predicted noise-free waveform from the i-th anode channel and $\tilde{\overrightarrow{wc}}$ is the predicted noise-free waveform from the cathode channel. $\overrightarrow{A_i}$ and $\overrightarrow{C_i}$ represent the adjusted single-pixel event SRFs from anode channel ch_i. Three types of parameters E_i, τ_i and z_i are adjusted in the fitting. E_i represents the energy deposition in the i-th channel and scales the amplitude of the SRFs. τ_i represents the time offset of the waveform. z_i represents the depth of energy deposition in the i-th channel. For example, $\overrightarrow{A(20, 661.7, 0, 35)}$ represents the measured anode SRF for a 661.7 keV interaction in channel 20, depth bin 35, with zero time offset. It should be noted the SRFs are measured discretely in time and space, while in the fitting, τ_i and z_i can appear in decimal numbers. To overcome this issue, linear interpolations are used when necessary.

For each event, the parameters E_i, τ_i and z_i are optimized to minimize the SSE between the measured waveforms and the predicted noise-free waveforms. For simplicity, the parameters can be expressed in vector forms $\vec{E}, \vec{\tau}$ and $\vec{z}$ and the optimization can be expressed by

$$\vec{E}^*, \vec{\tau}^*, \vec{z}^* = \underset{\vec{E},\vec{\tau},\vec{z}}{\arg\min} \sum_{i=1}^{k} \left\| \tilde{\overrightarrow{wa_i}} - \overrightarrow{wa_i} \right\|^2 + \left\| \tilde{\overrightarrow{wc}} - \overrightarrow{wc} \right\|^2. \tag{2.5}$$

In each iteration, the updated parameters are calculated by Levenberg-Marquardt algorithm [28]. The optimized estimations of $\vec{\tau}^*$ are used as the timing of the waveforms. In addition, the tail region sampling windows are also adjusted according to $\vec{\tau}^*$. With the time-aligned sampling windows, the errors in amplitude estimation are expected to be partially mitigated. Figure 2.17 presents an example of two-pixel event waveforms processed by SRF fitting. More detailed description of this algorithm and the implementation can be seen in [18].

SRF fitting is expected to provide the best energy resolution among the three

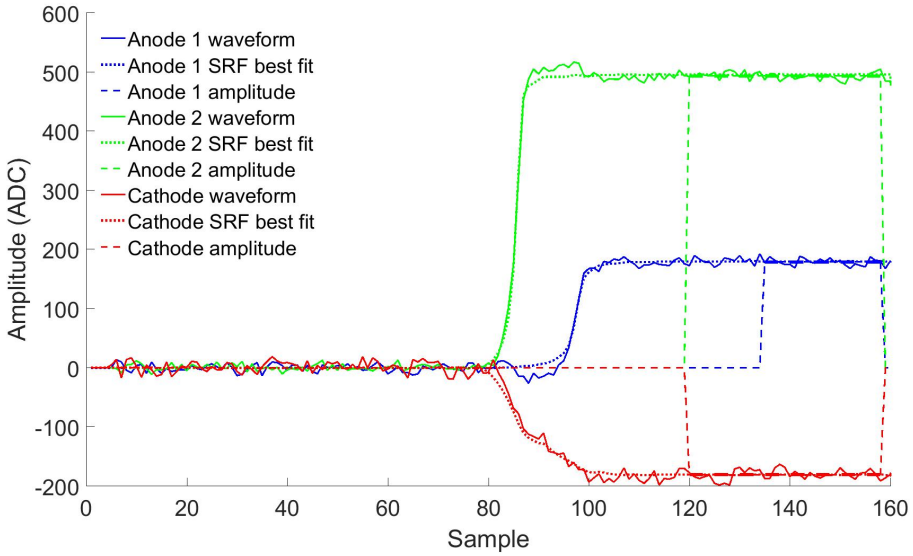

Figure 2.17: An example of SRF fitting and corresponding amplitudes estimation with time-aligned sampling windows.

waveform processing methods. However, a significant drawback of this method is that the optimization process requires numerous matrix operations and numerical interpolations, thus being costly in CPU time. Real-time waveform processing is very challenging to achieve using SRF fitting.

2.2.4 Sub-Pixel Position Sensing Technique

Sub-pixel position sensing technique estimates the position of energy deposition to a precision much smaller than the pixel pitch. This is achieved by comparing the transient signal amplitudes in the neighbor pixels. The nature of weighting potential cross-talk suggests that the neighbor pixels closer to the collecting pixel will have larger transient signal amplitudes. In 2011, Zhu developed a simple expression to estimate the lateral position of a single-pixel interaction to a sub-pixel precision [18]:

$$\tilde{X} = \frac{A_1 + A_4 + A_6 - A_3 - A_5 - A_8}{A_1 + A_4 + A_6 + A_3 + A_5 + A_8} \tag{2.6}$$

$$\tilde{Y} = \frac{A_1 + A_2 + A_3 - A_6 - A_7 - A_8}{A_1 + A_2 + A_3 + A_6 + A_7 + A_8} \tag{2.7}$$

In the equations above, A_i represents the transient signal amplitude in neighbor pixel i. The relative locations of the neighbor pixels are presented in Figure 2.18. Figure 2.18 also presents an example 661.7 keV, single-pixel event's waveforms and the estimated location of interaction in the collecting pixel. In practice, the transient signal amplitudes are estimated by feeding the signals through a digital filter with fast shaping time. By default, a CR-RC filter with a shaping time constant 100 ns is used for these neighbor pixel waveforms. For 661.7 keV, single-pixel events, the position resolution can achieve about 300 µm [29]. The improvement in position resolution brought about substantial improvement in imaging quality of pixelated CdZnTe detectors [15].

2.3 Events Reconstruction

Reconstruction of radiation interactions, also known as events, include both position and energy reconstruction. The development of events reconstruction algorithm started over 20 years ago when He found out that the depth of a single-pixel event can be estimated by cathode-to-anode signal amplitude ratio in pixelated CdZnTe detectors [30]. Over the past years, numerous improvements were made to the algorithm [27, 31, 32]. This section briefly introduces the position and energy reconstruction for single-pixel and multi-pixel events separately. A more detailed introduction can be seen in [27].

2.3.1 Single-Pixel Events Reconstruction

The principle of events reconstruction is constructing a data base through calibration, then looking up parameters in the data base using information for each event for position and energy estimation. In a pixelated CdZnTe detector, a calibration usually uses a measurement of a ^{137}Cs source to construct the data base. This is because the ^{137}Cs source emits a gamma ray with 661.7 keV energy. This energy is neither

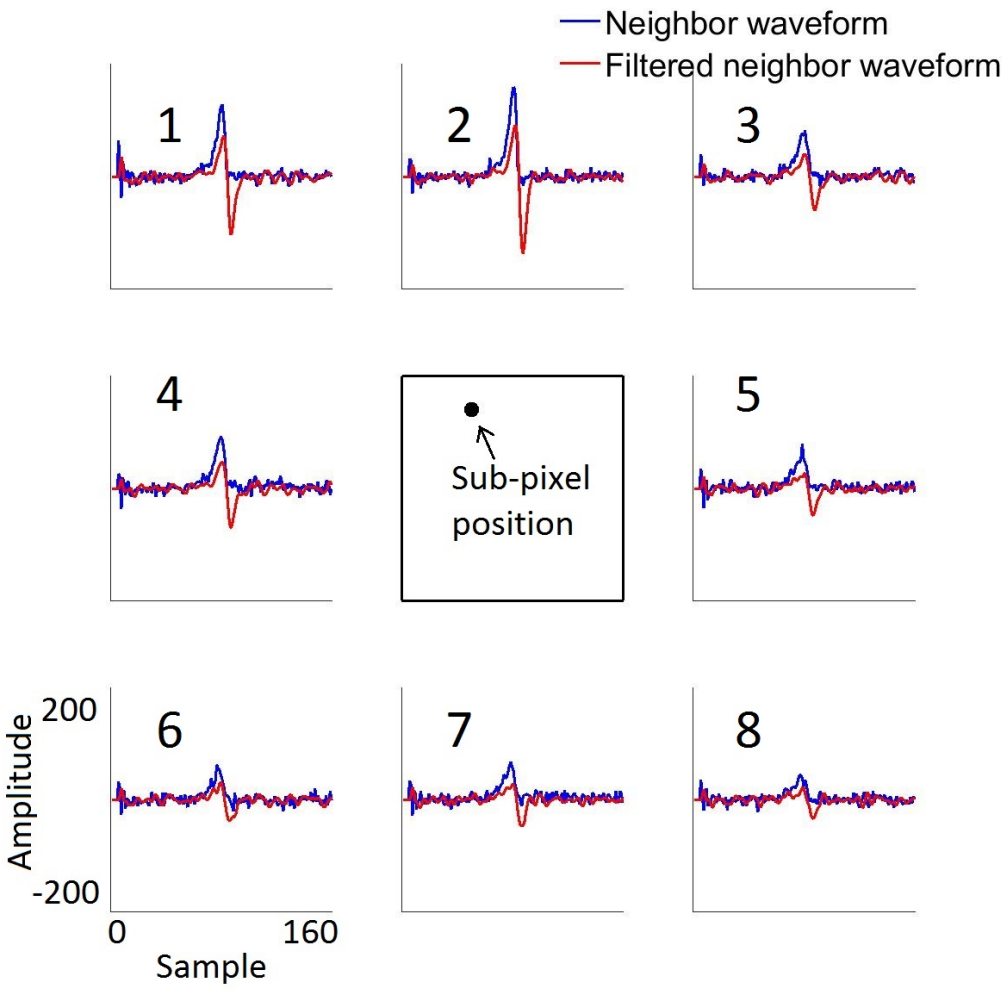

Figure 2.18: An example single-pixel event processed with sub-pixel sensing.

too low to be attenuated and just interact on the surface of the detector, nor too high to require long measurement time because gamma ray photoelectric interaction cross-sections decrease at higher energies. Additional measurements might be needed for non-linearity correction and will also be discussed.

As discussed in 2.1, 121 anode channels and a cathode channel are used to read out wavefroms from the electrodes in a pixelated CdZnTe detector. The electronic components in the channels are not expected to be exactly the same. As a result, the gain in each channel must be corrected. In each anode channel, the gain can be estimated by measuring the cutoff on the right side of the 661.7 keV peak in a ^{137}Cs measurement. Based on Shockley-Ramoe theorem, cathode channel signal amplitudes will not form a peak in the spectrum. Instead, mono-energetic gamma-ray interactions that are uniformly distributed in a detector will result into a continuum in the cathode channel spectrum. Still, the cutoff on the high-energy side of the continuum can be used to represent the cathode channel gain, because only cathode-side, full-energy depositions can induce these amount signal amplitudes. Figure 2.19 shows examples of anode and cathode channel spectra and corresponding cutoffs. For simplicity, AC_i and CC are used to represent the high-energy cutoff for the i-th anode and the cathode channel in a pixelated CdZnTe detector hereafter.

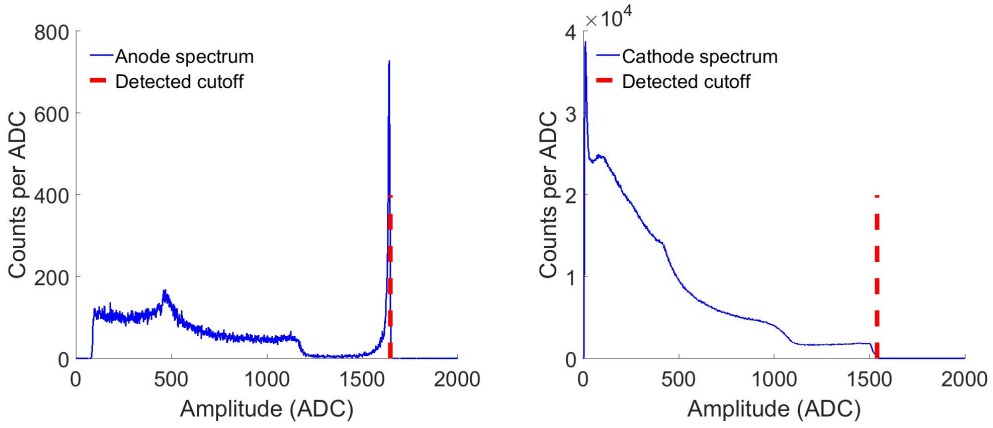

Figure 2.19: (Left) an example anode channel spectrum and cutoff. (Right) cathode channel spectrum and cutoff.

As discussed in Chapter I, the cathode-to-anode signal amplitude ratio (CAR) is linearly related to the depth of interaction in single-pixel events. This relationship was also experimentally verified by Kaye [31]. Hence, the depth of a single-pixel event that triggers the i-th anode channel can be expressed as

$$\tilde{Z} = 40\frac{AC_i \cdot S_C}{CC \cdot S_{A,i}} \tag{2.8}$$

where S_C and $S_{A,i}$ represent the amplitudes of cathode and anode signals respectively. The ratio is normalized by the cutoffs to cancel out the effect of channel-by-channel gains, and multiplied by 40 because the space under each anode channel is artificially divided into 40 voxels. The anode signal amplitudes are recorded separately for each voxel and the centroid of the peak corresponding to the 661.7 keV photoelectric interaction can be measured. Figure 2.20 presents an example signal amplitude spectrum for one voxel in a calibration.

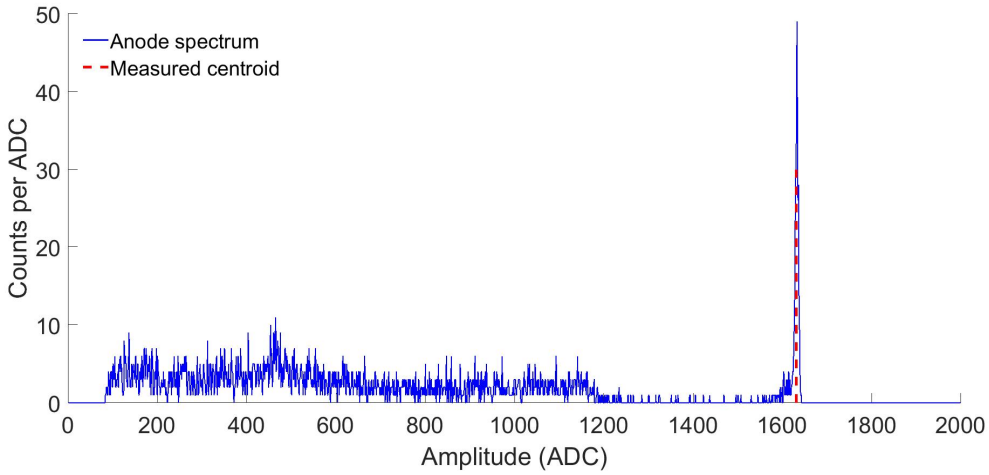

Figure 2.20: An example voxel's spectrum and measured 661.7 keV peak centroid.

Assuming the measured photopeak centroid in the i-th channel at depth z is $g(i, z)$, a single-pixel event's energy can then be calculated by Equation 2.9. Note some of the symbols are already used and defined in Equation 2.8.

$$\tilde{E} = 661.7 \frac{S_{A,i}}{g(i, \tilde{Z})} \tag{2.9}$$

To ensure accuracy of measured photopeak centroid, sufficient amount of events under the full-energy peak is needed. In a simplified model, one could assume that the measured signal amplitude for each event is the summation of the true amplitude and a Gaussian noise that is independent of any other event (i.e. sample). Assuming an intermediate pixelated CdZnTe detector has 0.5% FWHM resolution for 661.7 keV single-pixel events, and the measurement of the photopeak centroid is simply taking the average of all the samples' amplitudes under the photopeak. If 200 events are accumulated under a photopeak, then the relative uncertainty of the photopeak centroid should be $0.5\%/\sqrt{200} = 0.035\%$ (equivalent FWHM). Based on Equation 2.9, about 0.2 keV error is expected in energy reconstruction of subsequent events. This error is negligible compared to the electronic noise in the system. In practice, a million 661.7 keV, full energy, single-pixel events are needed for the calibration of one pixelated CdZnTe detector as this ensures about 200 photopeak counts under the peak of spectrum in each voxel. This is the bottleneck limiting the efficiency of calibration in a detector.

Figure 2.21 presents an example of measured photopeak centroid in each depth under an anode channel, compared against the depth of interaction. This relationship is also referred to as "gain-depth curve". Two major mechanisms affect the shape of this curve. For events with small depth values (i.e. being close to the anode side), the photopeak centroid decreases rapidly at lower depths. This is because the weighting potential for the collecting anode pixel changes very rapidly near the anode side, similar to that in Figure 1.3. For events close to the cathode side, however, the photopeak centroid decreases at higher depths. This happens because the collecting pixel's weighting potential changes insignificantly for non-near-anode regions. On the other hand, electron clouds from interactions near the cathode side drift through

longer paths to the collecting anode. These electron clouds are subject to more trapping and induce less charge on the collecting anodes. The effect of electron trapping is discussed in detail in Chapter III.

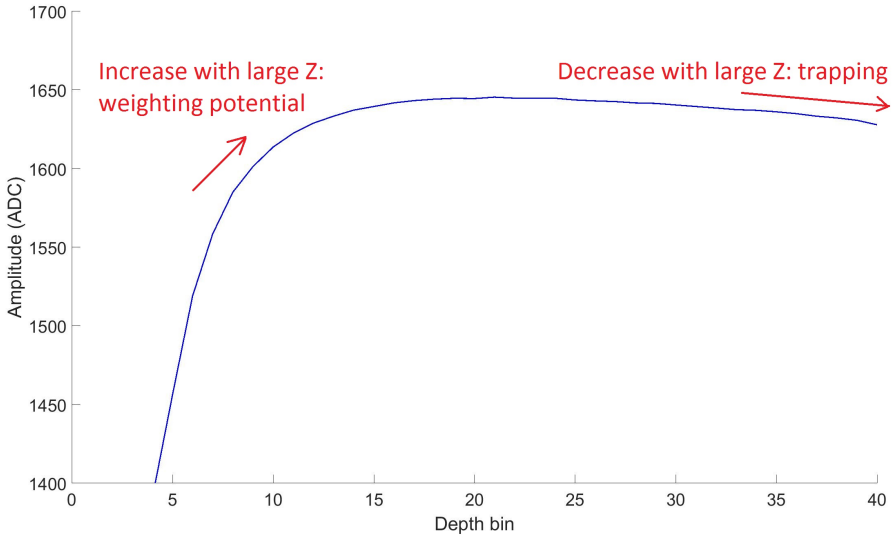

Figure 2.21: An example gain-depth curve. The effects of weighting potential change and electron trapping are also highlighted.

Non-linearity in pixelated CdZnTe detector is a non-negligible issue and must be corrected. Figure 2.22 presents the measured differential non-linearity in some channels of a detector. The dynamic range in this measurement was set to 3 MeV.

Differential non-linearity is defined as the difference between reconstructed energy and the true energy. For a perfectly linear detector system, the value is expected to be zero for all energies. As Figure 2.22 presents, in digital 3-D CdZnTe, gamma-ray interactions over 1 MeV can be significantly over-estimated in energy. In addition, the non-linearity is not exactly the same in each anode channel. For example, the reconstructed energies for 2614 keV events can differ by up to 5 keV among the anode channels. This value is larger than electronic noise in the system and can degrade the single-pixel events energy resolution significantly. For simplicity, the issue of difference in each channel's non-linearity is referred to as "non-uniformity of non-linearity" hereafter. In pixelated CdZnTe detectors, polynomial regressions are used

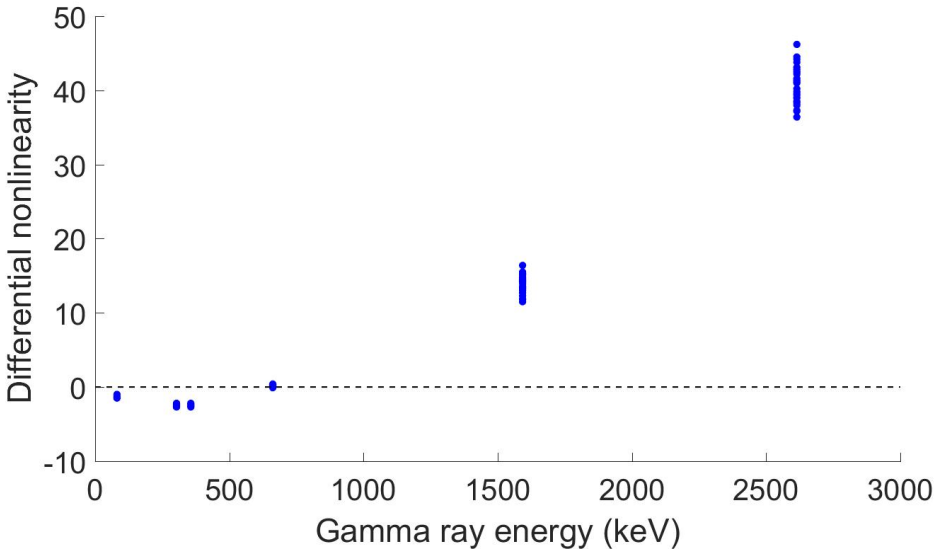

Figure 2.22: Measured differential non-linearity in a detector using the VAD_UM v2.2 system. 3 MeV dynamic range was used.

to explain the relationship between the true energy and the reconstrcuted energy for different gamma rays. The regressions are then used to correct for non-linearity in any subsequent measurements [31].

2.3.2 Multi-Pixel Events Reconstruction

For multi-pixel events, CAR can no longer be used to estimate depth of interactions. Instead, the timing difference between each anode signal and the cathode signal could be used. In CdZnTe detectors, the electric field and mobility-lifetime product can vary detector-by-detector. As a result, the relationship between anode-to-cathode timing difference and the depth of interaction in each channel has to be mapped. In practice, the relationship between the cathode-to-anode timing difference and the CAR is mapped for 661.7 keV, single-pixel events in each channel. An example is presented in Figure 2.23. This curve is referred to as "timing-depth curve" hereafter. It should be noted the timing-depth curve shown in Figure 2.23 has a convex shape, indicating that the electron clouds further away from the anode have lower average drift velocities. Assuming that mobility throughout depth 0 to 40 is uniform, the

figure further indicates that the electric field in the detector is non-uniform. The issue of electric field non-uniformity in large volume, room temperature semiconductor detectors has been a challenge and is under active investigations [33, 34].

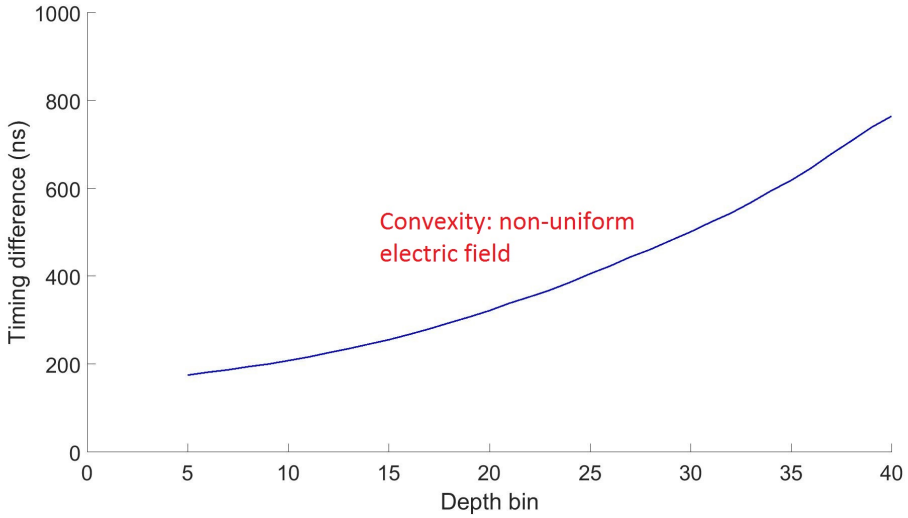

Figure 2.23: An example timing-depth curve. The convexity of the curve indicates non-uniform electric field in the detector. The non-zero intercept is an artifact due to the differences in cathode and anode waveform shapes and filters and does not affect the reconstruction.

As Figure 1.4 indicates, when an electron cloud drifts perpendicularly towards the collecting anode, signals are also induced on other anodes in a pixelated CdZnTe detector. This signal gradually increases until the cloud is very close to the anode region, then decreases rapidly as the electron cloud gets collected by the corresponding anode. The net signal amplitude is almost always negative, expected when the electron cloud is generated very close to the cathode and the net signal amplitude is zero. This phenomenon is called "weighting potential cross-talk" (or WPCT for simplicity). In a multi-pixel event, WPCT can cause the signal amplitude measured in each anode channel to be smaller than the signal without WPCT.

In the calibration of pixelated CdZnTe detectors, WPCT is calibrated using 661.7 keV, two-pixel events. These events are recorded separately for each pair of lateral

distance between the two triggered anode pixels, and the "centroid depth" of interaction. The centroid depth of interaction ($\bar{Z}$) is calculated by

$$\bar{Z} = \frac{\tilde{E}_1\tilde{Z}_1 + \tilde{E}_2\tilde{Z}_2}{\tilde{E}_1 + \tilde{E}_2} \tag{2.10}$$

where $\tilde{Z}_1, \tilde{Z}_2, \tilde{E}_1$ and $\tilde{E}_2$ represent the reconstructed depths and energies in anode 1 and 2, respectively. Assuming that the lateral distance between the two pixels is d, a 2-D matrix W can be constructed with each element $W(d, \bar{Z})$ representing the measured 661.7 keV, two-pixel event peak centroid. In practice, three matrices are constructed for different types of triggered pixels in a two-pixel event: both belong to the center 9×9 pixel region (W_{CC}), both belong to the peripheral region (W_{EE}), and one from each region (W_{CE}). This helps improve the reconstructed energy resolution because weighting potential profile for peripheral pixels is very different compared to the center 9×9 pixels. In fact, a perfect WPCT calibration should be carried out for every unique pair of voxels in each CdZnTe detector. However, this detailed calibration would require an extremely large amount of calibration data and make the calibration impractical. The paritioning of pixels into only center 9×9 region and peripheral region is a compromise for efficiency of calibrations. Figure 2.24 presents example photopeak centroids compared against the centroid depth for two-pixel events that have two SN anode pixels triggered. The data is shown separately for different types of pixels. It could be seen that when both pixels belong to the peripheral region, the WPCT causes the most energy deviation from 661.7 keV. Another observation worth mentioning is that WPCT causes more energy deficit for events near the anode side.

Based on superposition principle, WPCT in each anode pixel of a multi-pixel event can be corrected by

$$\tilde{E}_i{}' = \tilde{E}_i + \sum_{j \neq i}^{k} \tilde{E}_j \left(\frac{661.7}{W_{typej}(d_{i,j}, \tilde{Z}_j)} - 1\right) \tag{2.11}$$

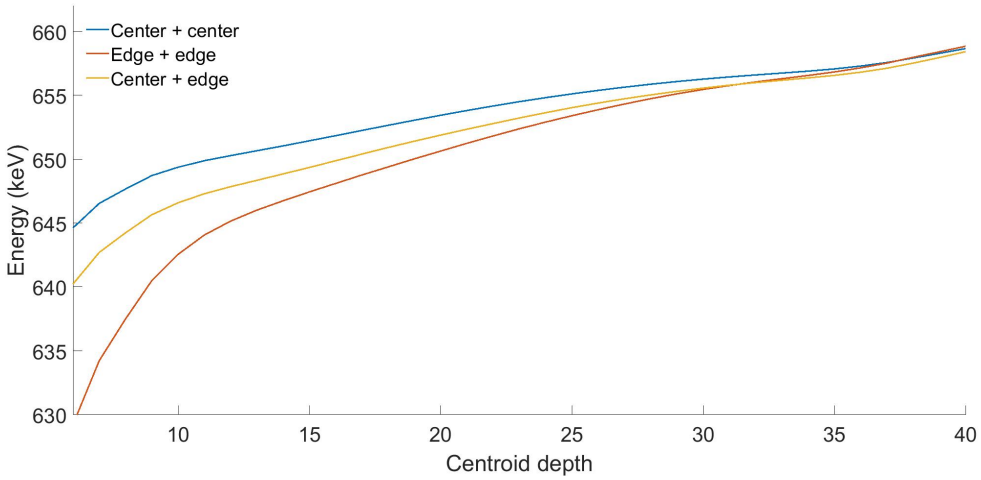

Figure 2.24: Example of 661.7 keV, two-pixel SN events peak centroids in a detector for different combinations of pixel locations.

where k is the total number of triggered anode channels and W_{typej} represents the type of the pixel pair (i, j) (center + center, edge + edge or edge + center). In the i-th anode, the energy is corrected once for every other triggered anode channel because WPCT happends for every pair of triggered anodes.

2.4 Summary

This chapter gives a brief introduction of the techniques that enabled the work in this thesis. The digital readout systems read out waveforms from the pre-amplifiers with very low noise. Various waveform processing methods provide flexible options to investigate information about the interactions in CdZnTe. The 3-D events reconstruction algorithms lay the foundation of position and energy reconstruction of radiation interactions.

Figure 2.25 presents a simplified summary of single-pixel and multi-pixel events calibration in 3-D CdZnTe detectors using only a ^{137}Cs source measurement. With the correct calibration, 3-D CdZnTe could reach very outstanding energy resolution. Figure 2.26 presents the spectra measured in an example direct-attachment module.

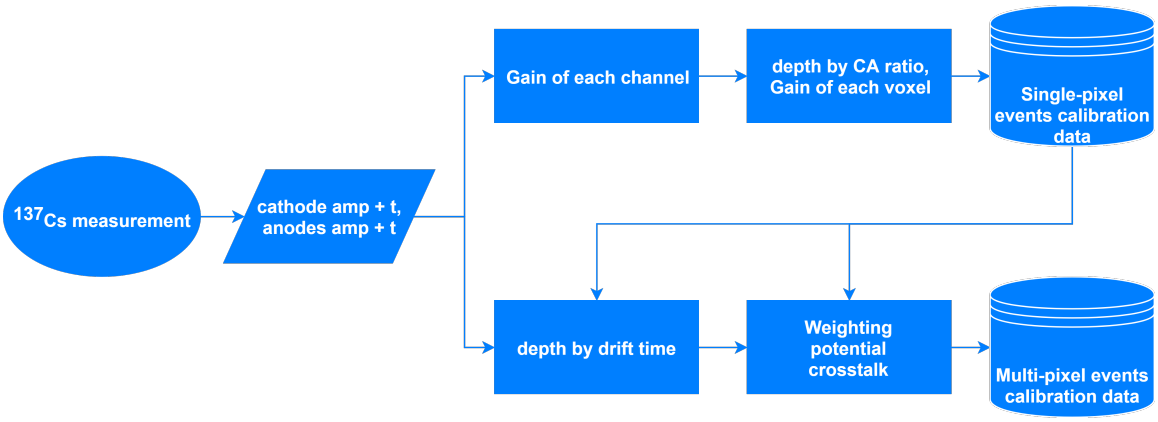

Figure 2.25: Simplified calibration flowchart for a 3-D CdZnTe detector.

Such performance was observed on many recently delivered direct-attachment 3-D CdZnTe detectors. The outstanding resolution achieved at room temperature makes these detectors very attractive in application.

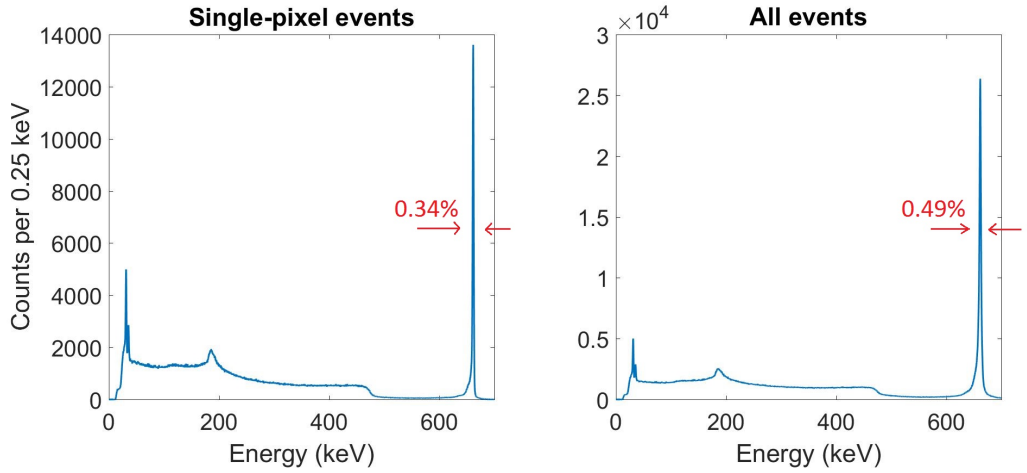

Figure 2.26: Spectra of a ^{137}Cs measurement from an example detector, directly attached to a VAD_UM v2.2 ASIC carrier board.

CHAPTER III

Electron Mobility-Lifetime Product Measurement in 3-D CdZnTe with the Digital System

3.1 Electron mobility-lifetime product and trapping

The electron mobility-lifetime product ($\mu_e\tau_e$) in CdZnTe detectors is a very important characteristic that implies the quality of the detector. Previous work shows that 3D position-sensitive CdZnTe detectors with higher $\mu_e\tau_e$ values usually had better energy resolution after depth-dependent correction [35]. High-accuracy $\mu_e\tau_e$ measurements can help estimate CdZnTe material quality, providing valuable information for improving crystal production.

The value of $\mu_e\tau_e$ determines the amount of trapped electrons in CdZnTe detectors as they drift towards the collecting anode. This process can be modeled as

$$N = N_0 \exp(-\frac{D}{\mu_e\tau_e E}) \tag{3.1}$$

where N_0 and N represent the number of electrons in the beginning and during the drift, D presents the drift distance, E represents the electric field. This equation assumes that both the electric field and $\mu_e\tau_e$ in the detector are constant values.

In recent years, the $\mu_e\tau_e$ values in CdZnTe detectors increased significantly. As will be shown in Figure 3.7, the latest Redlen detectors showed $\mu_e\tau_e$ values as high as

5×10^{-2} cm^2/V. With this $\mu_e\tau_e$ value, if a $2 \times 2 \times 1.5 cm^3$ detector is biased at - 3000V, at most 1.5% electrons will get lost due to trapping when the interaction occurs on the cathode side of the detector. This small amount of trapping raises more challenges in accurate measurement of CdZnTe detector $\mu_e\tau_e$ values. In the work described in this chapter, simple subtraction was used to give unbiased estimations of the signal amplitudes. This could mitigate the effect of ballistic deficit [36] in the measurement of the $\mu_e\tau_e$ values in 3-D CdZnTe detectors.

A part of results described in this chapter have been published as [37].

3.1.1 Two-Bias Method

Two $\mu_e\tau_e$ measurement methods are commonly used in 3-D CdZnTe detectors: two-bias method and depth-fitting method. The work described in this chapter attempts to improve the measurement results on both methods.

The two-bias method was developed by He in 1998 [38]. This method compares cathode-side photopeak events signal amplitudes measured at various cathode biases. Assuming two ^{137}Cs measurements are carried out with V_1 and V_2 voltage differences on the detector, and the measured 661.7 keV peak centroids are A_1 and A_2, the two-bias method can calculate the $\mu_e\tau_e$ value by

$$\mu_e\tau_e = \frac{D^2}{\ln \frac{A_1}{A_2}} \Big(\frac{1}{V_2} - \frac{1}{V_1} \Big). \tag{3.2}$$

In Equation 3.2, the peak centroid A is regarded as a direct representation of the amount of collected electrons N in Equation 3.1.

3.1.2 Depth-Fitting Method

Boucher developed a new method to measure the $\mu_e\tau_e$ values in 3-D CdZnTe in 2012 [39]. This method only requires one measurement, and compares the measured

signal amplitude against different depth of interactions. The calculation is summarized by

$$\mu_e\tau_e = \frac{t_2 - t_1}{V \times \ln \frac{A_1}{A_2}} \int_{z=z_1}^{z=z_2} v(z)dz \tag{3.3}$$

where t_1 and t_2 represent the measured drift times of electron clouds from z_1 and z_2 to the anodes while $v(z)$ represents the velocity of electron cloud as a function of z. $v(z)$ can be calculated using the measured drift time at different depth bins. This method can be used in conjunction with the conventional calibration process in 3-D CdZnTe detectors. However, unlike the two-bias method that only uses cathode-side events, this method uses events from both the cathode surface and the bulk. As a result, the effect of weighting potential change on the signal amplitude must be corrected. The weighting potential field calculation can be done by using ANSYS Maxwell. In practice, $\mu_e\tau_e$ values for the center 7×7 pixels in each detector are calculated because the weighting potential profile is significantly different for the peripheral pixels.

3.2 Effect of Ballistic Deficit on $\mu_e\tau_e$ measurement

As mentioned in Chapter II, trapezoidal filters were found to have the best performance for 3-D CdZnTe detectors. Conventionally, they are used to process waveforms from calibration measurements on each 3-D CdZnTe detector that arrive at the University of Michigan. However, it was found that ballistic deficit exists when trapezoidal filters were used to process the waveforms. An example in Figure 3.1 shows the amplitude of a SRF from the cathode-side of a pixel in detector 5R-68 (biased to -2500 V) was estimated to be 1582 ADC using a trapezoidal filter. In comparison, directly subtracting the average baseline value from the average tail value (simple-subtraction method hereafter) estimates the amplitude to be 1599 AC. As the bias or the interaction location changes, the ballistic deficit (by percentage) changes as well, because

of the change in the waveform shape. For the same pixel shown in Figure 3.1, with the detector biased to -2000 V, the amplitudes estimated by trapezoidal filter and simple-subtraction are 1551 ADC and 1578 ADC, respectively. Figure 3.2 presents the relative amplitude deficit in all the anode channels of 5R-68 at different biases. The relative deficit is calculated by $(A_{subtr} - A_{filter})/A_{filter}$. A_{subtr} and A_{filter} represent the amplitudes calculated by simple-subtraction and trapezoidal filter, respectively.

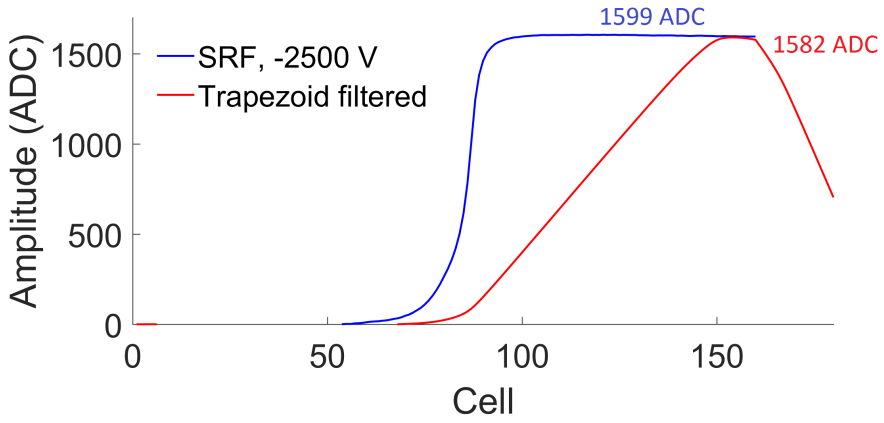

Figure 3.1: An example showing the ballistic deficit for a SRF waveform from the cathode side of 5R-68.

Although Figure 3.2 shows that ballistic deficit by percentage is only less than 1%, the effect on $\mu_e\tau_e$ value calculation in 3-D CdZnTe is substantial. Using the amplitudes from trapezoidal filter and simple-subtraction in Figure 3.1, the term $1/(\ln(N_1/N_2))$ in Equation 3.2 is 58 and 94 respectively (presented in Figure 3.3). For the pixel in this discussion, the $\mu_e\tau_e$ measurement with two-bias method using trapezoidal was about 40% lower than the result using the simple-subtraction method.

3.3 $\mu_e\tau_e$ Measurement with Simple Subtraction

Fortunately, with digital readout systems, the waveform amplitudes can be estimated using simple subtraction. Figure 3.4 presents the measured $\mu_e\tau_e$ values in 5R-48 by depth-fitting and two-bias methods. The signal amplitudes were extracted

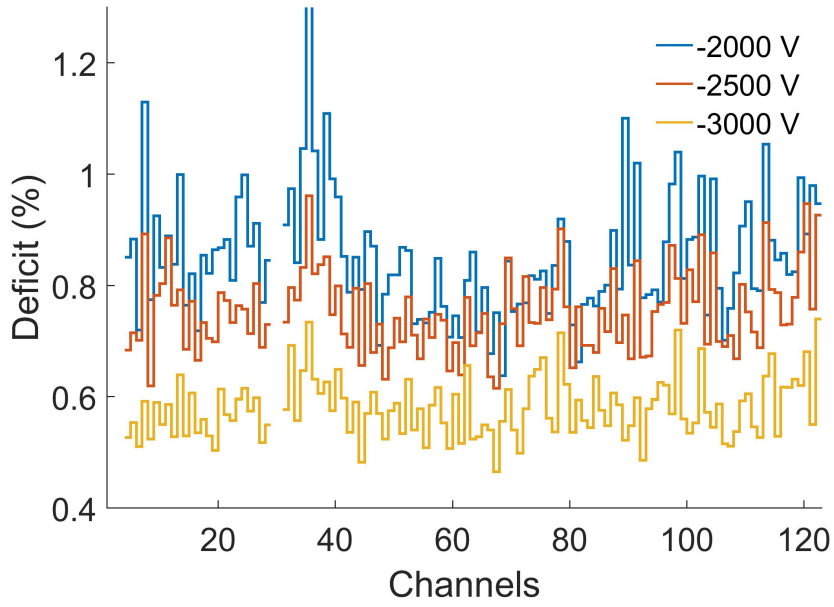

Figure 3.2: Deficit by percentage in all channels of 5R-68 for different biases.

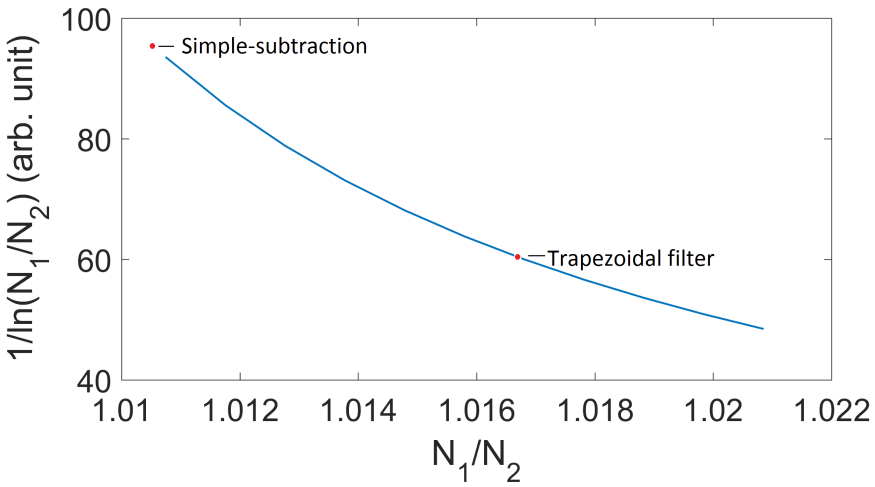

Figure 3.3: The term $1/(\ln(N_1/N_2))$ changes very rapidly with N_1/N_2 when N_1/N_2 is close to 1.

using both trapezoidal filter and simple subtraction. It could be seen that simple subtraction resulted into much higher measured $\mu_e\tau_e$ values.

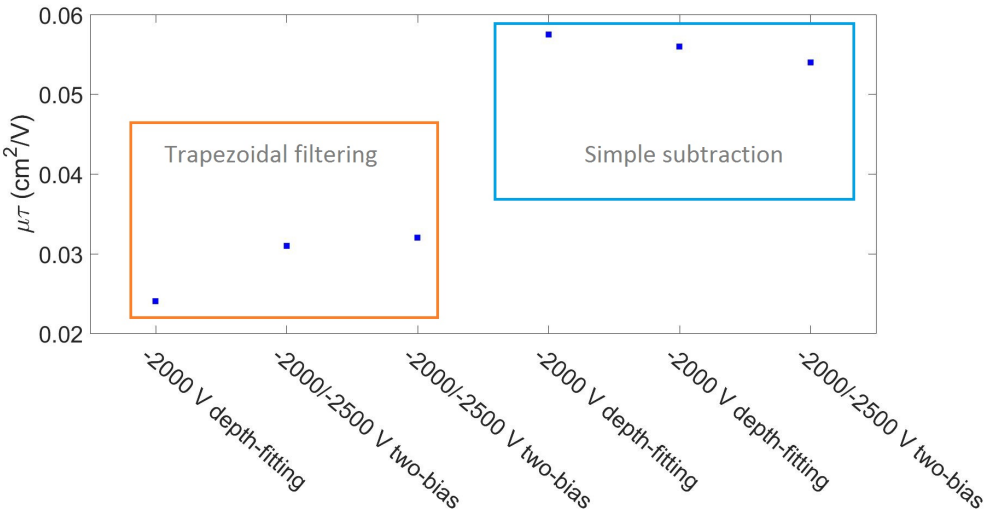

Figure 3.4: Measured $\mu_e\tau_e$ values through simple subtraction are much higher than those from trapezoidal filtering. Examples drawn from measurements on detector 5R-48.

Figure 3.5 and Figure 3.6 present the measured $\mu_e\tau_e$ from repeated measurements with detectors 5R-40 and 5R-68. About 20% relative variation was observed in both detectors using either two-bias method or depth-fitting method. The uncertainty was estimated by calculating the maximum deviation of each result from the averaged result. This measured uncertainty was much larger than previous estimations in [39] and [38].

A possible reason is that the CdZnTe detectors tested in this experiment have better qualities (larger $\mu_e\tau_e$ values) than the detectors studied in [39] and [38]. The larger $\mu_e\tau_e$ values, the less amplitude change is expected due to electron trapping. For example, assume the two-bias method is used to calculate the $\mu_e\tau_e$ values in a 3-D CdZnTe detector. Also assuming the calculation is based on cathode side photopeak events at biases of -3000V and -2500V. For a detector with a $\mu_e\tau_e$ value of 0.05 cm^2/V, the expected relative amplitude decrease at -3000 V bias is about 0.3%. In comparison, if the true $\mu_e\tau_e$ value is 0.03 cm^2/V, the expected relative decrease is

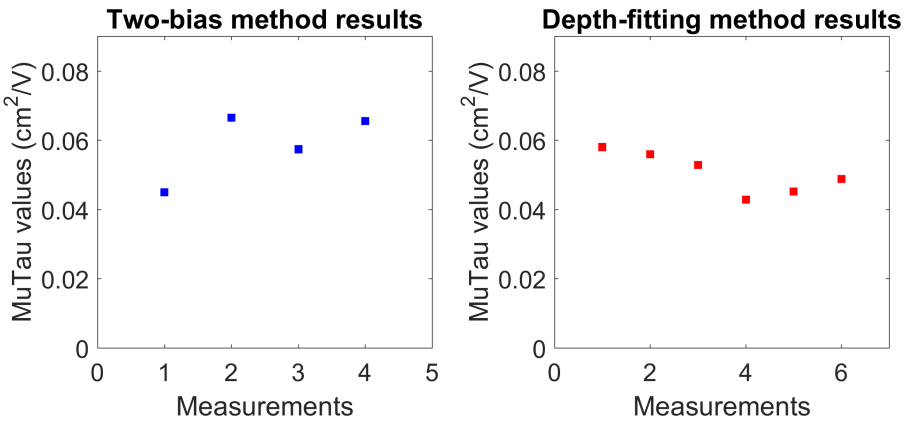

Figure 3.5: Repeated $\mu_e\tau_e$ measurements in 5R-40.

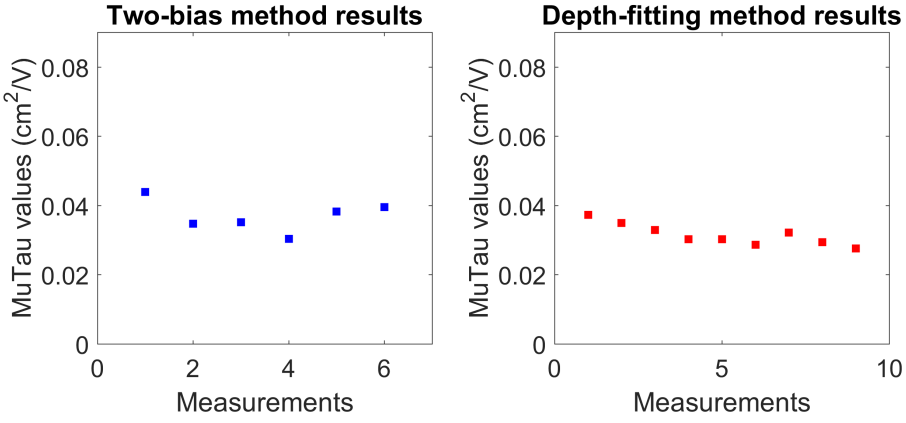

Figure 3.6: Repeated $\mu_e\tau_e$ measurements in 5R-68.

about 0.5%. Formula (3.4) describes the calculation of expected relative amplitude difference for two different biases. The notations are the same as that in (3.2).

$$\exp(-\frac{D^2}{V_1\mu_e\tau_e}) - \exp(-\frac{D^2}{V_2\mu_e\tau_e}) \tag{3.4}$$

The principle of $\mu_e\tau_e$ calculation is measuring the relative change of signal amplitude due to trapping. The above discussion showed that this relative amplitude change is expected to decrease for larger $\mu_e\tau_e$ values. On the other hand, the potential contributors to $\mu_e\tau_e$ uncertainty, such as statistical fluctuation and non-uniform electric field [33], are not affected. Hence, the relative $\mu_e\tau_e$ uncertainty is expected to increase for detectors with larger $\mu_e\tau_e$ values.

With simple subtraction to estimate the amplitudes, the calculated $\mu_e\tau_e$ values of seven CdZnTe detectors are presented in Figure 3.7. Based on the results in Figure 3.5 and Figure 3.6, a universal relative uncertainty of 20% was added for each measurement. The values were consistent, within estimated uncertainty, across differing calculation methods and biases. Notably, the values with trapezoid filters were also significantly lower than the values from simple-subtraction methods. Detectors with larger serial numbers were delivered more recently and they showed increased $\mu_e\tau_e$ values. Detector 5R-40 was received in October 2014, while 5R-69 was received in December 2016. The measured $\mu_e\tau_e$ values increased significantly in the seven detectors that were delivered over the range of two years. The limited samples indicate a high probability that the detector quality has been improving over time.

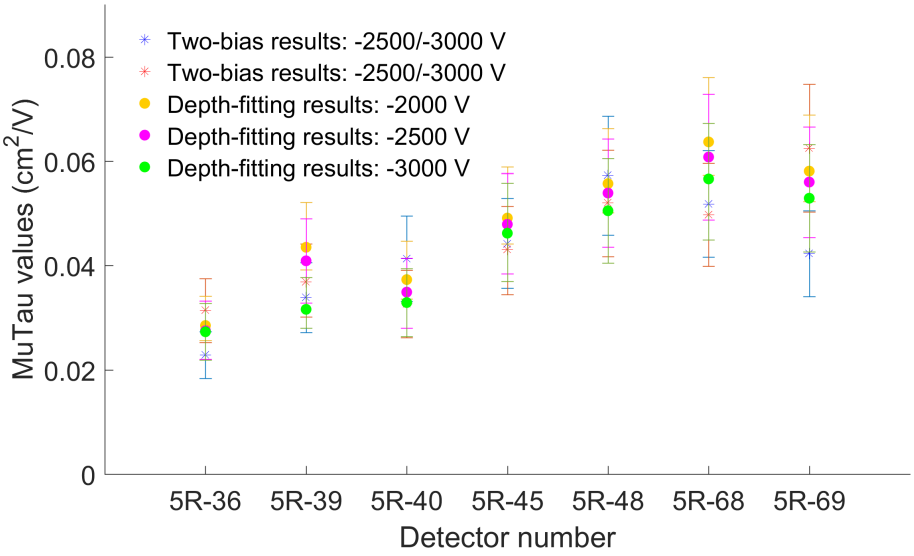

Figure 3.7: The $\mu_e\tau_e$ values calculated using both the depth-fitting and two-bias methods for seven detectors at different cathode biases. Simple-subtraction was used to estimate the amplitudes.

CHAPTER IV

Temperature Based Gamma-ray Event Reconstruction

4.1 3-D CdZnTe at Varying Ambient Temperatures

While CdZnTe detectors can be operated at room temperature, in operation it was found that the ambient temperature still needs to be regulated. Up to now, most of the 3-D CdZnTe detector systems required at least a fan and a Peltier to constantly extract heat generated from the ASICs. For example, an Orion system can consume up to 15 W power, with about 7 W used in temperature regulation. This extra power consumption significantly hinders the design of hand-held, 3-D CdZnTe detector systems. With the same battery, the operation time of the Orion system can be shortened by up to 40 %. In addition, extra weight and room are needed for the cooling components. If the temperature regulation can be omitted without significantly degrading the performance of the 3-D CdZnTe detectors, the future generations of hand-held 3-D CdZnTe detector systems can become much more convenient to use.

Previously, Mann studied the effects of ambient temperature on 3-D CdZnTe detectors read out by IDEAS analog systems [40]. The study was obfuscated by the complex response in the analog components. For example, the IDEAS analog systems

used peak-hold circuits to "hold" the signal amplitude in each channel before being read out and the response of peak-hold circuits changes with temperature. Mann used singular value decomposition (SVD) [41] to reduce the amount of data required for calibration, but SVD comes at the cost of reduced interpretability of each correction step. In addition, the poor performance in the analog systems hindered detailed analyses. In this chapter, the effect of ambient temperature change on 3-D CdZnTe detectors, read out by digital systems, are discussed in detail. The mechanisms that cause systematic changes in the detector system response are separated. Different methods were developed to compensate for the systematic changes. Using a temperature sensor on the ASIC, real-time, temperature-based event reconstructions were carried out.

A part of results described in this chapter have been published as [42].

In this study, an environmental chamber [43] was used to control the ambient temperature of the system. Limited by space, a VAD_UM v2.2 single-board system was used. The system uses a single VAD_UM v2.2 ASIC populated in a separable frontend box. Thanks to the design, the frontend box could be placed inside the environmental chamber while subsequent readout electronics are kept outside. It should be noted the ambient temperature in the environmental chamber is slightly different from the ambient temperature in a realistic environmental. In the environmental chamber, a constant air flow at the set temperature keeps blowing. In contrast, the air is expected to stay still in an open area most of the time. In this chapter, "ambient temperature", or "temperature" for short, represent the temperature setting of the environmental chamber exclusively. Figure 4.1 presents an image of the environmental chamber and the frontend box.

To clearly show the challenge when 3-D CdZnTe is used without temperature regulation, detector 5R-76 was calibrated at various ambient temperatures. Using the calibration data acquired at 0 ^{o}C, measured data at various ambient temperatures was

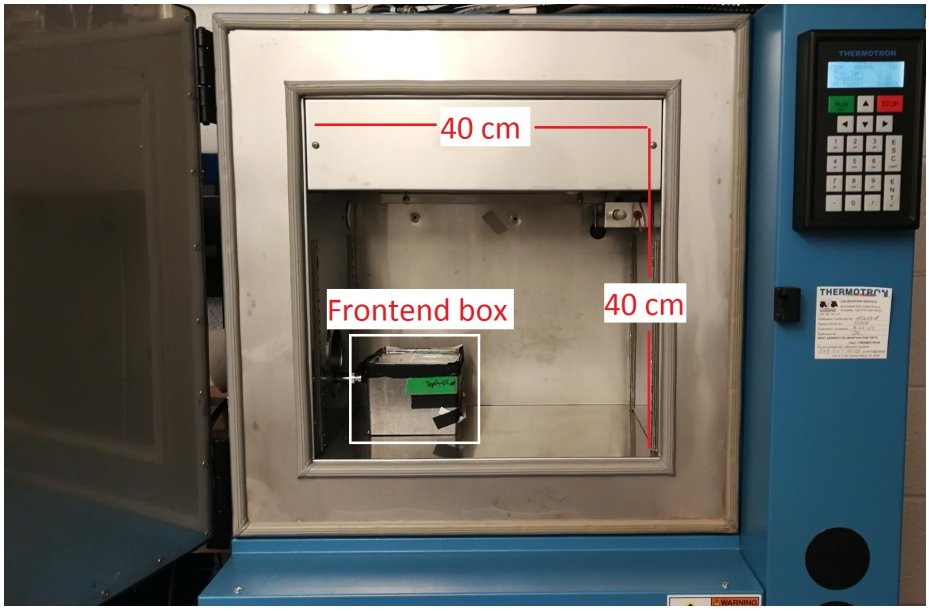

Figure 4.1: Figure of the environmental chamber and the frontend box.

reconstructed. Figure 4.2 presents the energy spectra for these measurements. For easier comparison, Figure 4.2 also presents the single-pixel events resolution FWHM for these measurements using either the 0 ^{o}C calibration or self-calibration. Self-calibration means that the calibration generated from a ^{137}Cs measurement is applied to the measurement itself. This provides a "benchmark" of the expected resolution FWHM. It could be seen that in self-calibrated results, the single-pixel events resolution was always about 0.5% FWHM. In contrast, when the 0 ^{o}C calibration was applied, the resolution kept degrading for measurements taken at higher ambient temperatures. Furthermore, for these measurements taken at higher temperatures, the reconstruction using the 0 ^{o}C calibration significantly underestimated the energies. For example, the measurement at 30 ^{o}C showed a spectrum with the 661.7 keV peak centered at about 642 keV.

To maintain good performance without temperature regulation, two critical challenges must be addressed. First, algorithms are needed to quickly calibrate a detector at various temperatures. Second, if several calibrations were carried out at different

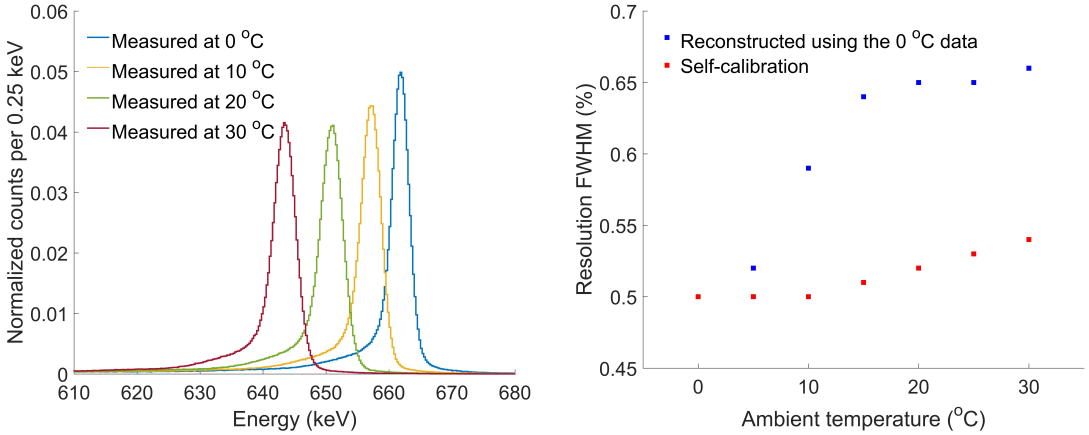

(a) Energy spectra in the peak region

(b) Energy resolution at 661.7 keV

Figure 4.2: ^{137}Cs measurements were conducted at different ambient temperatures and reconstructed using a 0^{o}C calibration. Reconstructed peak centroids decrease with increasing ambient temperature. Energy resolution also degrades at higher temperatures. Error bars of resolutions fall within plotted points. The calibration-temperature drift data was acquired using detector 5R-76.

temperatures, a practical method is needed to reconstruct events on-the-fly based on these calibrations and temperatures measured in real time. The answer to these two challenges are discussed in detail in the following sections.

4.2 Digital 3-D CdZnTe Response vs. Temperature

Although a fast calibration method is not strictly needed to calibrate a detector at various temperatures, without it, these calibrations become practically impossible. Commercially-used CdZnTe detectors are required to work in a wide ambient temperature range. This means that if the ambient temperature is not regulated, the system must be calibrated repeatedly at multiple temperatures. Usually, for a fixed temperature, a 3-D CdZnTe detector requires about 10 hours to carry out both 3-D calibration, and the non-linearity calibration. The cost of such calibration will increase linearly if the conventional workflow is repeated.

In subsequent sections, the effect of ambient temperature on different character-

istics of a detector system are discussed and the exact mechanisms causing these changes are presented. For each type of response that changes with temperature, a corresponding algorithm is proposed to correct for the change. All these correcting algorithms try to achieve an identical purpose: assuming a full calibration is already taken at an arbitrary temperature, the algorithms should reduce the "marginal cost" of calibrating the system at another temperature by as much as possible. Three detectors: 5R-18, 5R-52 and 5R-76 were used in work discussed in this chapter. Each detector was calibrated at 0, 5, 10, 15, 20, 25 and 30 ^{o}C. For ease of discussion, only one detector's data is presented and discussed each time, yet the observations and conclusions were the same for all three of them.

4.2.1 Cell Baseline vs. Temperature

Cell baseline values are subtracted from waveforms on an event-by-event basis (Section 2.2). It was noticed that in VAD_UM v2.2 systems, the cell baseline values are affected by temperature. Figure 4.3 presents the measured cell baseline values in an example channel at 0 ^{o}C and 30 ^{o}C. It could be noticed that for the latter half samples, the cell baseline values at 30 ^{o}C is significantly higher than that at 0 ^{o}C.

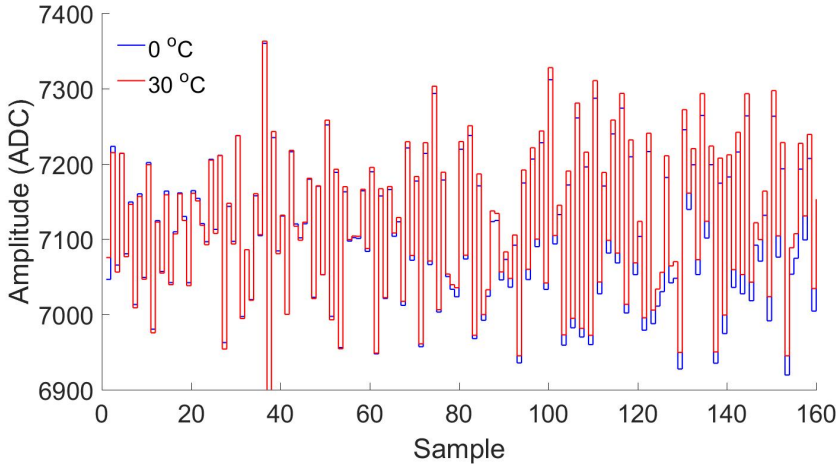

Figure 4.3: Cell baseline values measured in an example channel at 0 ^{o}C and 30 ^{o}C in the tested system. Error bars are negligible.

To show the effect more clearly, the cell baselines at 0 ^{o}C are subtracted from those measured at various temperatures: 0, 10, 20 and 30 ^{o}C. The results are presented in Figure 4.4. In each sample cell, the baseline increases monotonically as a function of temperature, and the trend is almost linear. In addition, this trend of increase is most significant for cell samples in the end of the 160 sample cells in each channel. The exact cause of this trend is unclear, because the micro-structures of the ASICs are unknown.

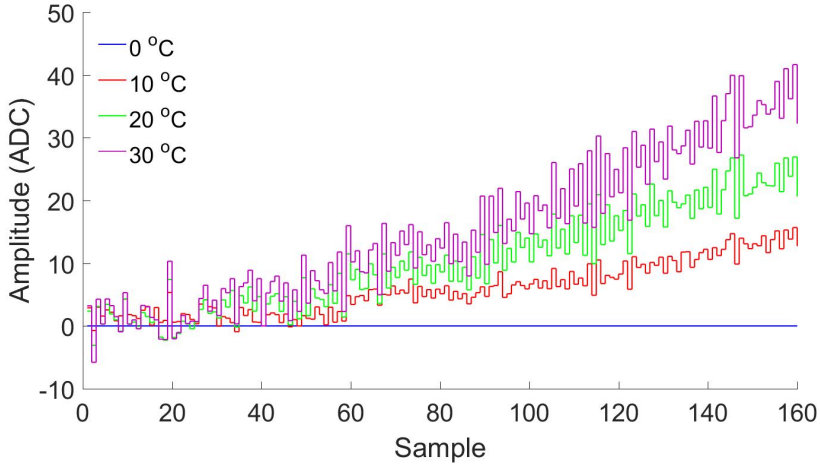

Figure 4.4: Differences between the cell baseline values measured at different temperatures, and the baseline values at 0 ^{o}C. Error bars are negligible.

The change of cell baseline values as a function of temperature must be corrected to achieve good performance. Consider the cell baselines measured at 0 and 30 ^{o}C, the same waveform after cell baseline subtraction can differ in amplitude by up to 30 ADC. It should be pointed out in real measurements, an event can take place anytime (Section 2.2). This means that instead of a constant change of amplitude, an extra random noise will be introduced if the cell baseline calibration for a different temperature is used. Fortunately, because the cell baseline values increase almost linearly with temperature, in real measurements, the cell baseline for each temperature can be estimated by linear interpolation and extrapolation, as long as the system's cell

baseline values are measured at more than one temperatures. Because cell baseline can be measured relatively fast (within 3 minutes for a detector), no improvements in algorithms are needed.

4.2.2 Channel-by-Channel Gain vs. Temperature

The change in 661.7 keV peak cutoffs (AC_i and CC in Equation 2.8) with ambient temperature is shown in Figure 4.5, illustrating that ambient temperature substantially affects channel-by-channel gain. This observed, temperature-dependent gain stems from gain fluctuations in both the detector and readout electronics.

External test pulses were used to isolate electronic gain for each ambient temperature without the detector connected. Relative changes in channel-by-channel gain from ^{137}Cs measurements, which combine electronic and charge collection efficiency, and test pulses, which uses electronics alone, are highly correlated as shown in Figure 4.5. This implies that the change of electronic gain with temperature is the main cause of channel-by-channel gain change with temperature in ^{137}Cs measurements. Furthermore, channel-by-channel gains are seen to decrease almost linearly with increasing ambient temperature.

It should be noted that the measurement of 661.7 keV events spectra cutoffs, AC_i and CC, only require very little measurement data to estimate. In practice, one could accurately measure these cutoffs using a measurement that lasts only several minutes. Hence, the observations in Figure 4.5 do not necessarily provide insights about how to further reduce the required calibration time. However, they indicate that if two or more calibrations were taken at various temperatures, one should be able to carry out a linear regression between the cutoff and temperature in each channel. Such a regression is expected to predict the cutoffs at other temperatures accurately to a first order.

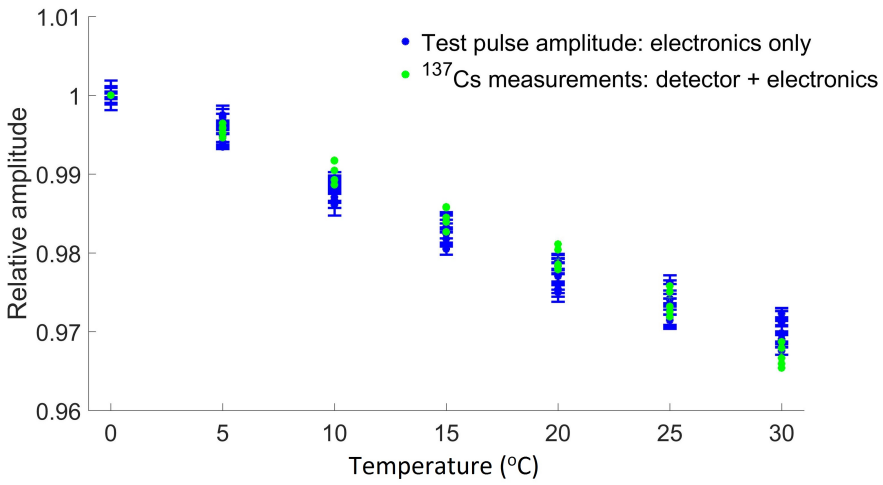

Figure 4.5: Relative gain change with temperature, measured using both a ^{137}Cs source and test pulses. Plotted data are from arbitrarily-chosen channels in detector 5R-52. Strong agreement between changes in electronic and total gain are seen. The uncertainty in ^{137}Cs measurements is negligible.

4.2.3 Electron Mobility-Lifetime Product vs. Temperature

Previous studies already showed that as temperature (T) decreases, the electron mobility-lifetime product ($\mu_e(T)\tau_e(T)$) can increase in CdZnTe detectors [44]. Because of the high performance in digital 3-D CdZnTe detectors, even very small change in $\mu_e(T)\tau_e(T)$ can still cause non-negligible performance degradation. Figure 4.6 presents the measured $\mu_e(T)\tau_e(T)$ values for some example anode channels in detector 5R-76. These Redlen crystals also showed decreased $\mu_e(T)\tau_e(T)$ at higher temperatures.

In i-th channel, the gain-depth curve measured at ambient temperature T, can be described using a simplified model

$$g(i,z,T) = g_e(T)\Delta\varphi(z)exp(-\frac{z}{\mu_e(T)\tau_e(T)E}) \tag{4.1}$$

where $g_e(T)$ represents the electronic gain in channel i, $\varphi(z)$ represents the weighting potential at depth z, and E represents the electric field in the detector. This simplified

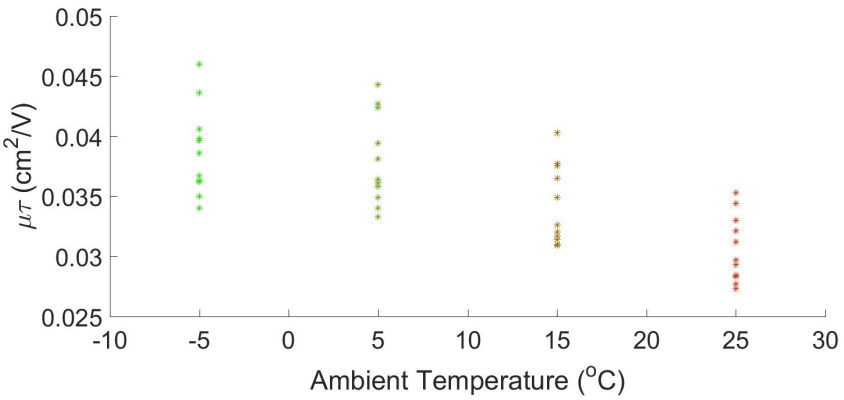

Figure 4.6: Measured $\mu_{e,T}\tau_{e,T}$ values for arbitrarily selected anode channels in detector 5R-76.

model has three assumptions. First, the mobility-lifetime product of electrons in each CdZnTe detector is independent of depth z. Second, the electric field E is uniform inside the detector. Third, signal induction from the drift of electrons only happen when the electrons are in the vicinity of the collecting anode. This assumption is not exactly accurate, but it provides a convenient way to model the effect of temperature change on the gain-depth curves in 3-D CdZnTe detectors.

Figure 4.7 shows gain-depth curves for a single anode channel of detector 5R-52. As discussed in Sec. 2.3, the gain is estimated by measuring the 661.7 keV photopeak centroid in each voxel. These measured gain-depth curves in 3-D CdZnTe detectors are complex in shape. However, the effect of ambient temperature T on gain-depth curves can be approximated using a simpler trend as long as the same bias is applied on the detector. The $\mu_e(T)\tau_e(T)$ values measured in recent Redlen CdZnTe detectors are usually on the same order of magnitude of 1E-2 cm^2/V [37]. Hence, by Taylor expansion [45], Equation 4.1 can be approximated as

$$g(i,z,T) = g_e(T)\Delta\varphi(z)(1 - \frac{z}{\mu_e(T)\tau_e(T)E}) = \Delta\varphi(z)(A(T) + B(T)z) \tag{4.2}$$

where $A(T)$ and $B(T)$ are used for easier discussion. They are defined as:

$$A(T) = g_e(T), \tag{4.3}$$

$$B(T) = -g_e(T)\frac{z}{\mu_e(T)\tau_e(T)E}. \tag{4.4}$$

Since electron trapping only causes a relatively small deficit in signal amplitude, $|B(T)| << |A(T)|$ for all T in the range of this discussion. As a result, the relationship between the gain-depth curves for two different temperatures (T and T_0) in the same anode channel can be simplified using Taylor expansion:

$$\begin{aligned}
\frac{g(i,z,T)}{g(i,z,T_0)} &= \frac{A(T)+B(T)z}{A(T_0)+B(T_0)z} \\
&= \frac{\frac{A(T)}{A(T_0)}+\frac{B(T)}{A(T_0)}z}{1+\frac{B(T_0)}{A(T_0)}z} \\
&= \frac{(\frac{A(T)}{A(T_0)}+\frac{B(T)}{A(T_0)}z)(1-\frac{B(T_0)}{A(T_0)}z)}{(1+\frac{B(T_0)}{A(T_0)}z)(1-\frac{B(T_0)}{A(T_0)}z)} \\
&= \frac{\frac{A(T)}{A(T_0)}+(\frac{B(T)}{A(T_0)}-\frac{A(T)B(T_0)}{A(T_0)^2})z-\frac{B(T)B(T_0)}{A(T_0)^2}z^2}{1-(\frac{B(T_0)}{A(T_0)}z)^2} \\
&\approx \frac{A(T)}{A(T_0)}+(\frac{B(T)}{A(T_0)}-\frac{A(T)B(T_0)}{A(T_0)^2})z.
\end{aligned} \tag{4.5}$$

Equation 4.5 implies that although the gain-depth curve for a channel in 3-D CdZnTe detectors is complex, the relative change of the curve between the ambient temperature of T_0 to T can be approximated as a linear function. The linear functions variable is depth z, and its intercept and slope are affected by T and T_0. Assume a complete calibration measurement has been taken at ambient temperature T_0, and another, shorter measurement is taken at ambient temperature T. During the short measurement at ambient temperature T the space under each channel can be divided into coarser depth bins. Photopeak centroid amplitudes from interactions in these

coarse depth bins can be used in a linear fitting to estimate Equation 4.5. This avoids the time consuming collection of 200 photopeak counts per voxel required in full calibrations (Section 2.3). As a result, a short measurement at T is enough to estimate the gain-depth curve at T. In this study, a complete calibration measurement using ^{137}Cs usually takes about 2 hours. However, with a complete calibration at T_0, 15 minutes of measurement at other ambient temperatures proved sufficient to estimate the gain-depth curves for all anode channels as shown in Figure 4.7. It should be noted that in this example, the curves slightly decrease when z is very close to 40 (interactions are close to the cathode). The most possible cause is artifacts in the reconstruction because sometimes events with failed depth reconstructions are directly assigned a value of 40. These events can happen anywhere in the detector. According to the curve, non-cathode-side events have decreased signal amplitudes compared to cathode-side events. As a result the peak centroid is slightly lower than expected.

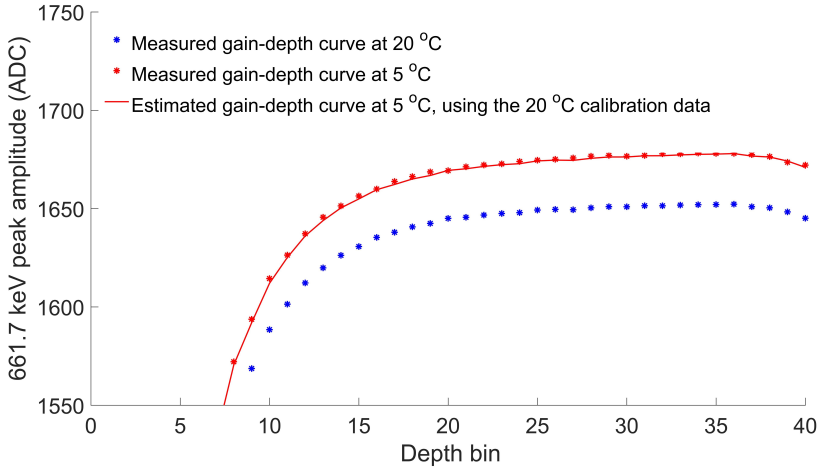

Figure 4.7: An example comparing the estimated and measured gain-depth curves at 5^oC for an anode channel in 5R-18. The estimation is based on the linear relationship in Equation 4.5, using data from a complete calibration at 20^oC and a short measurement at 5 ^oC. Error bars are negligible and omitted in the figure.

The relationship between drift time and depth in each channel, called the timing-

depth curve, also changes with ambient temperature because the mobility of electrons decreases for higher ambient temperatures. As presented in Figure 4.8, at higher temperatures, the electron drift time from the same interaction location to the collecting anode increases. If the timing-depth curves measured at 5^oC are used to reconstruct events measured at 25^oC, the depths of interactions will be systematically overestimated by up to over 1 mm, thus degrading the resolutions of both energy spectrum and Compton imaging. Fortunately, the measurements showed that in each channel, the timing-depth curve for ambient temperature T can be easily estimated by scaling the same curve from a complete calibration at T_0 by a constant value. This value can be easily calculated by measuring the maximum drift times at both temperatures. The maximum drift time corresponds to interactions from the cathode side (z=40), and can be easily measured using only several minutes of measurement.

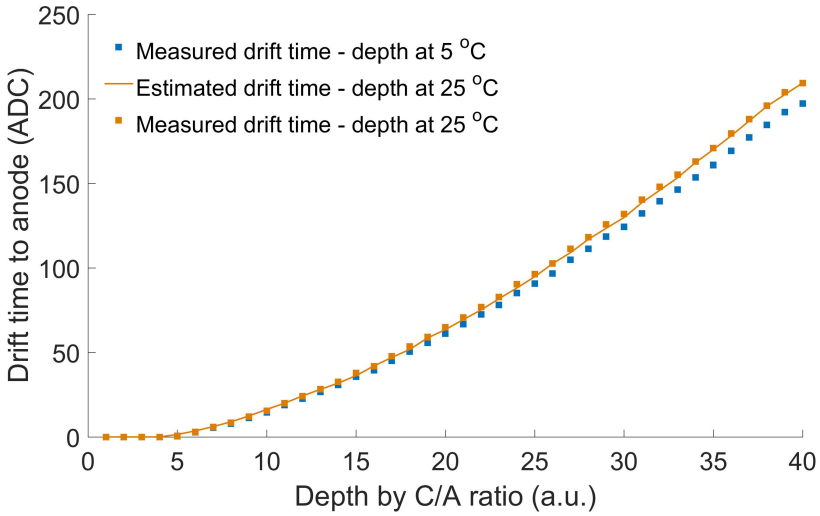

Figure 4.8: An example comparing estimated and measured timing-depth curves at 25^oC for one anode channel. The drift time on the Y-axis is the measured timing difference between the anode and cathode signals. The estimate is calculated by linearly re-scaling the timing-depth curve from a complete calibration at 5^oC by a constant, and the constant is the ratio between the maximum drift times for both temperatures.

4.2.4 Other Detector System Responses vs. Temperature

There are two more important calibrations for 3-D CdZnTe detectors: WPCT calibration and non-linearity calibration (see Section 2.3). These two calibrations also require long measurement time. Fortunately, these two calibrations do not change significantly as temperature changes.

Theoretically, WPCT can change with varying temperature due to changes in electron cloud sizes, because temperature affects the diffusion of electrons. However, such effect should be minimal when the temperature changes from 30 ^{o}C to 0 ^{o}C. Consider the model that approximates the diffusion of electrons as a Gaussian distribution with standard deviation

$$\sigma = \sqrt{\frac{2kTd}{eE}} \tag{4.6}$$

where k is the Boltzmann constant, T is the absolute temperature in the detector, d is the distance of drift, e is unit charge, and E is the electric field in the detector [27]. Even if the temperature in 3-D CdZnTe detector changes from 30 ^{o}C to -40 ^{o}C (303 K to 233 K), for an electron that drifts from the cathode to the anode (15 mm), the FWHM of the diffusion term can only change from 145 μm to 127 μm. Such a change is negligible compared to the average size of electron clouds from interactions above several hundred keV. For example, the average electron cloud size from a 662 keV photoelectric interaction is about 250 μm [18]. Furthermore, in 3-D CdZnTe, WPCT is most significant in the near-anode region. The drift distance d is much smaller for events in this region. As a result, no observable changes in WPCT should be observed in the temperature range discussed in this study. Figure 4.9 compares the measured 661.7 keV peak centroids for two-pixel, side-neighbor events that take place in the edge pixels region. These events have the most significant amplitude deficit from WPCT (see Figure 2.24), yet the effect of temperature on WPCT is still

negligible.

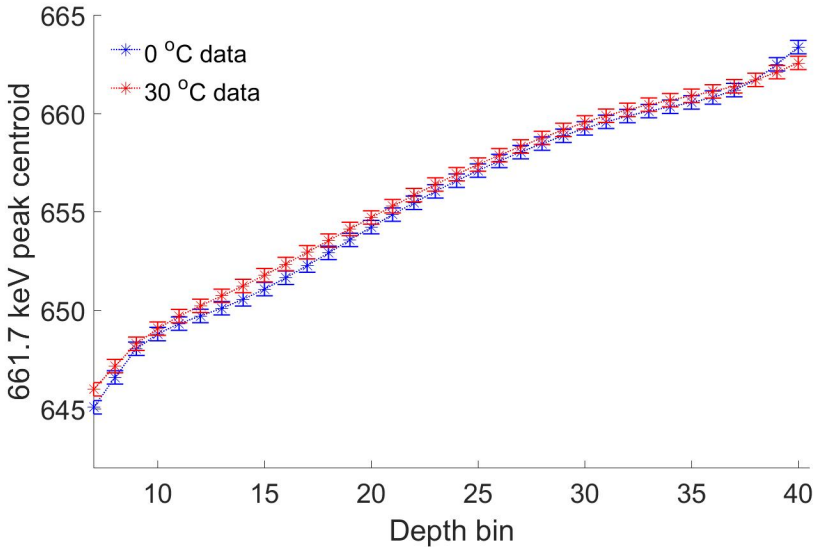

Figure 4.9: An example comparing the WPCT in 2-pixel, SN, edge-pixel events measured in 5R-76 at 0 ^{o}C and 30 ^{o}C. Error bars are 3 times the standard deviation (STD) in the peak centroid from statistical fluctuation.

The effect of temperature on non-linearity is more challenging to predict because it is the aggregated result of temperature effect on all the electronic components in the system, as well as the detector crystal itself. Fortunately, the measurements suggest that the effect of temperature on non-linearity is also negligible, as Figure 4.10 shows.

4.2.5 Performance of Temperature-Corrected Calibration

Based on the analyses in the previous three sections, a complete calibration at T_0 and a fast measurement at T is sufficient to estimate the complete calibration data at ambient temperature T. This estimation process is referred to as temperature-corrected calibration hereafter. ^{137}Cs measurements taken at various ambient temperatures for each detector were reconstructed using both self-calibration and temperature-corrected calibration. The results are compared in Figure 4.11. For both single-pixel and all events, the energy-resolution FWHM at 661.7 keV was only

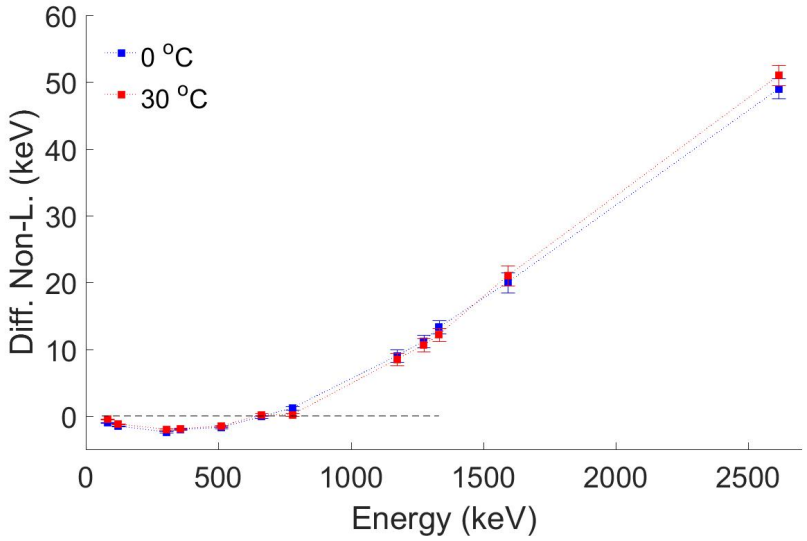

Figure 4.10: An example comparing the differential non-linearity measured at 0 ^{o}C and 30 ^{o}C. Error bars are 3 times STD in the peak centroid from statistical fluctuation. Differential non-linearity represents the difference between the reconstructed peak centroid and the true gamma ray energy.

degraded by 0.02 to 0.03% when using temperature-corrected calibration compared to self-calibration. However self-calibration requires 2 hours of measurement at each temperature while, in contrast, temperature-corrected calibration only requires an additional 15 minutes for each, additional ambient temperature. Within 0 to 30 ^oC, with a 5 ^oC step size, the total calibration time, neglecting non-linearity correction, was reduced from 14 to 3.5 hours when using temperature-corrected calibration. The reduction of time complexity is even more significant if non-linearity is considered. Multi-pixel event results from 5R-18 were omitted as many anode channels showed significant gain deficits. The exact reason of this problem is under investigation and is discussed with some preliminary results in Section 6.5.2.

4.3 Transient Temperature Tests

Ambient temperature is expected to fluctuate in practical, in-field measurements using hand-held, CdZnTe devices without temperature regulation. A temperature

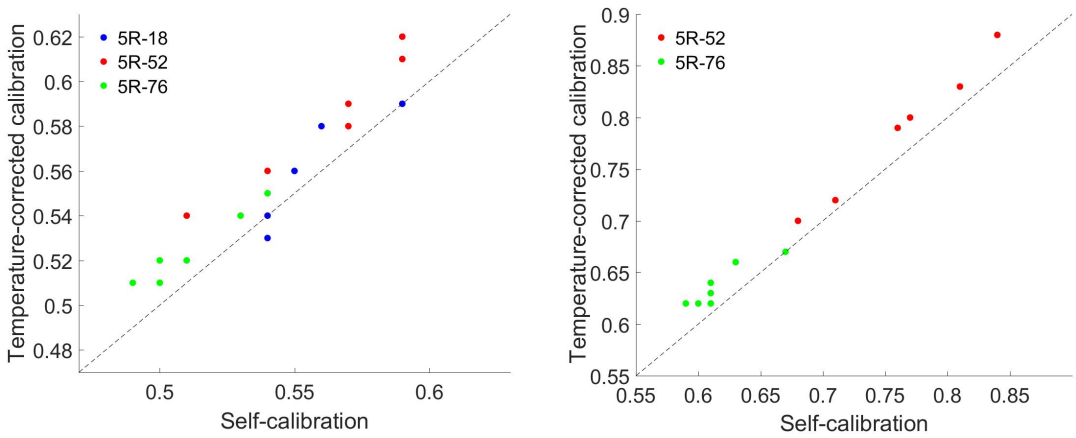

(a) Single-pixel events energy resolution

(b) All events energy resolution

Figure 4.11: ^{137}Cs measurements were conducted at 0, 5, 10, 15, 20, 25 and 30 ^{o}C ambient temperatures for each detector and reconstructed using conventional, self-calibration and time-efficient, temperature-corrected calibrations. Dashed lines represent $y = x$, corresponding to no loss in performance relative to the self-calibration benchmark. Data points above this line represents degradation of resolution.

sensor on the VAD_UM v2.2 ASIC can be used to measure ASIC and detector temperatures (the ASIC is directly coupled to the 3-D CdZnTe detector). As shown in Figure 4.12, the ASIC temperature sensor output was linearly related to the ambient temperature of the environmental chamber. However, it should be noted that the measurement was made with the system at thermal equilibrium. In fluctuating ambient temperatures, the ASIC temperature sensor is not guaranteed to truly reflect the detector temperature because of heat transfer and gradient.

Temperature-based event reconstruction can be summarized into two steps. First, a complete calibration and subsequent fast measurements are used to estimate the temperature-corrected calibration data in a temperature range with a certain step size. Second, the calibration data for each temperature is then mapped to a corresponding ASIC sensor output. Linear interpolation is used in real measurements to estimate the calibration data based on the ASIC sensor output for each event.

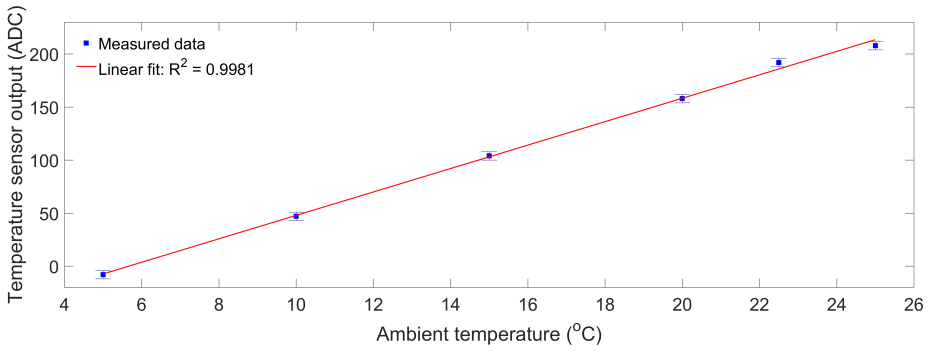

Figure 4.12: Comparison between the ASIC temperature sensor and the ambient temperature setting.

A practical performance evaluation of the temperature-based reconstruction method was made by quickly changing ambient air temperature during a measurement. To start, each detector was at equilibrium with the environmental chamber set to 25 ^{o}C. The environmental chamber was then set to 5 ^{o}C and an one-hour, ^{137}Cs flood irradiation from the detector cathode side was started. One hour measurement duration was chosen to ensure that the detector temperature reached the new equilibrium. Drierite was used in the environmental chamber to mitigate condensation. In the field, a hand-held CdZnTe device might experience a similar change in ambient temperature when the user enters or exits a building. Figure 4.13 presents the temperature reading during this period.

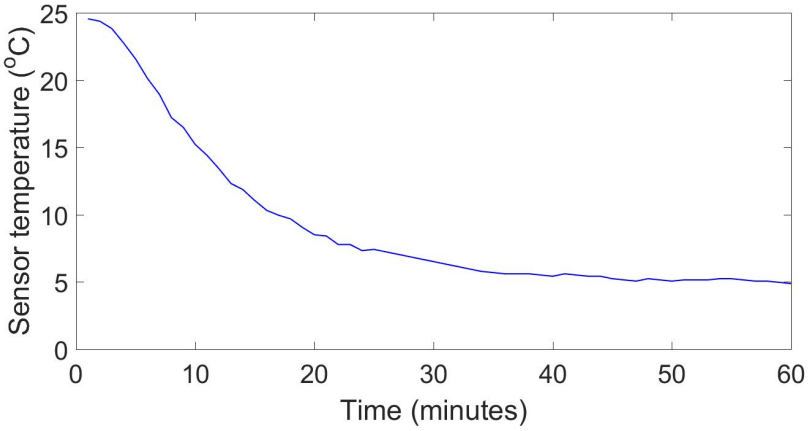

Figure 4.13: Temperature sensor reading during the transient temperature test.

Table 4.1: Energy resolution FWHM at 662 keV for different measurements and reconstructions: 25 ^oC measurements are reconstructed using self-calibration while transient measurements were reconstructed using temperature-corrected calibrations. Multi-pixel events results from 5R-18 are omitted due to gain variation problems.

Detector	**Event types**	**25^oC equilibrium** [a]	**25 to 5 ^oC fast change** [b]
5R-18	Single-pixel	0.55%	0.62%
5R-52	Single-pixel	0.58%	0.61%
5R-52	All events	0.68%	0.73%
5R-76	Single-pixel	0.53%	0.61%
5R-76	All events	0.63%	0.71%

[a] Reconstructed using self-calibration.
[b] Reconstructed using temperature-corrected calibration.

As Table. 4.1 shows, the energy resolution of temperature-corrected measurements during the transients were worse than steady-state results in Figure 4.11. This degradation was expected, since the ASIC sensor will not always truly reflect the temperature on the detector when ambient temperature changes rapidly. Still, the most significant degradation was within 0.1% FWHM. Figure 4.14 shows the single-pixel events spectrum peak shape using the temperature-based reconstruction method during the transient. In comparison, it also presents the peak shape when only one calibration is used during the temperature transient. It should be noted that when only one calibration dataset is used, the energy resolution of the resulting spectrum was degraded to 0.82%. In addition, the complex peak shape cause by gain-drift make it difficult for peak fitting algorithms to distinguish gamma-ray lines that are close in energy.

4.4 Real-Time, On-the-Fly Energy Reconstruction

The environmental chamber is still not exactly the same as the real measurement scenarios. To fully demonstrate the performance of the temperature-based reconstruction, 5R-76 was selected to use in a series of real-time, on-the-fly event recon-

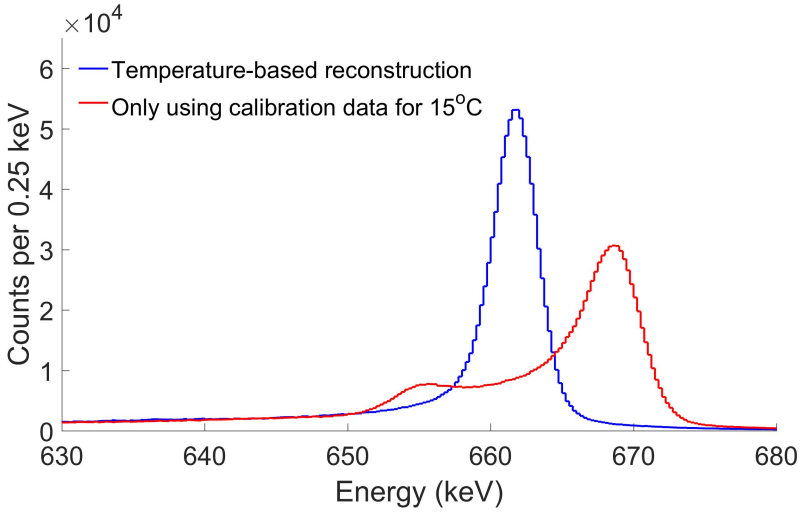

Figure 4.14: Single-pixel events spectra, reconstructed by both temperature-based reconstruction and only one calibration dataset for 15 ^{o}C. Events were from 5R-52, 25 to 5 ^{o}C fast change (Table. 4.1).

structions. This detector was chosen because it was anecdotally the best detector, as shown in Table 4.1. The experiment took place in 2019 February, 20 months after the calibrations were carried out, hence they were also used to verify the long-term stability of the temperature-based calibrations.

In the experiment, the detector system and the DAQ computer were loaded onto a cart inside the laboratory, with the ambient temperature at about 23 ^{o}C. The cart was then pushed out of the building into the open area. The ambient temperature outdoors was about -7 ^{o}C. The DAQ was enabled and events were reconstructed on-the-fly while the system was cooled down. Figure 4.15 presents the setup of the system outdoors. After the system reached equilibrium, the cart was moved back into the building with the DAQ and reconstruction continuously working. Figure 4.16 presents the measured temperature sensor reading from one of the experiments. It could be noticed that the temperature readings were convex and concave curves as a function of the time at the start of the two measurements. This was because the temperature difference between the system and the environmental was the biggest in

the beginning of both phases.

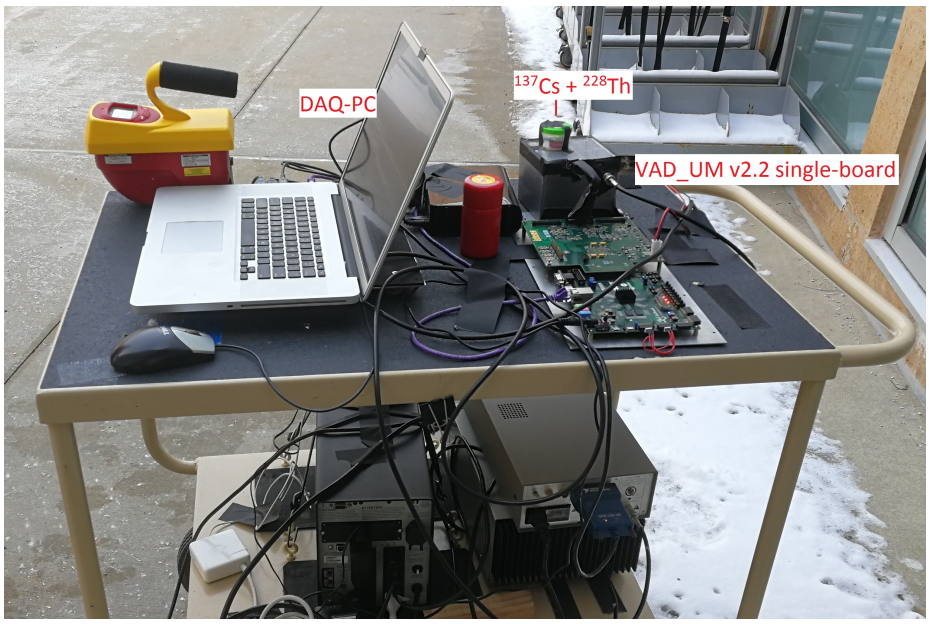

Figure 4.15: Setup of the system outdoors.

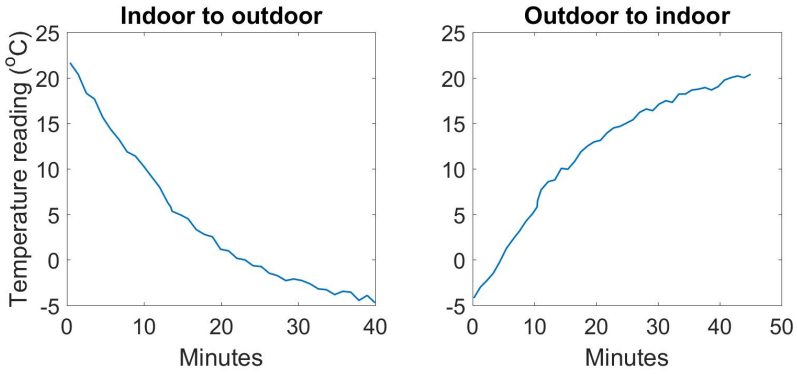

Figure 4.16: Output of the temperature sensor during the two phases of the detector movement.

The measured gamma ray events were reconstructed on-the-fly. The temperature-corrected calibration data was generated using one complete calibration at 20 ^oC and three 20-minute ^{137}Cs measurements at 0, 10 and 30 ^{o}C taken 20 months prior to the experiment. Figure 4.17 presents the reconstructed events spectra from both phases.

The energy resolution for 662, 1592 and 2614 keV are presented in Figure 4.18. In comparison, the energy resolution from self-calibration at 20 ^{o}C is also presented.

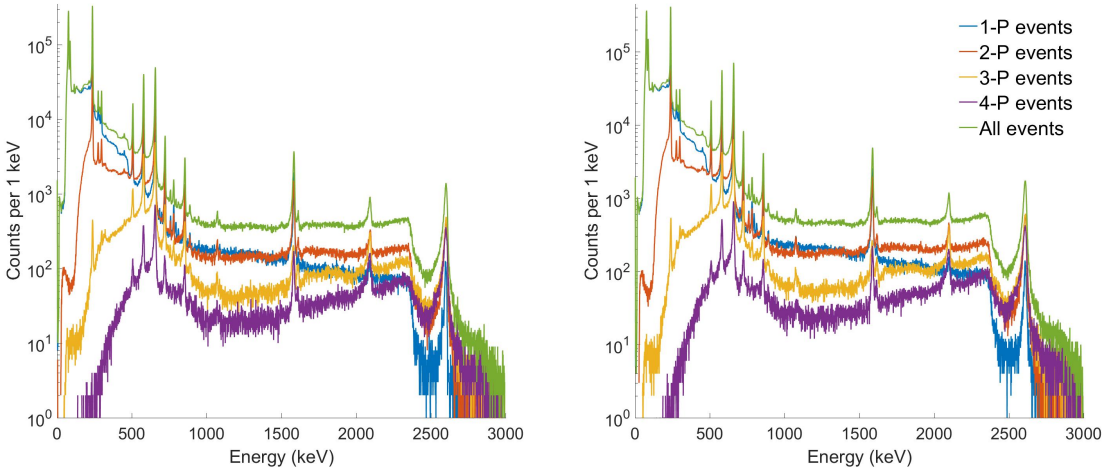

(a) indoors to outdoors (b) outdoors to indoors

Figure 4.17: Events energy spectra reconstructed on-the-fly using temperature-based reconstruction.

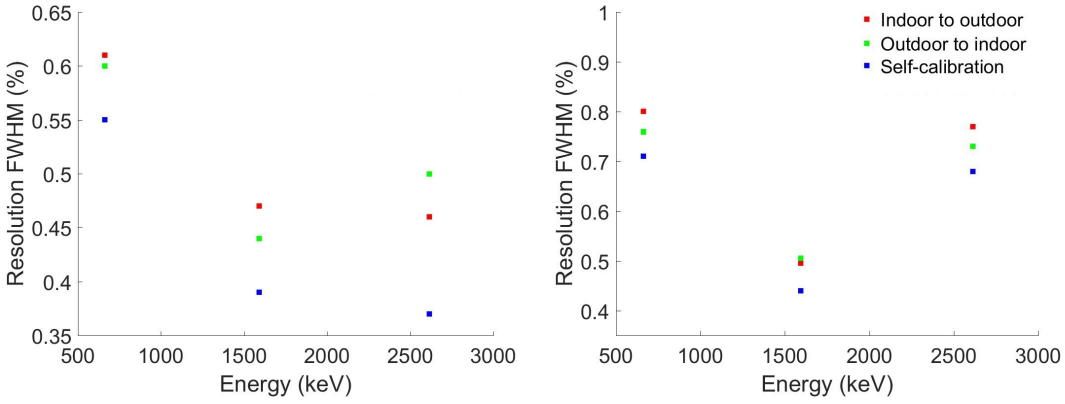

(a) Single-pixel events (b) All events

Figure 4.18: Energy resolution achieved in both phases of the on-the-fly temperature-based reconstruction tests.

Note the resolution from self-calibration at 661.7 keV was different from that in Table 4.1. The data shown in Figure 4.18 was measured in 2019 to ensure fairness of comparison, and the threshold was lowered. As a result, more multi-pixel events were read out and the all events resolution was worse than that in Table 4.1. It should be noted the single-pixel events energy resolution at 2614 keV was less trustworthy due to limited count time. The all events resolution (in percentage) at 1592 keV was better compared to that at 2614 keV because 1592 keV events were all pair-production, double-escape events. Less multi-pixel events were detected at this energy compared to 2614 keV. As a result, the all events resolution at 1592 keV is affected less significantly by multi-pixel events that have worse resolution.

Overall, no more than 0.1% FWHM resolution degradation was observed at all energies. To fully understand the source of this resolution degradation, the reconstructed 2614 keV, single-pixel events peak centroids were compared against the measurement progress as Figure 4.19 presents. It could be seen that when the cart moved from indoors to outdoors, the reconstructed events energy was underestimated, then gradually recovers to the expected energy. Conversely, when the cart moved from outdoors to indoors, the energy was first overestimated, then recovers. The observation suggests that the temperature sensor on the ASIC chip is more sensitive to temperature change compared to the readout electronics. In the first phase, the temperature on the sensor decreased faster than that on the anode channels. As a result, based on the reconstruction algorithm (Equation 2.9) the gain was overestimated and the energy was underestimated. In the second phase, the temperature on the sensor increased faster than that on the anode channels. As a result, the gain was underestimated and the energy was overestimated.

To further validate this hypothesis, the reconstructed 661.7 keV, single-pixel events during the "indoors to outdoors" phase are presented in Figure 4.20. It could be seen that the peak centroid at 661.7 kev also varied in a similar way to that in

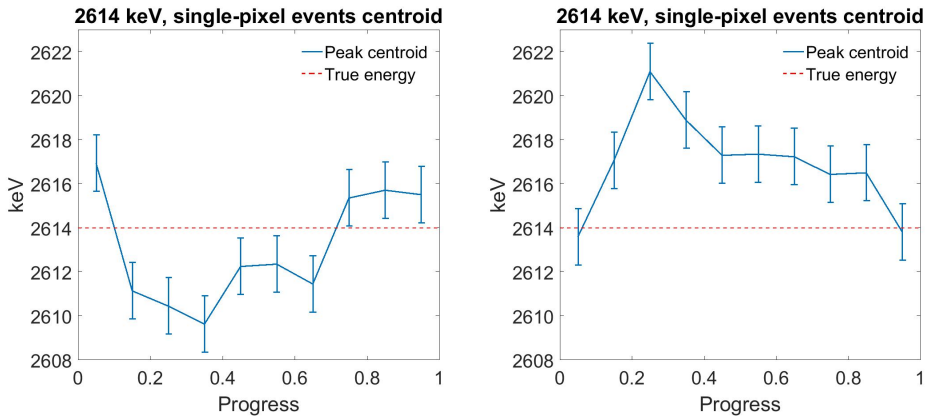

(a) indoors to outdoors (b) outdoors to indoors

Figure 4.19: Reconstructed 2614 keV, single-pixel events peak centroid vs. progress of measurement. The red dashed lines represent the true energy at 2614 keV. Error bars are three times the STD.

4.19(a). In addition, the energy resolution in each period was better than 0.6%, except for the first 10% of measurement when the temperature gradient was the most significant between the detector system and the environment. The resolution decreased anecdotally, most likely due to a decrease of electronic noise as the temperature decreased. The effect of temperature on electronic noise in this detector is shown in detail in Figure 4.22. The fact that most of the partitioned measurements showed good single-pixel events resolution at 661.7 keV indicates that the temperature-based calibration worked successfully for each channel at each depth. The main reason of the resolution degradation came from the peak centroid variation in the whole detector, which was caused by the hypothesized difference in temperature sensitivity between the sensor and the readout electronics.

In further analyses, the recorded events from the above experiment were also reconstructed using the same algorithm, but only two calibrations: one complete calibration at 20 ^{o}C and one 20-minute measurement at 0 ^{o}C. No further resolution degradation was observed. This agrees with the expectation because the resolution degradation due to the inaccuracy in temperature sensor was the dominant factor,

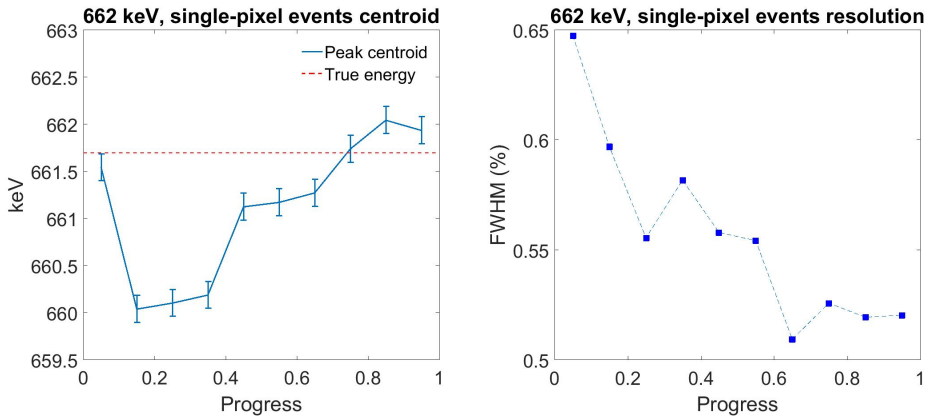

(a) Peak centroid (b) Energy resolution FWHM

Figure 4.20: Reconstructed 661.7 keV, single-pixel events peak centroid and FWHM vs. progress of measurement. The red dashed line represents the true energy at 661.7 keV. Error bars are three times the STD.

compared to the anecdotal resolution degradation due to the inaccuracy of the estimated calibration data, shown in Figure 4.11.

4.5 CdZnTe Detector at High Temperature

In some scenarios, a user might have to operate a detector at very high ambient temperatures up to 40 ^{o}C. For example, in certain regions of a nuclear power plant, the temperature can be very high. Operation of detectors in high temperatures is challenging because the leakage current (I) increases as a function of temperature

$$I \propto e^{-\frac{E_g}{2k_BT}} \tag{4.7}$$

where E_g is the band gap, k_B is Boltzmann constant and T is the absolute temperature [46]. At higher temperatures, the leakage current can increase significantly. As a result, the electronic noise in the device will increase and the detector's performance will degrade [18].

Figure 4.21 presents the measured bulk leakage current as a function of temper-

ature in detector 5R76 with a cathode bias of -3000 V. The leakage was measured directly using the high-voltage supply [47]. Again, the temperature was controlled by the environmental chamber. It could be seen at 0 ^{o}C, the leakage current was negligible. As the temperature increases, the bulk leakage increases almost exponentially.

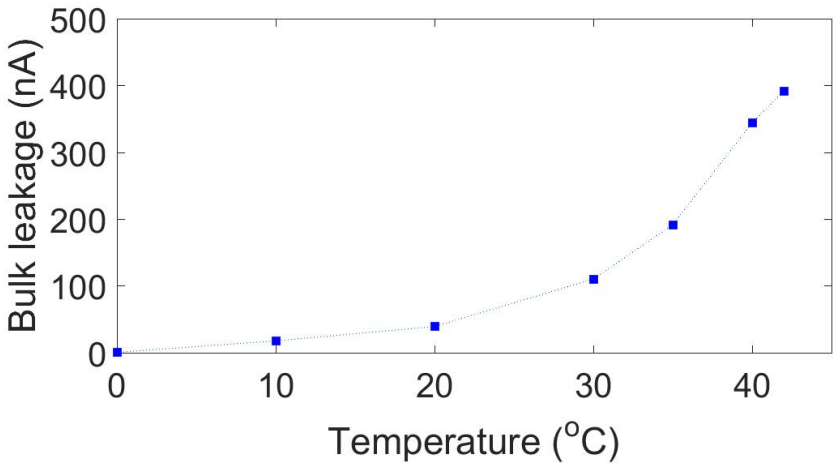

Figure 4.21: Bulk leakage in 5R76 vs. temperature. The bias was -3000 V.

Thanks to the pixelated design, the electronic noise in each anode channel is not significantly affected. Figure 4.22 presents the measured electronic noise as a function of temperature. To highlight the effect of temperature on noise, 700 keV dynamic range was used. It could be seen that at 42 ^{o}C, the average anode noise is still below 3 keV.

Figure 4.23 presents the measured ^{137}Cs single-pixel events energy spectrum at 40 ^{o}C using detector 5R76. 0.53 % resolution FWHM was achieved at 661.7 keV. In comparison, the resolution at room temperature is 0.40 %. Though the performance degrades at 40 ^{o}C, the resolution is still considered very useful in many scenarios.

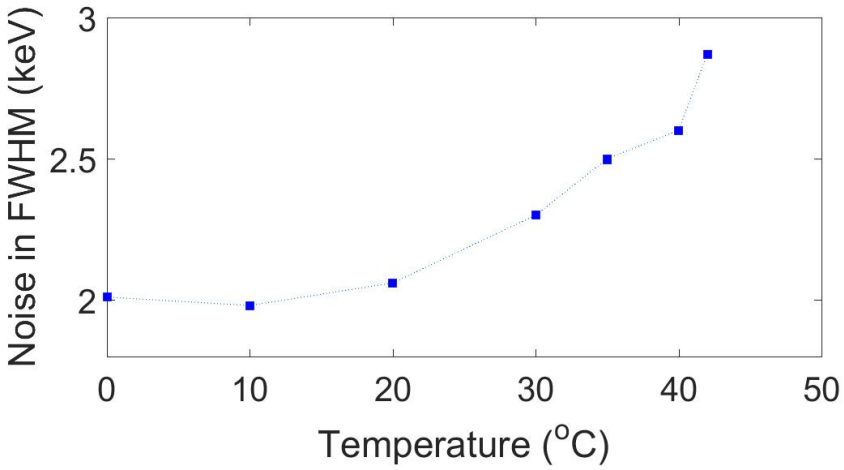

Figure 4.22: Average anode noise in 5R76 vs. temperature. The bias was -3000 V. 700 keV dynamic range was used.

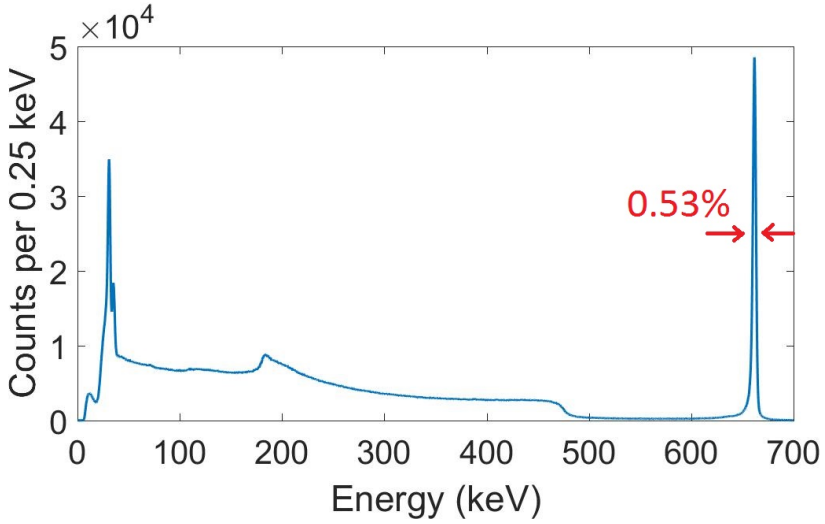

Figure 4.23: Single-pixel events energy spectrum of a ^{137}Cs measurement using 5R76 at 40 ^{o}C.

CHAPTER V

Fast Neutron Damage in 3-D CdZnTe

5.1 Neutron Damage in 3-D CdZnTe Detectors

Previous studies showed that spontaneous fission neutrons with $10^{10}/\text{cm}^2$ fluence, or fast neutrons with $2\times10^8/\text{cm}^2$ fluence, can cause non-negligible extra trapping in CdZnTe [13, 48, 49]. In this work, more detailed experiments about fast neutron damage were made with high-performance, 3-D CdZnTe detectors.

An important metric was developed to quantify the effect of neutron damage in 3-D CdZnTe detectors: increase of cathode-side events electron trapping when the detector cathode is biased to -3000 V. To estimate this value, the "relative gain-depth curve" is first calculated by

$$g_{rel}(i,z) = \frac{g_{post}(i,z)/g_{post}(i,10)}{g_{pre}(i,z)/g_{pre}(i,10)} \tag{5.1}$$

where $g_{pre}(i,z)$ and $g_{post}(i,z)$ represent the measured 661.7 keV photopeak event signal amplitude at depth z in channel i before and after the neutron irradiation. The signal amplitudes for events at depth 10 are used to normalize the electronic gain, which could be affected by temperature (discussed in Chapter IV). The exact depth bin could be chosen arbitrarily. Figure 5.1 presents an example relative gain-depth curve in a channel after neutron irradiation. It could be seen that the curve shows

a positive slope, indicating that more electron trapping was induced from neutron damage in the detector. If the trapping did not change at all, the curve should be constant 1 for all depths assuming perfect precision of measurement. A linear regression could be conducted on this curve and the slope times 40 (the number of depth bins) is used to represent the increase of cathode-side events electron trapping. It should be noted the values of $g_{pre}(i,z)$ and $g_{post}(i,z)$ are acquired from calibrations that use -3000 V on the cathode. For higher or lower biases the increase of trapping is expected to decrease of increase accordingly. In subsequent discussions the value is referred to as "increase of (extra) cathode-side electron trapping".

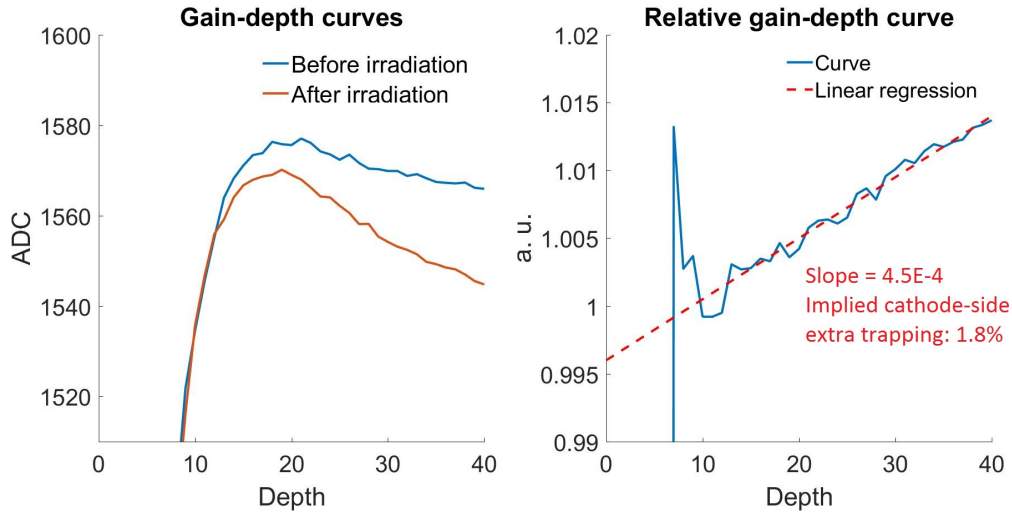

Figure 5.1: Left: gain-depth curves from an example channel before and after neutron irradiation. Right: relative gain-depth curve and estimated cathode-side events extra trapping.

Figure 5.2 presents a comparison between increased cathode-side electron trapping against fast neutron fluence measured in different detectors. The results acquired from the Orion-α and Orion-β detectors are from high-energy gamma ray detection experiments. The setup is presented in Figure 6.1 and will be discussed in detail in Chapter VI. For the other detectors, the irradiation was conducted directly by using a PuBe source to flood irradiate each bare detector. In each experiment, the cathode of the detector was always facing the source. It should be noted that the uncertainty

of neutron fluence for each data point is non-negligible. The values were estimated to a first order, assuming the PuBe source has infinitesimal size. Figure 5.2 shows an expected trend that the more fast neutron fluence could cause more increase of cathode-side electron trapping. However, for the same amount of neutron fluence, different detectors show very different amount of extra trapping. It should be noted that the conditions in the irradiations were not strictly controlled. As a result the effects of cathode bias, temperature and neutron flux are not reported. Interestingly, it could be seen that 3-D CdZnTe detectors are very sensitive to fast neutron fluences. A fast neutron fluence as low as $1\times10^8/\text{cm}^2$ can already cause non-negligible increase of trapping. For reference, the latest Redlen detectors have $\mu_e\tau_e$ values of about 4E-2 cm^2/V. Based on Hecht equation [50], with -3000 V cathode bias, the induced signals on a collecting anode from cathode side events will lose 2% amplitude due to trapping. The experiments show that if a 3-D CdZnTe detector is irradiated by about 1E9 n/cm^2 neutron fluence, the loss can increase by another 2%.

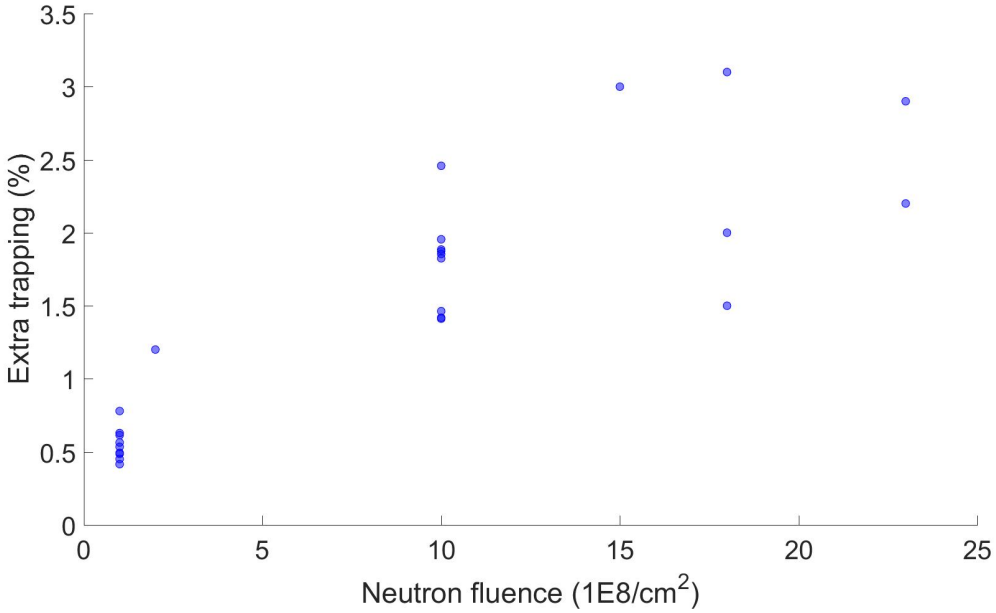

Figure 5.2: Increase of trapping, quantified as cathode-side event signal amplitude decrease (%) with -3000 V bias after different neutron fluence in 3-D CdZnTe.

As discussed in Section 2.3, the gain-depth curves are used to correct for the effect of weighting potential and trapping of electrons in 3-D CdZnTe detectors. As Figure 5.1 shows, neutron irradiation significantly affects the gain-depth curves. As a result a calibration before neutron damage is no longer suitable for measurements using the same detector after neutron damage. An example is shown in Figure5.3. Two ^{137}Cs measurements were taken with detector 5R-69 before and after a neutron irradiation with about $2.3\times10^9/\text{cm}^2$ fluence. In the first measurement (the one before neutron damage), the self-calibration results show 0.52% single-pixel events resolution FWHM at 661.7 keV. Using the calibration from the first measurement to reconstruct the second measurement, the resolution degrades to more than 2%.

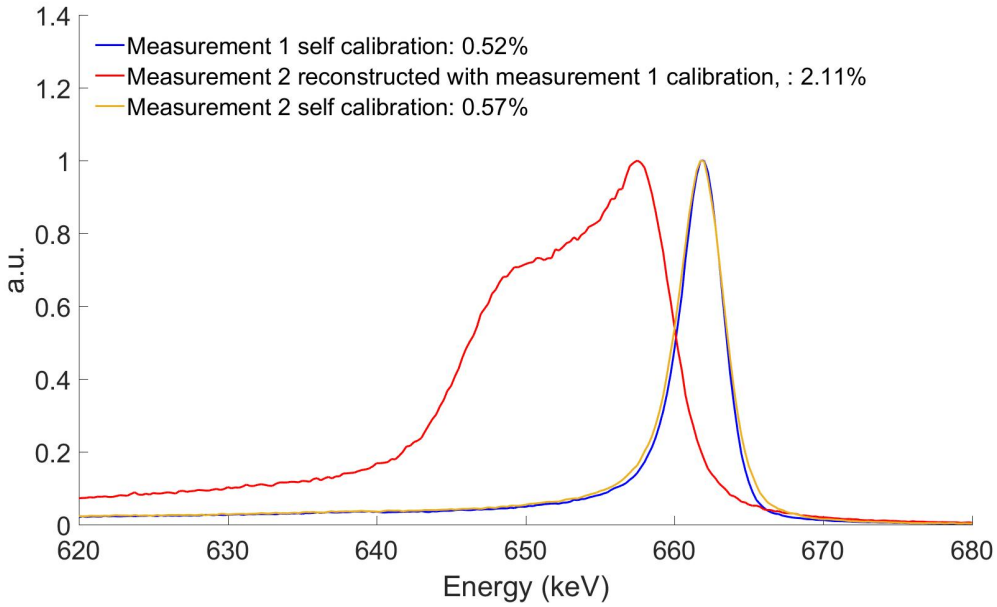

Figure 5.3: Normalized single-pixel events energy spectra from measurements before and after neutron damage, reconstructed using different calibrations.

Figure 5.3 also compares the self-calibration results from both measurements before and after neutron irradiation. It could be seen that although neutron damage can increase electron trapping in CdZnTe, with the position sensing technique the reconstructed resolution is still 0.57%, because the systematic trapping could be measured

and largely corrected. Nevertheless, compared to the resolution of 0.52% FWHM before neutron damage, the degradation is non-negligible. This is because in 3-D CdZnTe detectors the reconstruction only corrects for trapping to $1720 \times 1720 \times 375$ μm^3 voxels. The variation of sub-voxel trapping cannot be corrected. Figure 5.4 compares the resolution FWHM against reconstructed depth of interactions in randomly selected channels before and after the neutron damage in detector 5R-68. The resolution for depth bins below 15 degrades significantly because of the drastic change of weighting potential profile. In the range of depth bin 15 to 20, the resolution values are similar before and after the neutron damage. This indicates that in the two measurements the electronic noise did not change. For depths larger than 20 (close to the cathode side), the resolution values from the measurement after neutron damage increase significantly, because the damage increased electron trapping in the detector. Electrons from interactions closer to the cathode are subject to more trapping because they need to drift all the way to the collecting anodes.

5.2 Annealing of 3-D CdZnTe Detectors in Room Temperature

Previous work have shown that radiation damage in semiconductor detectors could be annealed over time [49]. In addition, the annealing process is faster in an environment with higher temperature [48, 51, 52]. In this work, the annealing of high resolution, 3-D CdZnTe detectors was also experimented with two different ambient temperatures: room temperature and 80 ^oC temperature. The annealing results at room temperature is discussed in this section, while the high-temperature annealing is discussed in Section 5.3.

After the high-energy gamma ray detection experiment discussed in Chapter VI, the nine direct-attachment detectors in the Orion-β system were calibrated multiple

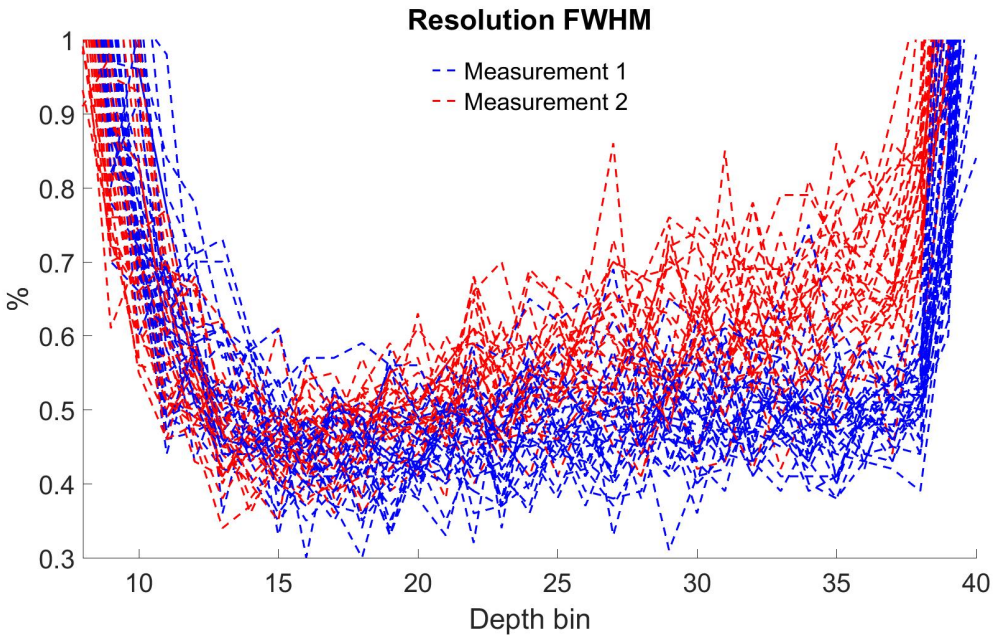

Figure 5.4: FWHM vs. depth for measurements before (measurement 1) and after (measurement 2) neutron damage in 5R-69. Self-calibrations were used for reconstruction. Data is shown on a channel-by-channel basis. The abnormally high values for depths close to 40 (near-cathode events) are artifacts from the reconstruction software.

times in the next several months. In each calibration, the increase of cathode-side electron trapping, relative to the calibration prior to the neutron damage, was calculated again. Equation 5.2 presents the relative gain-depth curve calculation. It is almost identical to Equation 5.1 except that $g_t(i,z)$ represents the calibration result at time t.

$$g_{rel}(i,z) = \frac{g_t(i,z)/g_t(i,20)}{g_{pre}(i,z)/g_{pre}(i,20)} \tag{5.2}$$

The calculated extra cathode-side events trapping (relative to the calibration with no neutron damage) in Orion-β detectors is shown in Figure 5.5. Each data point represents the result averaged over all pixels on one detector. It could be seen that right after irradiation, the cathode-side events trapping increased by about 2%. In 20 days, the extra cathode-side events trapping decreased to about 1.2%. After 120 days, the values decreased to almost zero, indicating a near complete recovery of neutron damage has almost finished. Figure 5.6 and Figure 5.7 present the change of resolution in each detector before neutron damage, immediately after neutron damage and after four months at room temperature. In Figure 5.7 each relative value is calculated by subtracting the FWHM before neutron damage in the same detector from the FWHM from the current measurement. It could be seen that the degraded resolution after neutron damage gradually recovers after four months of room-temperature annealing. The resolution might further improve in the future, if the remaining neutron damage can be further annealed at room temperature.

5.3 Annealing of 3-D CdZnTe Detectors at High Temperature

Section 5.2 shows that fast neutron damage in 3-D CdZnTe detectors could recover within several months at room temperature. However, this process is too slow

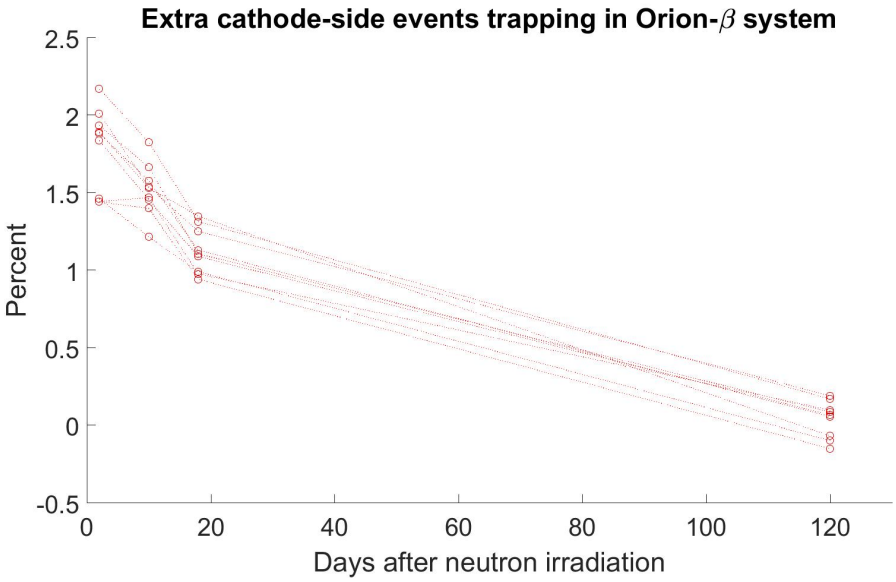

Figure 5.5: Extra cathode-side events trapping compared against the calibration before neutron damage vs. time. Each data point represents one detector. Without any neutron damage a value of zero is expected.

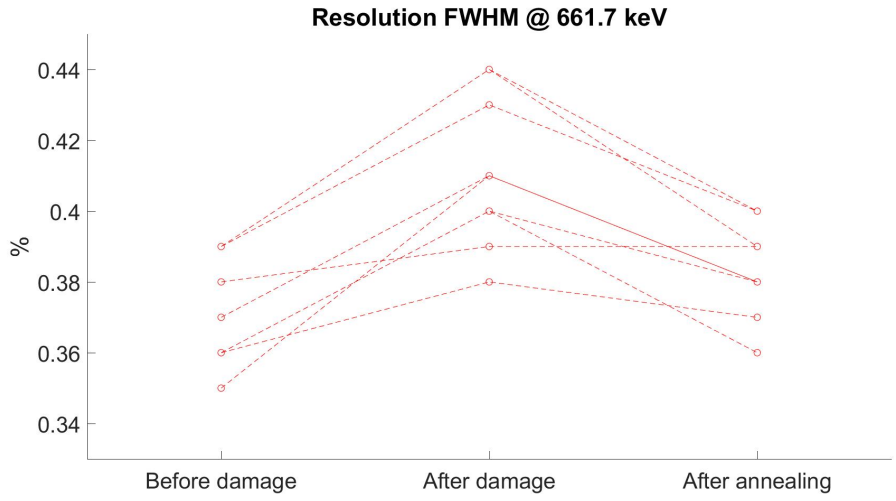

Figure 5.6: Single-pixel events resolution FWHM at 661.7 keV measured in the Orion-β detectors. The annealing process occurred over four months at room temperature. Self-calibrations were used for reconstruction in each measurement.

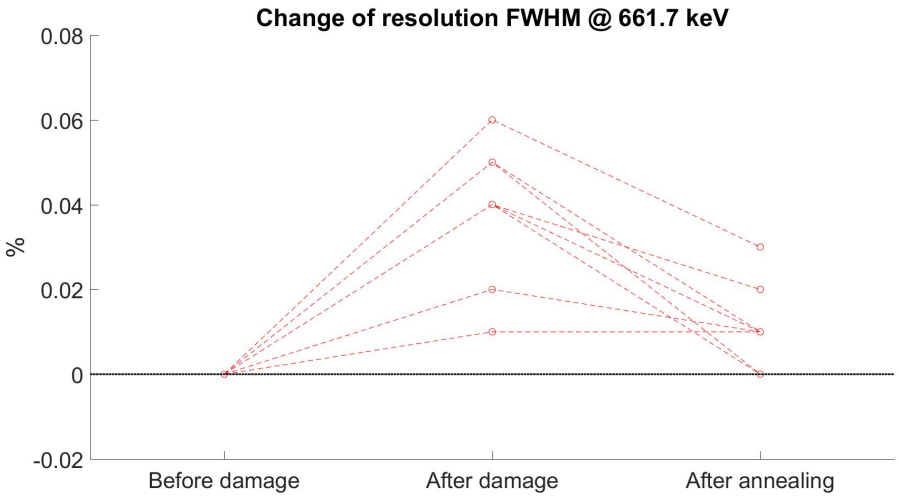

Figure 5.7: Change (relative to the first measurement) of single-pixel events resolution FWHM at 661.7 keV measured in the Orion-β detectors. The annealing process was four months at room temperature. Self-calibrations were used for reconstruction in each measurement. Black dotted line is zero.

for the end users working in fields such as medical physics or active interrogation. To accelerate the annealing process, the 3-D CdZnTe detectors were put inside an environmental chamber at 80 ^{o}C ambient temperature. No bias was applied. The same environmental chamber was used in the temperature-based events reconstruction experiment in Chapter IV.

Seven detectors were annealed at 80 ^{o}C ambient temperature. No higher temperatures were used based on suggestions from Redlen as higher ambient temperatures might damage the fabrication of the detectors. Figure 5.8 presents the results. The calculation algorithm is identical to that in Figure 5.5. It could be seen that in all the detectors, the cathode-side events extra trapping decreased to values below zero after 60 hours of annealing at 80 ^{o}C. These negative values indicate that the annealing at 80 ^{o}C not only eliminates the extra electron trapping from neutron damage, but also further reduce the electron trapping.

It should be pointed out that the results from Orion-β31 was based on another irradiation using a PuBe source, after it has annealed at room temperature as shown

in Section 5.2. This detector was annealed again at 80^{o}C to provide direct comparison and shows that high temperature significantly accelerates the annealing process. It should also be pointed out that the Orion-β31 detector was directly attached to the ASIC. As a result the ASIC was also put in 80-^{o}C environment for about 60 hours. The ASIC worked correctly after the annealing process, indicating tha the electronics can endure the high-temperature annealing process.

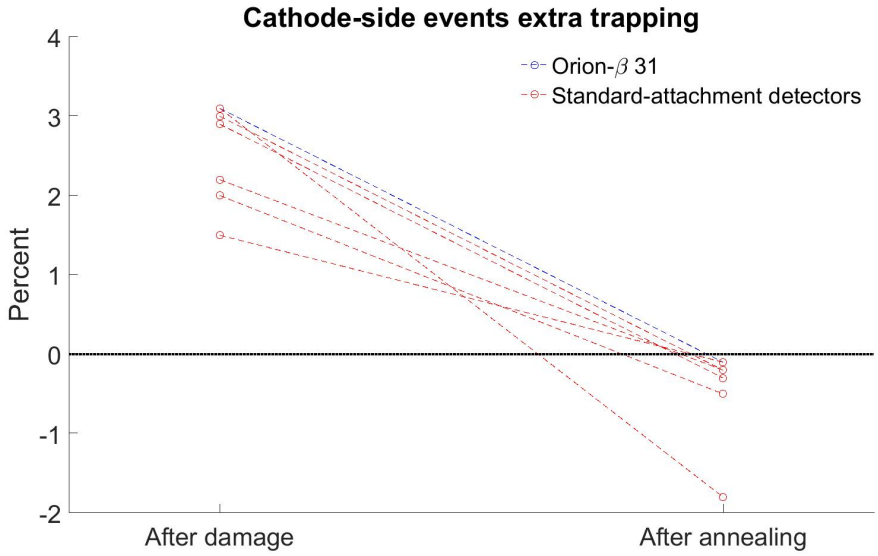

Figure 5.8: Extra cathode-side events trapping compared against the calibration before neutron damage . Each data point represents one detector. Without any neutron damage a value of zero is expected. Black dotted line is zero. Orion-β31 is marked in a different color because it is a direct-attachment detector and tested using a different system.

The reduction in electron trapping after high-temperature annealing also improves the resolution. Figure 5.9 presents the single-pixel events resolution FWHM measured in each detector before neutron damage, after neutron damage and after high-temperature annealing. For easier comparison the relative changes of FWHM values are also shown in Figure 5.10. Each relative value is calculated by subtracting the FWHM before neutron damage in the same detector from the FWHM from the current measurement. It could be seen that the change of resolution is below zero in

all the detectors after high-temperature annealing. The reason is that the electron trapping in each detector after high-temperature annealing is reduced compared to that before the neutron damage, as Figure 5.8 shows.

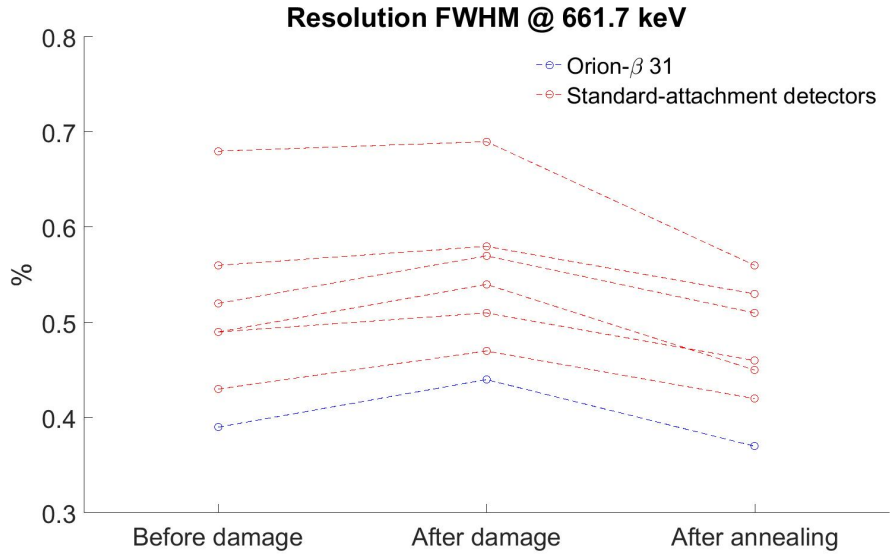

Figure 5.9: Single-pixel events resolution FWHM at 661.7 keV measured in detectors tested with high-temperature annealing. Self-calibrations were used for reconstruction in each measurement. Orion-β31 is marked in a different color because it is a direct-attachment detector and tested using a different system.

It could be seen in Figure 5.9 and Figure 5.10 that one of the tested detectors (5R-32) showed the most significant performance improvement after high-temperature annealing. Compared to the test result before any neutron damage, the single-pixel events resolution FWHM at 661.7 keV improved from 0.68 % to 0.56 %. Figure 5.11 presents the FWHM vs. the depth of interaction in each pixel before neutron irradiation and after high-temperature annealing. It could be seen that before neutron irradiation, the FWHM values close to the cathode side are very poor, indicating that there exists significant sub-pixel variation of trapping in the detector. In many pixels, the FWHM values increase significantly for depth bins above 20. This implies that there is very likely a "layer" with a large amount of defects in the middle of the detector. After the high-temperature annealing, the resolution largely improves

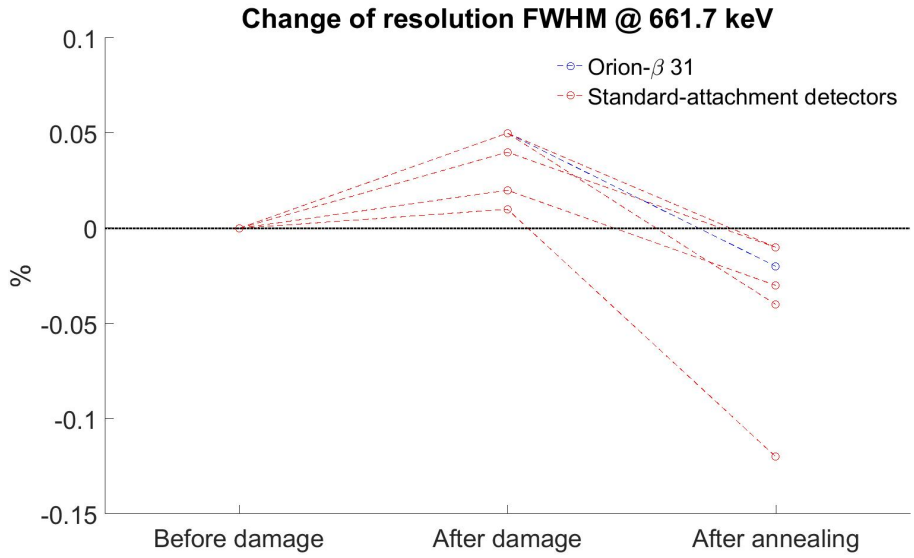

Figure 5.10: Change (relative to the first measurement) of single-pixel events resolution FWHM at 661.7 keV measured in detectors tested with high-temperature annealing. Self-calibrations were used for reconstruction in each measurement. Black dotted line is zero. Orion-β31 is marked in a different color because it is a direct-attachment detector and tested using a different system.

especially for depths over 20. This improvement of resolution as a function of depth signifies the effect of high-temperature annealing on detector performance.

Additional evidence of improvement in material quality could be found by comparing the cathode SRFs from measurements before neutron damage and after high-temperature annealing. As Figure 5.12 shows, the cathode SRFs are much straighter after annealing. Straight cathode SRFs represent uniform electric field in the detector [33]. The observations indicate that high-temperature annealing improves the material uniformity in detector 5R-32 significantly.

5.4 Summary

This chapter discusses the effects of neutron damage in 3-D CdZnTe detectors. With fast neutron fluence as low as $1\times10^8/\text{cm}^2$, non-negligible increase of trapping could be observed in the high-performance, 3-D CdZnTe detectors. The degrada-

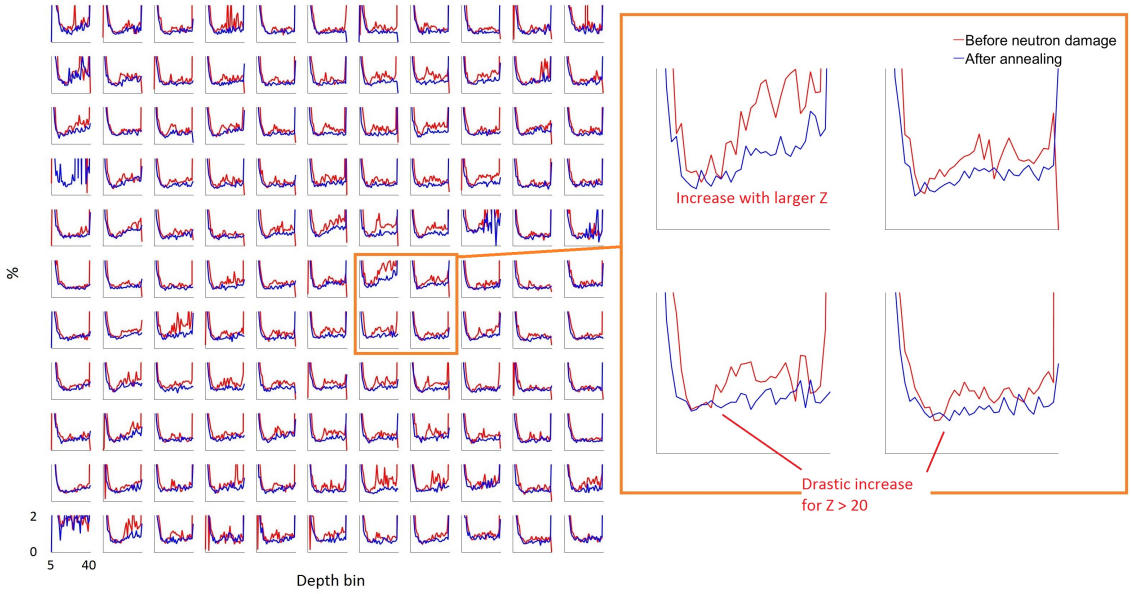

Figure 5.11: FWHM vs. depth for measurements before neutron damage and after high-temperature annealing in 5R-32. Self-calibrations were used for reconstruction. Data is shown on a pixel-by-pixel basis. The abnormally high values for depths close to 40 (near-cathode events) are artifacts from the reconstruction software.

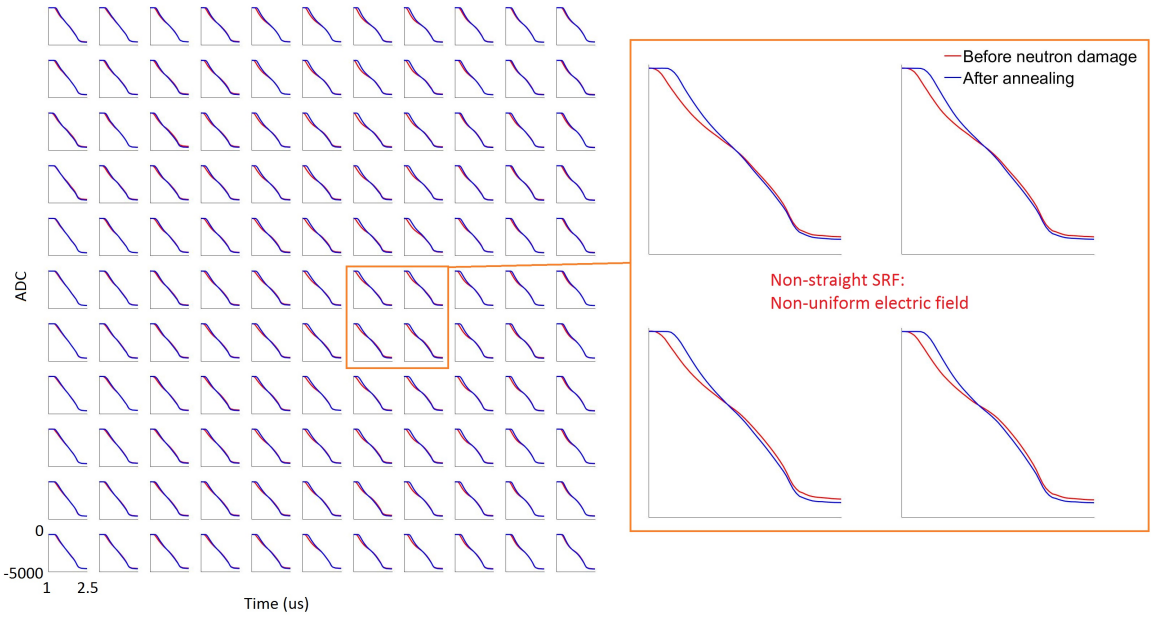

Figure 5.12: Cathode SRFs from measurements before neutron damage and after high-temperature annealing in 5R-32. Data is shown on a pixel-by-pixel basis. Non-straight SRFs indicate non-uniform electric field.

tion is observed at much lower fluences than previous studies, possibly due to the high system performance. Due to increased trapping the energy resolution of 3-D CdZnTe detector degraded significantly. With about 2 % extra cathode-side events trapping induced, room-temperature annealing requires at least 4 months. At 80 ^{o}C, however, this process could be shortened to several days. In the detectors after high-temperature annealing, electron trapping is reduced to be even lower than the initial states before neutron damage was induced. The single-pixel events resolution at 661.7 keV was also improved compared to the no-neutron-damage results. The studies provide valuable information about neutron damage and annealing in high-performance 3-D CdZnTe detectors. For end users in fields such as medical imaging, the high-temperature annealing provides a potential solution to maintain the system's performance as radiation damage accumulates in the long run.

CHAPTER VI

Detection and Measurements of 3 to 7 MeV Pair-Production Double-Escape Interactions

6.1 Introduction

The detection and measurement of high-energy (above 3 MeV) gamma rays can be used for active interrogation [53], nuclear resonance fluorescence [54] and medical imaging [55]. In the past, 3-D CdZnTe detectors were mostly used to detect and measure gamma rays in the energy range of 0 to 3 MeV. At higher energy ranges, the application of 3-D CdZnTe is limited mainly due to low efficiency and readout dynamic range. With the development of large, digital CdZnTe arrays in recent years [13], the detection and measurement of gamma rays above 3 MeV in CdZnTe is becoming feasible. Multiple attempts have been made to measure and reconstruct high-energy gamma-ray interactions in 3-D CdZnTe detector arrays in the past. Boucher used a 18-detector array, read out by analog ASICs, to measure up to 6.1 MeV gamma rays from neutron activation in ^{16}O [35]. However, the analog ASICs dynamic range was limited to 3 MeV. Hence, the only possibility of detecting high-energy peaks are Compton-scattered events that deposit the full energies in the system. Furthermore, with information from analog filters only, the reconstruction of these events was not ideal. As a result, no clear peaks were resolved in the experiments. Later, Streicher

tried to use two CdZnTe detectors, directly attached to VAD_UM v2.2 ASICs (with up to 9 MeV dynamic ranges) to measure high-energy gamma rays. The experiments showed 4.4 MeV gamma-ray peaks from the de-excitation of ^{12}C atoms [13]. However, these gamma rays are significantly Doppler-broadened and performance of high-energy gamma-ray measurements in 3-D CdZnTe detectors is still unclear [56]. In this chapter, experiments using the Orion systems to measure high-energy gamma-rays from neutron activation in ^{35}Cl are recorded. Several mechanisms degrading the energy resolution for high-energy gamma-rays in 3-D CdZnTe detectors are discussed. Practical correction algorithms for some of the issues were developed and discussed in detail.

6.2 Experiments and Initial Results

The high-energy gamma ray measurements in this work mainly focuses on gamma rays from neutron activation of ^{35}Cl. This isotope is naturally abundant, and has a thermal neutron absorption cross section of about 30 barn. ^{35}Cl (n, γ) ^{36}Cl reactions generate a series of gamma rays that are well separated in energy with negligible Doppler broadening. Table 6.1 presents some significant gamma rays from this reaction [57].

Table 6.1: Significant gamma ray lines from ^{35}Cl (n, γ) ^{36}Cl.

Energy (MeV)	Probability (%)
6.111	19.7
7.414	10.0
7.790	8.6

^{238}PuBe(α, n) sources were used to generate fast neutrons in these experiments. A polyvinyl chloride (PVC) target was built to thermalize and absorb the fast neutrons. The target is a 30×30×30 cm^3 cube composed of 12 30×30×2.5 cm^3 boards tiled together. Each of the upper 6 boards has a 4-cm-diameter hole drilled in the center.

In the experiments, a ^{238}PuBe source was put into the central hole of the target. Fast neutrons from the PuBe source were thermalized by hydrogen and carbon atoms in the PVC target, then absorbed mainly by ^{35}Cl atoms. The geometry of the target was determined with considerations for convenience of set up, neutron-to-gamma ray conversion rate and maximizing leaked gamma rays based on non-rigorous MCNP simulations [58]. In each experiment, an Orion system, composed of a 3×3 array of modules using VAD_UM v2.2 ASICs, was used to measure gamma rays from the target. The system was operated with 7 MeV dynamic range. Figure 6.1 presents the setup used in one of the earlier experiments. It should be noted the distance between the Orion system and the target was not strictly determined. In later experiments, the distance was shortened to increase the gamma ray flux in the detectors.

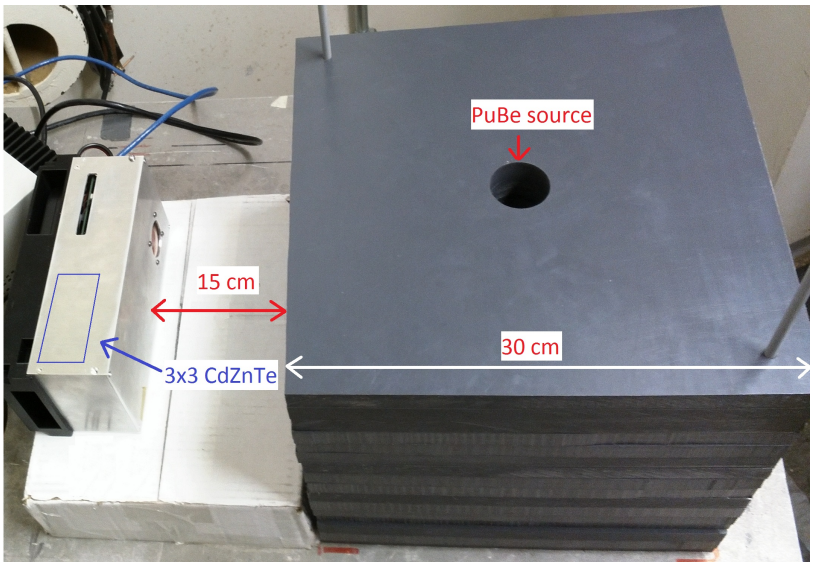

Figure 6.1: Setup of the Orion system and PVC target in one experiment. Location of the detector array is highlighted.

The measured data was initially processed by the algorithms described in Chapter II (referred to as "conevntional" reconstruction methods hereafter). Figure 6.2 presents the reconstructed spectra from a 4-hour measurement. The system used over 1 MeV threshold in the measurement to avoid triggering on low-energy gamma rays. The waveforms were processed using trapezoidal filter. The non-linearity cor-

rection was not carried out. Two groups of peaks are highlighted using dark blue and red arrows. The three Doppler-broadened peaks, highlighted using dark blue arrows, are full-energy deposition, pair-production single-escape (SE) and pair-production double-escape (DE) events of 4.4 MeV gamma rays from the de-excitation of ^{12}C atoms. The other four peaks highlighted by red arrows are all pair-production, double-escape events of gamma rays from ^{35}Cl (n, γ) ^{36}Cl reactions. This represents the first time, high-energy gamma-ray peaks up to over 7 MeV were observed in 3-D CdZnTe detectors.

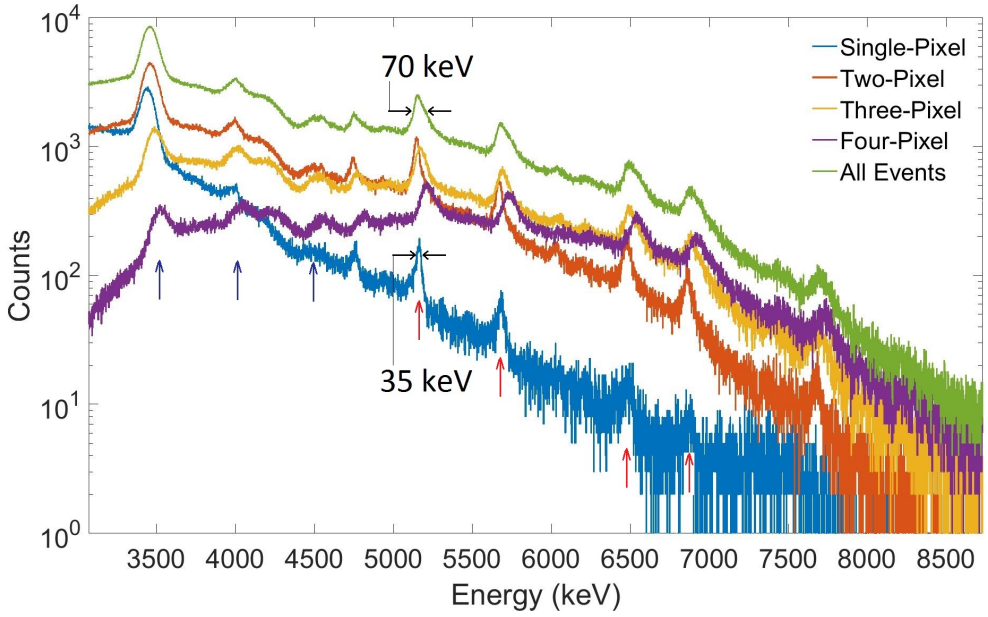

Figure 6.2: Energy spectra reconstructed using trapezoidal filter and conventional reconstructions. The resolution FWHM for the 5089 keV peaks is also shown.

Several issues in Figure 6.2 should be pointed out. First, at energies above 4.5 MeV, only the peaks from pair-production, double-escape events were observed. This indicates that the detector system's efficiency is low. As Figure 6.3 presents, gamma-ray interaction cross sections in CdZnTe decrease to about 1E-2 cm^2/g in the high-energy range, and the majority of the interactions are pair production interactions. However, this still does not fully explain the absence of full-energy photopeaks in the

high-energy range. This unexplained low efficiency in 3-D CdZnTe detector is under active investigation. In this chapter, the discussion mainly focuses on pair production, double-escape events reconstruction. Second, substantial non-linearity in the system was observed. The 5089 keV single-pixel events peak is centered at 5170 keV. In other words, the differential non-linearity is about 80 keV at 5.1 MeV in VAD_UM v2.2 ASICs. Last but not least, high-energy events were reconstructed with very poor energy resolution. For example, the 5089 keV single-pixel events, from 6111 keV DE interactions, showed only 35 keV FWHM resolution. In contrast, assuming that Fano factor is 0.1 and 5 eV is needed to create one electron-hole pair in CdZnTe [25], the theoretical resolution at 5.1 MeV only considering electronic noise (3 keV FWHM equivalent) and statistical variation is about 5 keV FWHM.

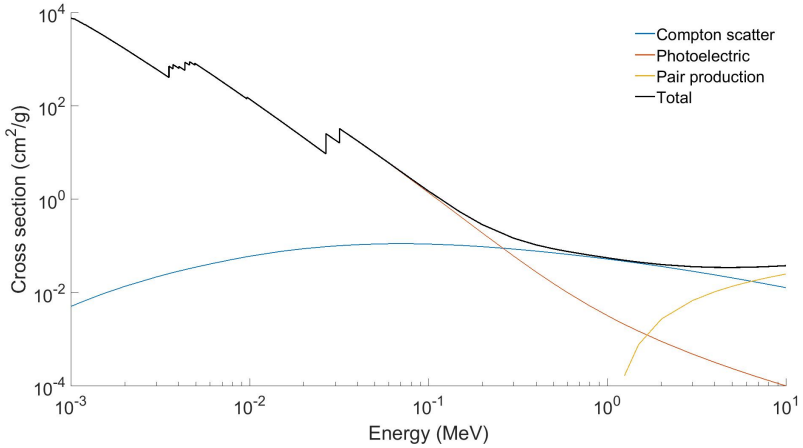

Figure 6.3: Gamma ray cross section in CdZnTe in 0 - 10 MeV.

6.3 High-Energy Events Reconstruction

This section discusses the mechanisms that degrade the high-energy events energy resolution. Correction algorithms are presented. By default, simple-subtraction is used for waveform processing prior to the reconstructions because it not only had the best performance but also had fast processing speed. The events energy reconstruction results using trapezoidal filters and SRF fitting will be discussed in Section 6.6.

6.3.1 Waveform Processing for High-Energy Events

Simple-subtraction calculates the average amplitude in a tail and baseline window, then uses the difference between the two values to estimate the signal amplitude. A drawback of simple-subtraction is that it does not align the sampling windows on an event-by-event basis with the measured waveforms. For high-energy events, this can potentially cause significant, systematic errors in amplitude estimation. By default, the baseline and tail windows in simple-subtraction are the 3-rd to the 61-th sampling cell, and the 120-th to the 158-th sampling cell, respectively. Figure 6.4 and 6.5 present the average two-pixel waveforms detected in the high-energy range for different interaction positions using one of the detectors. It could be seen that due to the weighting potential profile, cathode-side events anode waveforms increase at an earlier time compared to anode-side events. Similarly, edge and corner-pixel events anode waveforms also increase earlier than those from center pixels. These increasing edges start earlier than the 61-th sampling cell. When the default baseline sampling window (the 3-rd to the 61-th sampling cell) is used, the baseline amplitude will be overestimated and the signal amplitude will be underestimated. As mentioned, because of the difference in the weighting potential profile, the relative fractional underestimation varies as a function of the 3-D location of interaction. This issue is further complicated by the fact that the timing of rising edges is affected by the hardware threshold of the ASIC. At lower energies such as 662 keV, this issue is insignificant compared to electronic noise and statistical fluctuation of charge carriers. At 5.1 MeV, however, this variation is up to tens of keV.

To mitigate the effect of anode rising edges, the baseline sampling window was reduced to the 3-rd to the 41-th sampling cells for the baseline. The tail sampling window stayed as the 120-th to the 158-th sampling cells. These values were determined by making sure no anode rising edges occurred in the sampling windows. Though the reduction of cell samples can increase the electronic noise, this increase

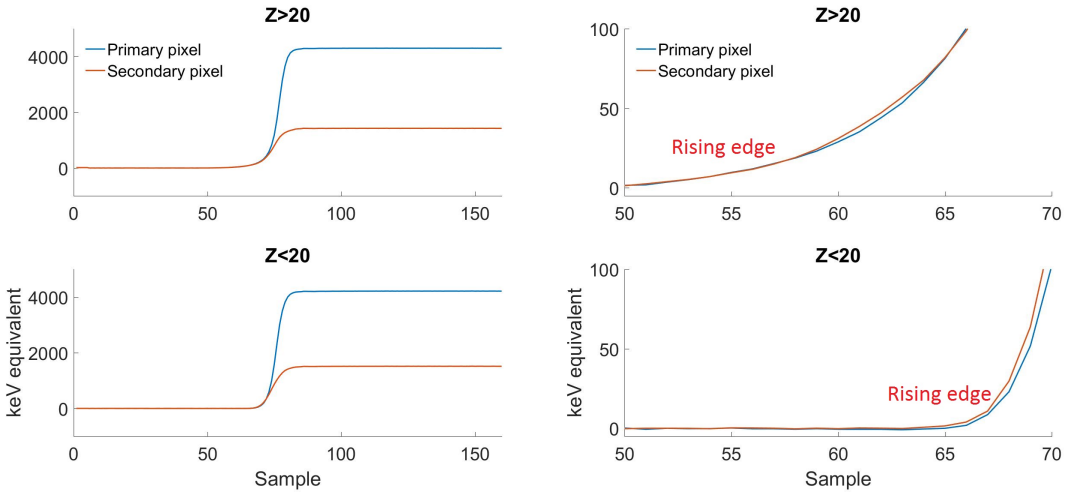

(a) Cathode-side vs. anode-side

(b) Same as left but in greater detail.

Figure 6.4: High-energy, two-pixel event average anode waveforms from the cathode side and anode side. The primary pixel is the one that has more energy deposition than the other.

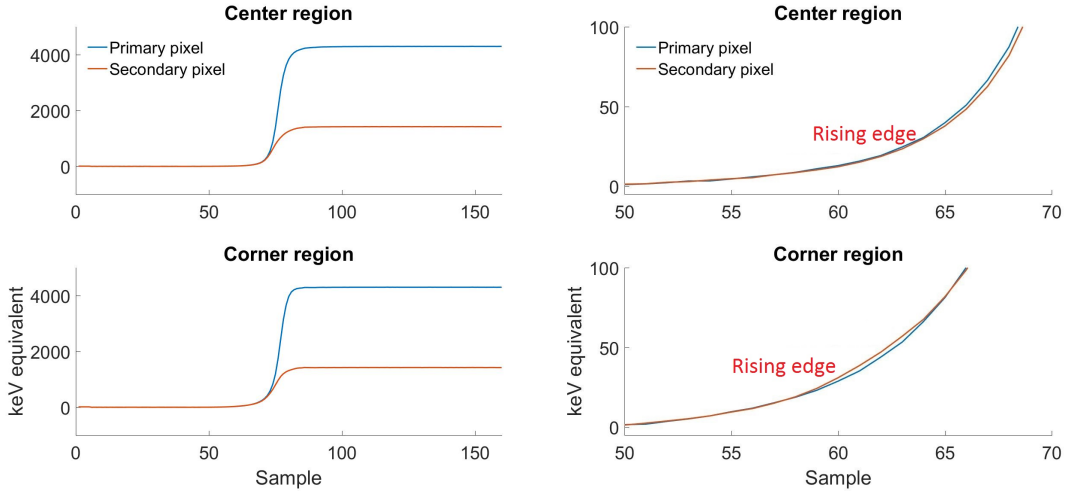

(a) Center region vs. corner region.

(b) Same as left but in greater detail.

Figure 6.5: High-energy, two-pixel event average anode waveforms from the center and corner of detector.

is negligible compared to the observed resolution in the high-energy range.

6.3.2 Neutron Damage Correction

Results in Chapter V have shown that neutron damage can cause increase of electron trapping in 3-D CdZnTe detectors. Fortunately, the locations of the detector system, PVC target and the source remained unchanged throughout each high-energy gamma ray measurement. This means that the neutron flux remained constant throughout each measurement. As a result, it is possible to model the neutron-induced extra trapping as a linear function of the progress of measurement. To verify this hypothesis, events energies, reconstructed using the conventional method, were plotted against the progress of the measurement. Figure 6.6 presents an example for a detector in a measurement using the Orion-α system. In this measurement, a very weak PuBe source was used. To accumulate enough counts, the measurement lasted 350 hours. Linear regressions were conducted between the reconstructed energy and the progress of measurement for each depth range. The slope is more negative for near-cathode events, because electron trapping is more significant for these events.

It could be observed from Figure 6.6 that linear relationships closely describe the increase of electron trapping over time. Hence, for an event with energy E, depth z in channel ch from the conventional reconstruction algorithm, an extra correction could be carried out using

$$E' = E \cdot g_{post}(ch, z)/\{g_{pre}(ch, z) + t \cdot [g_{post}(ch, z) - g_{pre}(ch, z)]\} \tag{6.1}$$

where t represents the time of detection for each event as a fraction of measurement dwell time. For two events recorded at the begining and end of the measurement, t equals to 0 and 1, respectively. $g_{pre}(ch, z)$ and $g_{post}(ch, z)$ represent the 661.7 keV event signal amplitude in channel ch at depth z, measured before and after the high-energy gamma ray experiments. It should be noted that the correction is based

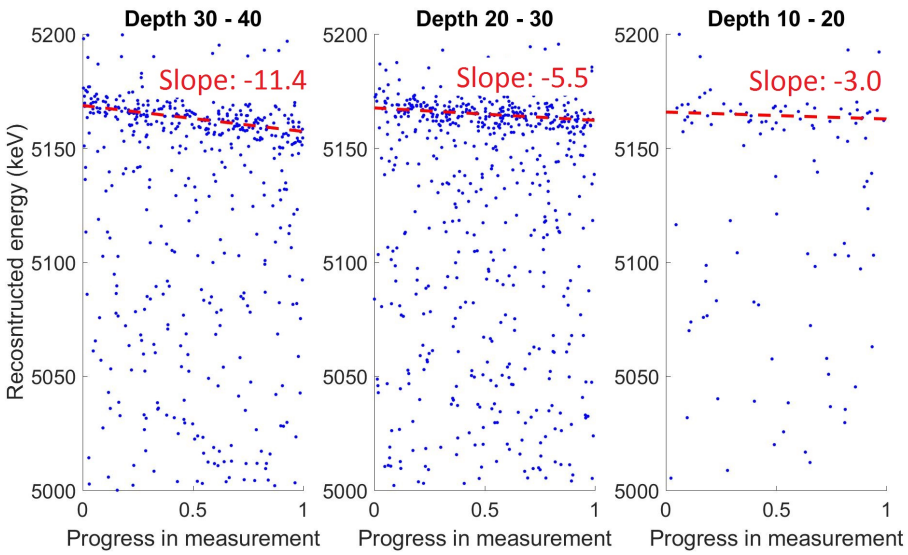

Figure 6.6: Reconstructed events energies over the progress in measurement. 0 means the beginning of measurement and 1 means the end. The events were down sampled from events in the whole detector for easier presentation. The trends stay the same when all the events were checked.

on a linear interpolation and may be imperfect. Over the 350 hours, recovery of neutron damage in CdZnTe could be observed, as shown Figure 5.5. The results of the correction for trapping change in Orion-α11 can be seen in Figure 6.7. To clearly show the improvement due to the correction of neutron-induced trapping, only non-anode-side (Z over 20), low-leak events are presented. The low-leak criterion omits events with estimated charge leak that exceed several keV. The estimation of charge leak will be discussed in Section 6.3.3.

It should be noted that the correction of neutron-induced trapping would vary in each measurement, because the neutron flux is measurement dependent. In following sections, changes in trapping were corrected using Equation 6.1 unless clarified otherwise. The following analyses and discussions focused on a 350-hour measurement using the Orion-α system. This measurement recorded the largest dataset with the minimum neutron damage in the detectors.

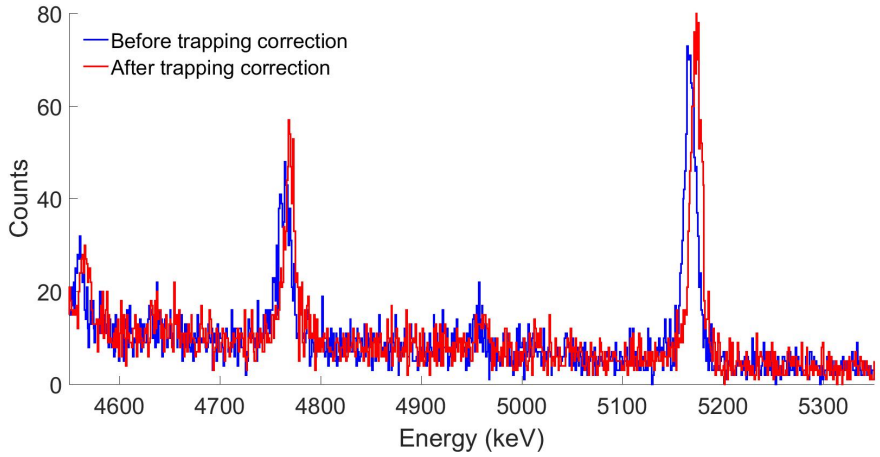

Figure 6.7: The correction of trapping change helps improve the cathode-side peak height in low-leak events.

6.3.3 Charge Leak Correction

Energetic electrons from photon interactions deposit their energies in non-infinitesimal volumes. This means charge clouds, instead of points of charge are generated from radiation interactions. In addition, repulsion and diffusion of charge further increase the sizes of clouds as they drift towards the collecting electrodes [59]. In previous studies, GEANT4 [60] simulations were used to generate energy depositions from gamma-ray interactions in CdZnTe [18, 27]. These depositions of energies were converted to charge directly, neglecting diffusion and repulsion. The simulations suggest that at high-energy ranges, the size of the electron clouds can be several mm. When an electron cloud is generated over more than one anode pixels' region, charge sharing is expected to take place [61, 62]. This is seen in Figure 6.2 where most of the 5.1 MeV events measured in 3-D CdZnTe detectors were two/three/four-pixel events. Since 5.1 MeV events correspond to pair-production, double-escape interactions from 6.1 MeV gamma rays, these events can only originate from single interactions. They were "promoted" to multi-pixel events because of charge sharing.

Charge leak originates from charge sharing events in 3-D CdZnTe detectors. In a charge sharing event, when only a very small amount of charge is collected by

one of the anode pixels, the induced signal might not be large enough to trigger the channel. In triggered only readout mode, this anode will not be read out and information corresponding to this deposited energy is lost. In high-energy gamma ray measurements, this issue was more significant due to the aggressive 1 MeV low-energy threshold used. To avoid losing information due to charge leak, triggered + 8 mode was used in these measurements and charge leak correction algorithm [18] was applied. In this section, the charge leak correction algorithm will be discussed separately for two cases: single-pixel and multi-pixel events.

Charge leak correction is a well-established algorithm for gamma rays below 3 MeV in 3-D CdZnTe detectors [18]. For each event, as charge drifts toward the collecting pixel, transient signals are induced on the neighbor pixels. Although the shape of the transient signal is expected to vary by factors such as charge distribution, electric field and trapping/de-trapping, the mean values in the tail and baseline regions in each transient signal should only be affected by weighting potential profile and charge leak. Assuming that the weighting potential field changes insignificantly as a function of the X- and Y-position for the same depth, the difference between the tail and baseline amplitudes should be the same for all the eight neighbors. To verify this hypothesis, average transient signals in SN and DN pixels were measured for 661.7 keV photoelectric events. As Figure 6.8 presents, at depth bin 20 (center of detector), the transient signals vary significantly as a function of sub-pixel locations. However, the tail amplitudes are nearly identical, regardless of the sub-pixel location of the interactions.

The single-pixel charge leak correction algorithm's pseudocode is presented in Algorithm 1. The vector vec_{diff} is one-indexed. It saves the difference between the tail and baseline values in each transient signal. The parameters $tails$ and $baselines$ are vectors storing the tail and baseline values in all the transient signals, and each vector's length is N. An implicit assumption is that at most one neighbor pixel has

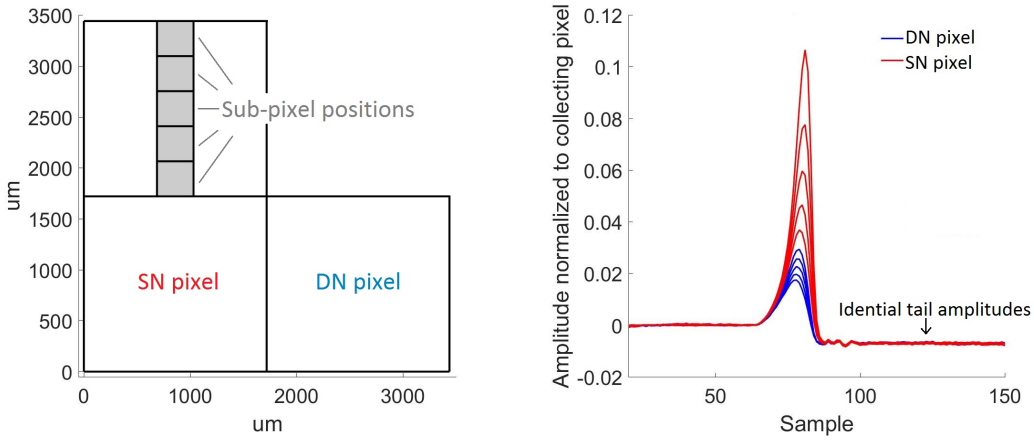

(a) Sub-pixel positions.

(b) Measured transient signals.

Figure 6.8: Measured average transient signals in side-neighbor and diagonal-neighbor pixels from 661.7 keV, single-pixel events for different sub-pixel locations at depth bin 20.

Algorithm 1 1-P charge leak correction

procedure LEAKCORR($tails$, $baselines$, N, E) ▷ input: transient signals
  init vec_{diff}
  for $k \leftarrow 1$ to N **do** ▷ N: number of transient signals
    $val \leftarrow tails[k]$ - $baselines[k]$
    push val **to** vec_{diff}
  sort vec_{diff} ▷ Sort in ascending order
  $leak_{est} \leftarrow vec_{diff}[N]$ - **mean**$(vec_{diff}[1 : N-1])$
  if $leak_{est} > thr$ **then**
    $E+ = leak_{est} \cdot 661.7/AC$

leaked charge. This assumption will be discussed later. With this assumption, charge leak should only take place in the pixel with the highest tail-baseline difference. The tail-baseline difference from the other transient signals are averaged to mitigate the effect of electronic noise. This mean value is subtracted from the last pixel's tail-baseline difference as an estimation of charge leak in ADC unit. The value *thr* is a threshold that determines when the estimated charge leak should be added to the reconstructed energy E. The value of AC is the measured ^{137}Cs single-pixel events anode spectrum cutoff, similar to that in Equation 2.8. Though a more accurate conversion could be done using the gain-depth curves, this conversion using AC is sufficiently accurate. It could be seen from Figure 2.21 that the gain-depth value changes by only several percent in non-anode-side regions. Consider an extreme example when the true energy leak is about 50 keV, the absolute error of estimated charge leak due to this conversion is still lower than contributions from electronic noise.

The optimal *thr* value in Algorithm 1 is a balance between two competing factors. A high *thr* value makes charge leak correction ineffective. A low *thr* value is more likely to result into over-correction because some non-charge-leak events can be incorrectly identified.

Similar to single-pixel event charge leak correction, Algorithm 2 presents the charge leak correction algorithm for multi-pixel events. It also assumes that at most one neighbor pixel has leaked charge. Although Algorithm 2 seems identical to Algorithm 1, it should be carried out on a "cluster-by-cluster" basis. A "cluster" of pixels is the group of triggered anode pixels that are adjacent to each other. For example, in Figure 6.9, transient signals from the seven neighbor pixels will be used as the input. An extra challenge in multi-pixel events charge leak correction is that the induced net signal amplitude in each neighbor pixel can come from electrons in more than one collecting anodes. This induction is very difficult to model accurately.

Algorithm 2 Multi-Pixel charge leak correction

```
1: procedure LeakCorr(tails, baselines, N, E)        ▷ input: transient signals
2:     init vec_diff
3:     for k ← 1 to N do                              ▷ N: number of transient signals
4:         val ← tails[k] - baselines[k]
5:         push val to vec_diff
6:     sort vec_diff                                  ▷ Sort in ascending order
7:     leak_est ← vec_diff[N] - mean(vec_diff[1 : N − 1])
8:     if leak_est > thr then
9:         E+ = leak_est · 661.7/AC
```

To apply the charge leak correction algorithms to high-enegry events correction, two questions must be answered. First, because the electron cloud size is larger at higher energies, is the assumption that at most one neighbor pixel has leaked charge still valid? Second, the absolute variation of tail-baseline difference as a function of the X- and Y-location will be amplified in the high-enegry range. Will this increase the inaccuracy of the estimated charge leak? These two questions are answered separately in the discussions below.

To verify the assumption that at most one neighbor pixel has leaked charge, GEANT4 was used to simulate 6.1 MeV gamma-ray pair-production interactions in CdZnTe where simulated electron clouds were recorded. This simulation assumes (1) the initial electron-hole pair positions can be approximated by the energy depositions directly, (2) no repulsion or diffusion take place and (3) the electrons drift towards the anode panel perpendicularly. An example is presented in Figure 6.9, where a simulated electron cloud is overlapped with virtual gaps between the anode pixels. In this example, if one uses 1 MeV hardware threshold and 30 keV software threshold, one anode pixel will be hardware triggered and eight neighbor pixels are read out. One of the neighbor pixels will be software triggered and the event becomes a two-pixel event.

The simulation was repeated using different software thresholds that was as high as 500 keV. The high software threshold was used to imitate events near the an-

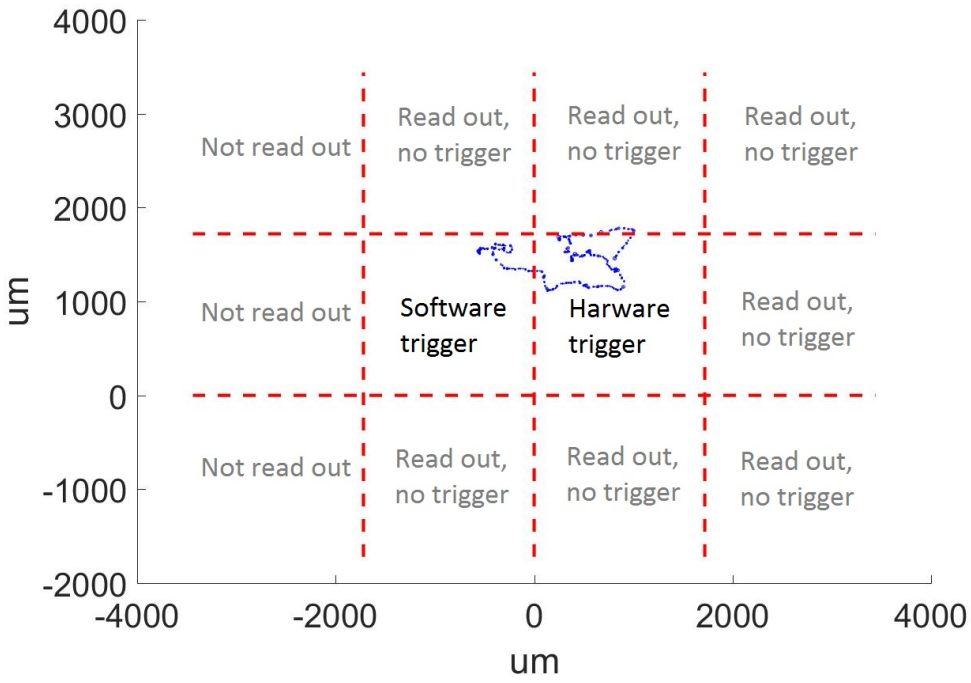

Figure 6.9: Simulated electron cloud in blue dots. The red dashed lines represent the gap between the pixels.

ode region. As discussed above, these events can cause non-negligible negative net signal amplitudes in non-collecting pixels. Even though the DAQ used a software threshold of about 30 keV, this induced negative signal makes the effective software threshold as high as several hundred keV for 5.1 MeV interactions. To verify that the simulated model is correct, the numbers of triggered pixels (both hardware- and software-triggered) were recorded for each event type and the probabilities were compared with measured results at 5.1 MeV. The measurement result for event type probability falls into the range predicted by the simulations, indicating that the simulation model was reasonably correct. It should be noted that in the measurement, only 1/2/3/4-pixel events were recorded. However, both the simulations and measurements showed that the most likely event types are two- and three-pixel events, and the simulations showed that events with more than 4 pixels triggered only occur with less than 5% probability.

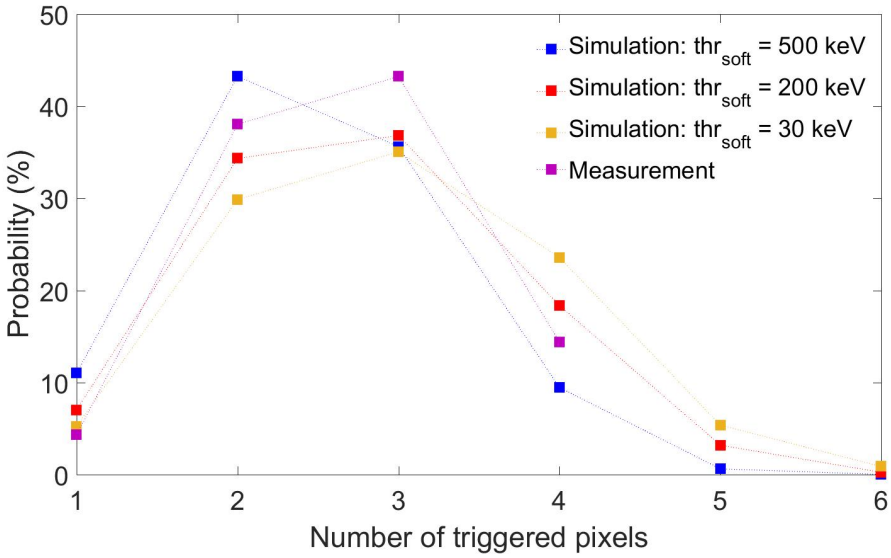

Figure 6.10: Simulated probability of event types compared with measurement results. Higher software thresholds in the simulations correspond to events closer to the anode side. The uncertainty was below 1% and error bars are not shown.

Three types of samples are recorded in each simulation presented in Figure 6.9:

1. The total energy in pixels that are hardware- or software-triggered, E_{trig}.
2. The total energy in pixels that are read out using trigger + 8 mode, $E_{readout}$.
3. A vector that records the energy depositions in all neighbor pixels that are not software-triggered, $Evec_{nb}$.

In each simulation, $Evec_{nb}$ was sorted in descending order. If the assumption that at most one neighbor pixel has charge leak is true, one should expect that the difference between $E_{readout}$ and E_{trig} closely matches the first element in $Evec_{nb}$. Figure 6.11 presents the simulation data using 1 MeV hardware threshold and 500 keV software threshold. As mentioned above, the high software threshold was used to simulate near-anode events. For these events, charge leak discrimination in the DAQ software performs poorly. Still, about 90% of the data points fall into the $y = x$ trend line. In the other 10% events, more than one neighbor pixels can have leaked charge. The

simulation result suggests that assuming at most one neighbor pixel can have leaked charge is reasonable.

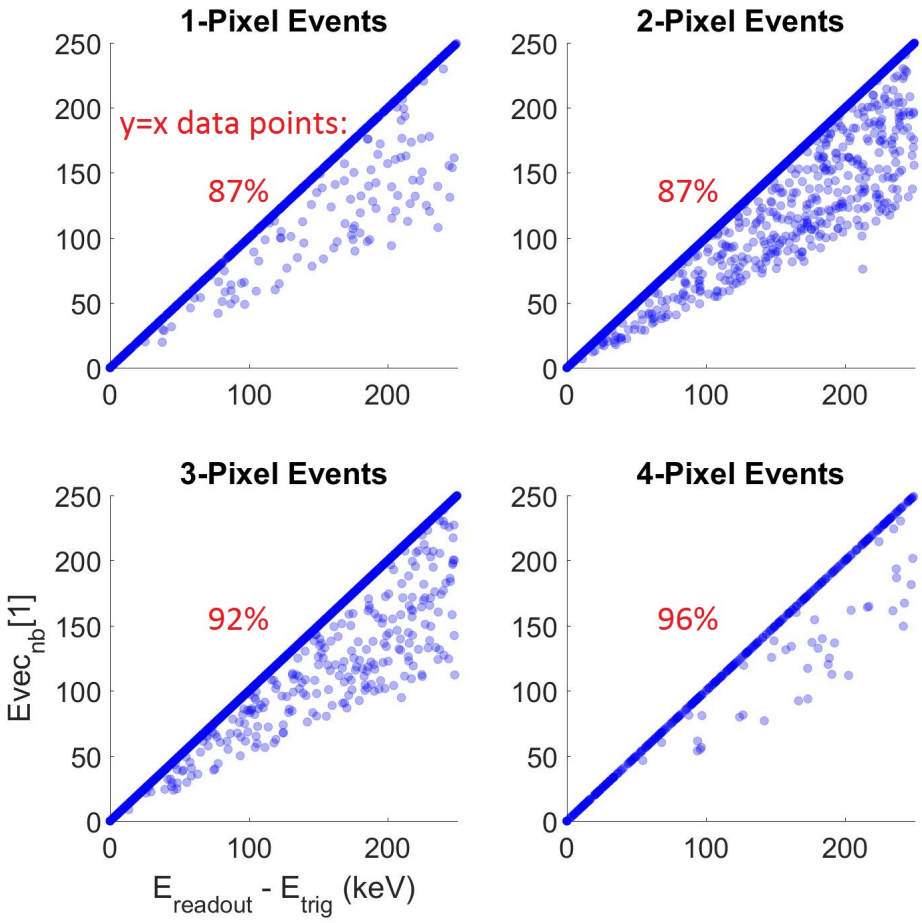

Figure 6.11: Simulation results: total leaked charge to neighbor pixels, compared with charge leaked to the most significant neighbor pixel. 500 keV software threshold and 1 MeV hardware threshold were used.

For further validation using experimental data, the sorted vec_{diff} values in charge leak correction were recorded. Figure 6.12 presents example histograms of the tail-baseline differences from the first three neighbor pixels of single-pixel events at depth bin 35 after sorting. It could be seen that the histogram for the first neighbor's tail-baseline difference values shows a significant "plateau" in the range of [10, 45] ADC, while the other two neighbor pixels' histograms are almost identical and do

not have such a plateau. The comparisons experimentally verify that in most cases, at most one neighbor pixel has leaked charge. This conclusion is consistent with the observation in Figure 6.17, that the correction eliminated the low-energy tail very well.

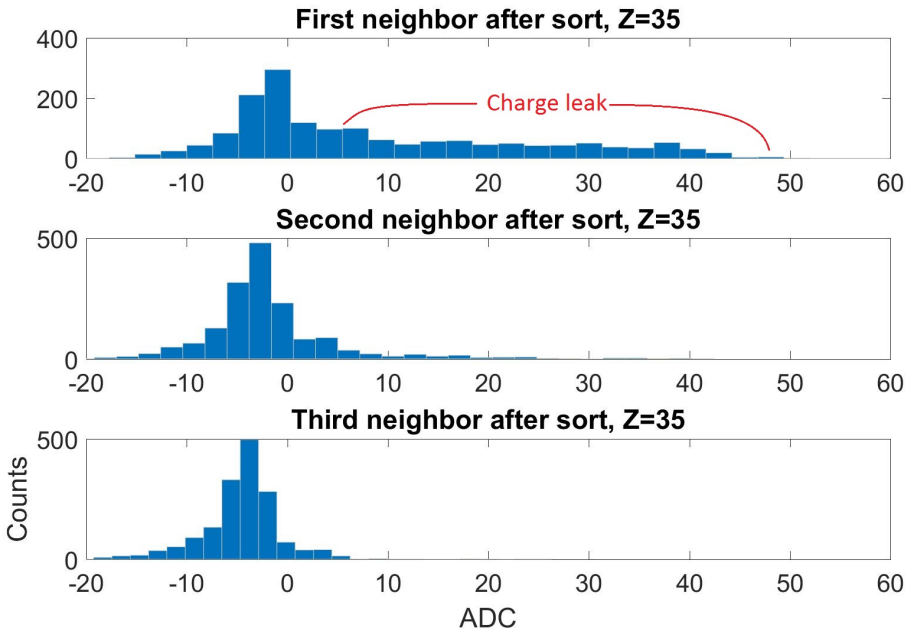

Figure 6.12: Histograms of tail-baseline differences from the first three neighbor pixels of single-pixel events at depth bin 35 after sorting. Note the mode in each histogram was below zero because of WPCT.

In the high-energy range, the tail-baseline difference, assuming zero leaked charge, can still vary by a non-negligible amount as a function of the X- and Y-location of the electron cloud. To demonstrate this two derived values were calculated and compared: the "diagonal-neighbor amplitude difference" (DNAD) and "diagonal-neighbor tail difference" (DNTD). Figure 6.13 presents the waveforms from the triggered anode, cathode and the neighbor pixels in a high-energy, single-pixel event. The figure also includes the tail-baseline difference for all the eight neighbor pixels. It could be seen that neighbor 7 has a tail-difference value of 16.83 ADC, significantly higher than the other neighbor pixels.

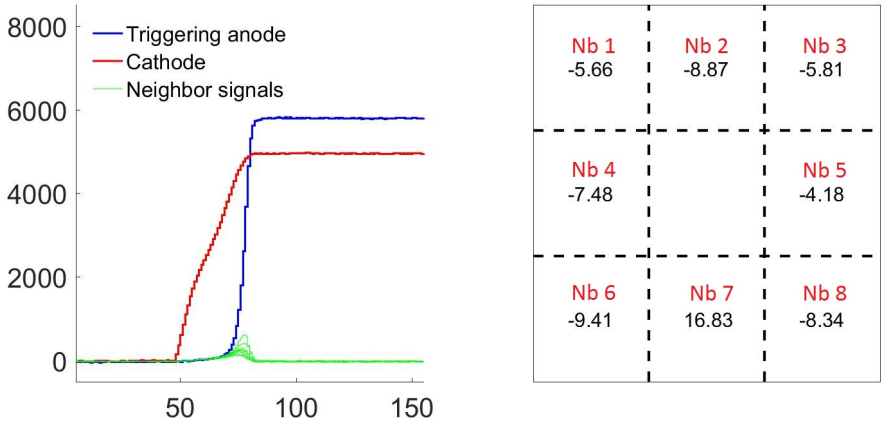

Figure 6.13: Example high-energy, single-pixel event waveforms and tail-baseline difference in each neighbor pixel.

For each single-pixel event, DNAD and DNTD are calculated along two orthogonal directions: top-bottom and left-right. The calculation for each value is done by

$$DNAD_{LR} = A_1 + A_6 - A_3 - A_8 \tag{6.2}$$

$$DNAD_{TB} = A_1 + A_3 - A_6 - A_8 \tag{6.3}$$

$$DNTD_{LR} = T_1 + T_6 - T_3 - T_8 \tag{6.4}$$

$$DNTD_{TB} = T_1 + T_3 - T_6 - T_8 \tag{6.5}$$

where A_i and T_i represent the signal amplitude and the tail-baseline difference in the i-th neighbor pixel respectively. The calculation of A_i is the same as the sub-pixel position calculation method introduced in Section 2.2.4. The indexing of i is shown in the right plot of Figure 6.13. Information from only the DN pixels was used to mitigate effect of charge leak.

Similar to that in Equation 2.6 and Equation 2.7, the value of $DNAD$ encodes information about the sub-pixel location of the electron cloud. For example, a positive $DNAD_{LR}$ value indicates that most of the charge in the electron cloud should be closer to the left region of the collecting anode pixel. The values of $DNTD$ could

be compared against $DNAD$. If the sub-pixel location of the electron cloud does not affect the tail-baseline difference, no statistical relationship should be observed between $DNAD$ and $DNTD$. Figure 6.14 and Figure 6.15 present the relationship between $DNAD$ and $DNTD$ along the two directions.

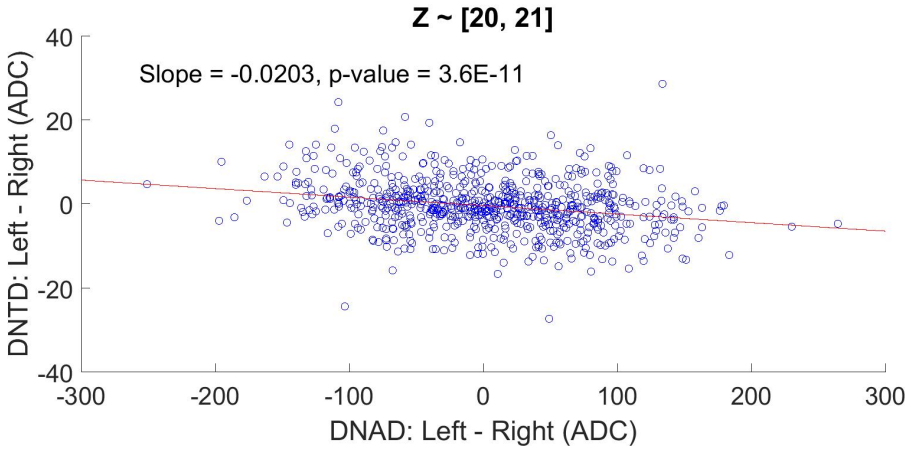

Figure 6.14: $DNTD_{LR}$ vs. $DNAD_{LR}$ for high-energy, 5089 keV events at depth bin 20. The red line represents the linear regression. Regressed slope and p-value are shown in text.

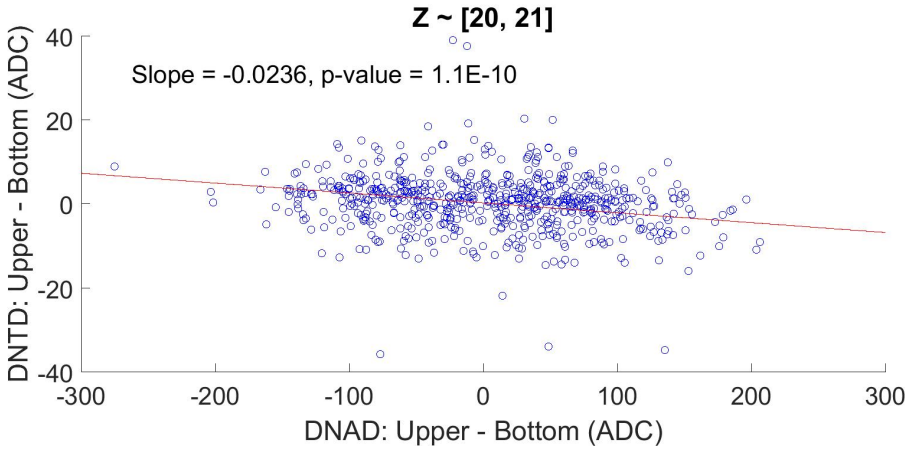

Figure 6.15: $DNTD_{TB}$ vs. $DNAD_{TB}$ for high-energy, 5089 keV events at depth bin 20. The red line represents the linear regression. Regressed slope and p-value are shown in text.

It could be seen that at depth bin 20, on average a lower $DNTD$ value is expected for a lower $DNAD$ value. The p-values for the regressed slopes based on t-test [63] are very close to zero, indicating that the negative slopes are statistically true. Physically,

the negative slope means that the tail-baseline difference in a neighbor pixel without leaked charge is expected to be lower if the electron cloud is closer to this neighbor pixel. The slope values of roughly -0.02 in Figure 6.14 and Figure 6.15 also indicate that for a single-pixel event at depth bin 20, the sub-pixel position in the X- and Y-location causes at least 6 ADC (equivalent to about 6 keV) variation of the tail-baseline difference. This variation is a lower bound based on the linear regression because the independent variable in this regression, $DNAD$, is not guaranteed to fully represent the sub-pixel location variation. For instance, the electron should have an extended shape on sub-pixel levels, however this distribution is not measured by $DNAD$.

Table 6.2 presents the regressed slopes between $DNAD_{TB}$ and $DNTD_{TB}$ for high-energy, single-pixel events in each depth bin. It could be seen that for depths closer to the anode side, more negative slopes are observed. This is expected because WPCT variation is expected to be more significant in regions closer to the anode side.

Table 6.2: Regressed slopes between $DNAD_{TB}$ and $DNTD_{TB}$ for high-energy, single-pixel events in each depth bin. A p-value smaller than 0.05 is considered significant statistically.

Depth bin	Slope	p-value
15	-0.0832	1.8E-32
20	-0.0236	1.1E-10
25	-0.0150	5.9E-7
30	-0.0090	2.3E-5

Table 6.2 also implies that the optimal thr value in the charge leak correction algorithms should be a function of the depth of interaction. For events closer to the anode, thr should be set higher. Figure 6.16 compares the reconstructed energy E before charge leak correction, and the estimated charge leak $leak_{est}$ for single-pixel events reconstructed to different depth ranges in one of the detectors.

Three observations in Figure 6.16 should be emphasized. First, a dashed red

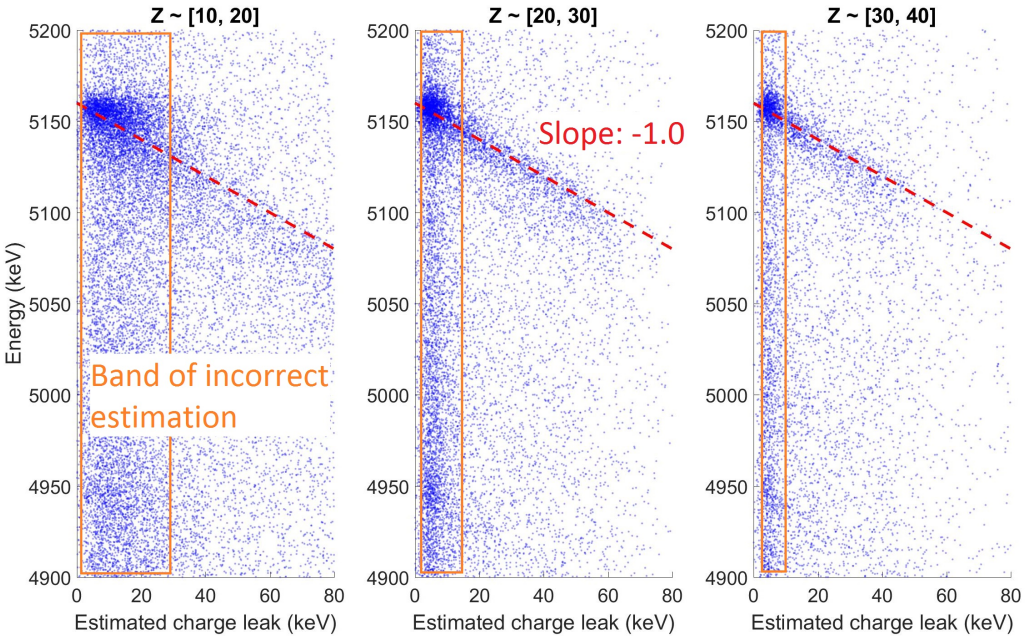

Figure 6.16: Reconstructed energy compared against the estimated charge leak for single-pixel events in different depth regions.

line with -1.0 slope is added to each figure. The lines closely match the relationship between the estimated charge leak and the reconstructed energy. This means that the corrections in Algorithm 1 is unbiased. Second, an orange box is added in each figure that highlights a region of incorrect charge leak. The region is wider for near-anode events, because of the increase in the variation of net signal amplitudes, as presented in Table 6.2. Third, for events with depths closer to the cathode (depth bins 30-40), most of the estimated charge leaks are distributed below 60 keV. In contrast, the estimated charge leak for events closer to the anode side can range to over 80 keV. This is due to the triggering mechanism in the detector system. With the waveforms collected, the data acquisition (DAQ) software will take the difference between the tail and baseline amplitudes in each neighbor waveform. Any waveform with a difference larger than a software trigger threshold will be recognized as an additional triggering pixel. Hence, a single-pixel event with too much leaked charge can be promoted to a two -pixel event. For near-anode events, a negative net signal

is induced on the neighbor pixels. As a result, this simple discrimination method using a soft threshold is less effective for near-anode interactions. In subsequent discussions, "hardware threshold" is used to represent the threshold in the ASICs, and "software threshold" is used to represent the threshold implemented in the DAQ. Understanding the triggering mechanism composed of the combined hardware and software thresholds is essential for later discussions.

Heuristically, for high-energy reconstruction, the value of *thr* can be set to 15 keV equivalent for $Z < 20$ and 5 keV equivalent for $Z >= 20$. Small adjustments (several keV) to this value does not affect the energy resolution significantly.

To verify that the charge leak correction is correctly implemented, spectra of non-anode-side events before and after the charge leak correction are compared. An example with data from Orion-α 31 is shown in Figure 6.17. The spectrum for events with estimated charge leak below 5 keV is also presented. It could be noticed that the charge leak correction algorithm eliminated the low energy tail in the uncorrected events spectrum due to charge leak, and significantly increased the peak amplitude. After charge leak correction, an energy peak at 4950 keV also became distinguishable. The energy spectrum for events with estimated leak below 5 keV showed an energy resolution of 14 keV FWHM. This is an approximation of the expected energy resolution without any leaked charge because 5 keV charge leak is negligible compared with the peak width of 14 keV. In comparison, the charge-leak-corrected spectrum showed a resolution of 16 keV FWHM. The 2-keV difference can be attributed to additional electronic noise in the neighbor pixels, and variations in WPCT as shown in Table 6.2.

6.3.4 Non-Linearity Correction

As discussed in Chapter II, energy non-linearity exists in 3-D CdZnTe detectors. In addition, the non-linearity varies on a channel-by-channel basis. As a result, both

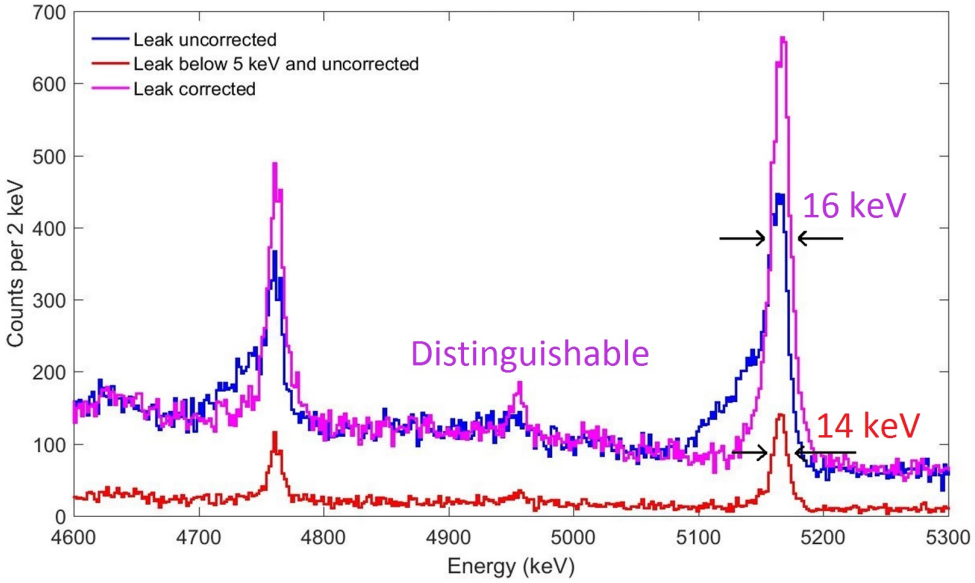

Figure 6.17: Orion-α13 single-pixel events with Z in range [20, 40].

single-pixel events and multi-pixel events resolution can be degraded if non-linearity problem is not corrected for.

For practical purposes, a non-linearity correction could only be carried out using events from the whole detector. This process was identical to that discussed by Zhang and Kaye [27,31]. Interestingly, as Figure 6.18 shows, all the detectors showed about 80 keV differential non-linearity at 5089 keV. The peak centroids were measured after charge leak correction was carried out. This consistency is not surprising because all the modules used the VAD_UM v2.2 ASICs. The observation suggests that even if there are no available sources that generate gamma rays above 3 MeV, one could simply use the 80 keV differential non-linearity value at 5089 keV, to correct for the non-linearity to a first order for all detectors connected to VAD_UM v2.2 ASICs.

In subsequent discussions, a non-linearity correction was always carried out for the whole detector, using measurements from ^{137}Cs and ^{228}Th sources, as well as the measured peak centroids for the 4.7 MeV and 5.1 MeV events in the high-energy range from ^{35}Cl gamma rays.

Figure 6.19 presents a summary of the reconstructed 5089 keV events resolution

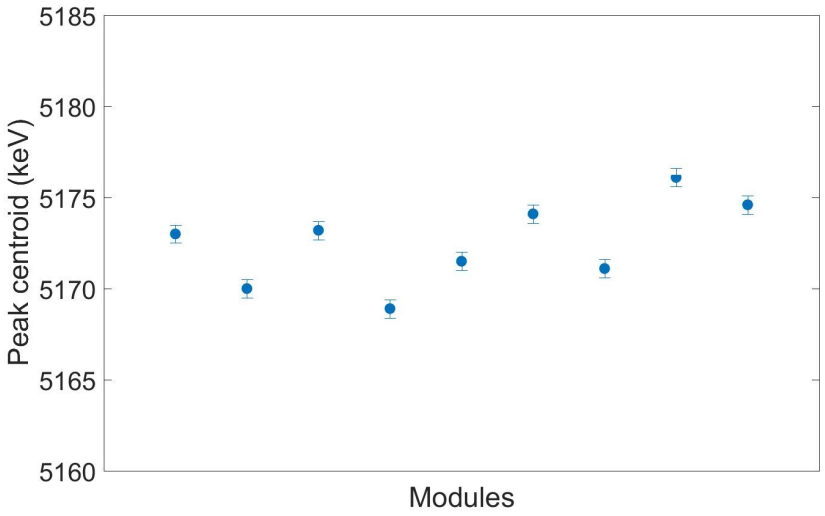

Figure 6.18: 5089 keV events peak centroid in each module of the Orion-α system.

FWHM for each event type. It could be seen that Orion-α22 showed significantly worse resolution for 3- and 4-pixel events compared to the other detectors. The specific issue on this detector is discussed in Section 6.5.2. Among the other detectors, 19, 20, 22 and 25 keV FWHM were achieved for 1-, 2-, 3- and 4-pixel events on average.

Assuming 3 keV (FWHM equivalent) electronic noise (see Figure 2.2), 5 eV (w) required on average for each electron-hole pair in CdZnTe and 0.1 Fano factor (F), the expected single-pixel events resolution at 5.1 MeV is about 5 keV using root summed square [25]:

$$FWHM_{total} = \sqrt{2.35^2 wFE + FWHM_e{}^2}. \tag{6.6}$$

The reported results in Figure 6.19 are still quite poor compared with the theoretical expectation. In the following section, the effects degrading the high-energy events resolution in 3-D CdZnTe detectors are discussed.

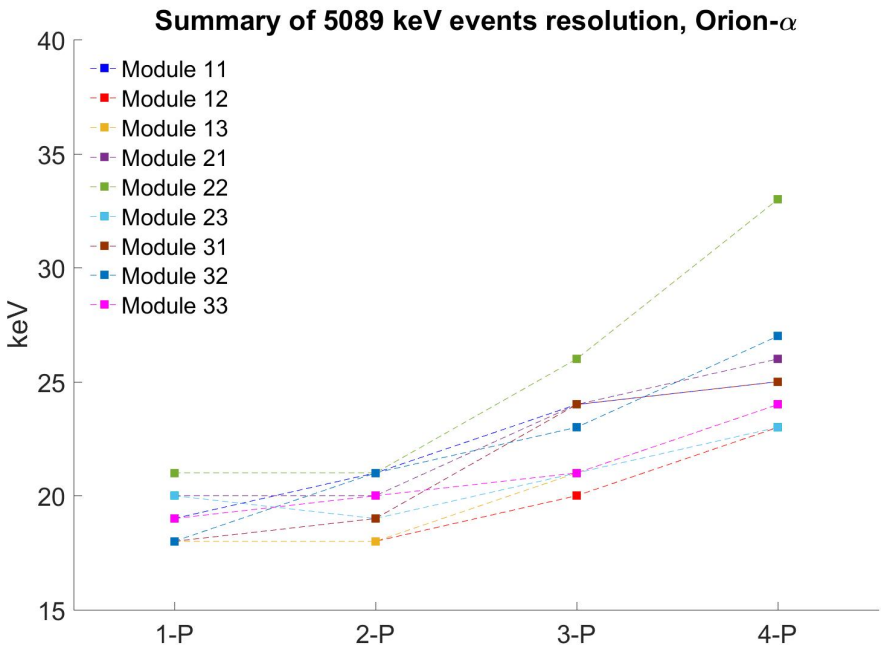

Figure 6.19: 5089 keV events resolution for each event type. The FWHM values were rounded to integers.

6.4 Single-Pixel Events Results and Analyses

6.4.1 Decomposition of Degradation Mechanisms

Single-pixel events can be "decomposed" using various filters and correction methods to evaluate the peak width contribution from each factor. The aggregated results from all the nine detectors are shown in Figure 6.20 and 6.21. Figure 6.21 also includes the theoretical value based on Equation 6.6. It could be noticed that Figure 6.21 presents the results as the squared FWHM values in each step. This quantification assumes that the peak width contribution from each factor can be regarded as an independent noise component. It could also be noticed that the largest gains in detector resolution were caused by steps "Z>20" and "Peak align". The physical meaning of each step will be discussed in the following sub-sections.

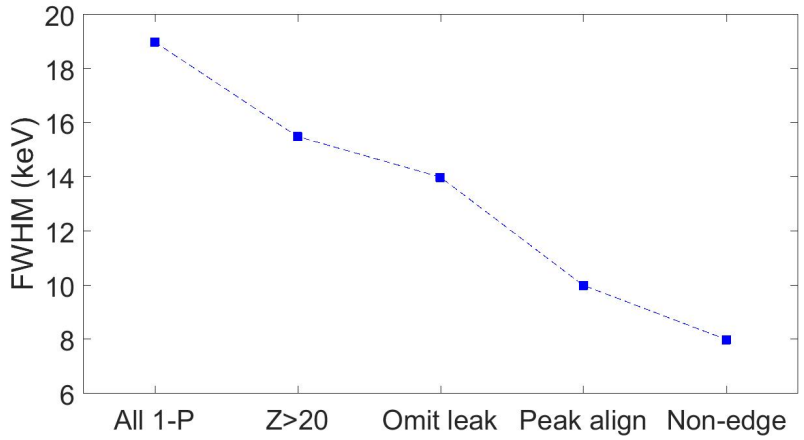

Figure 6.20: 5089 keV, single-pixel event energy resolution FWHM, after each additional filtering and correction step.

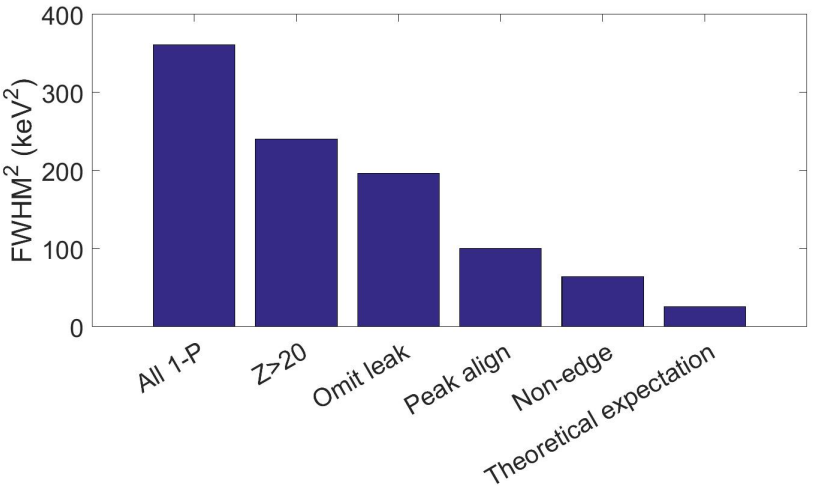

Figure 6.21: 5089 keV, single-pixel event energy resolution FWHM, quantified as squared values, after each additional filtering and correction step.

6.4.2 Anode-Side Events Performance

In the whole detector a 19 keV FWHM was achieved. This required a calibration at 662 keV, correction for neutron damage, and a charge leak correction.

In the second step, when only cathode-side (Z>20) events were selected, the resolution improved to 16 keV. This improvement comes from the omission of low-quality anode-side events with poor energy resolution. In 3-D CdZnTe detectors, the weighting potential for collecting anode changes drastically in the near-anode region. This could be verified in part using a simulation based on GEANT4 [60] and Maxwell [16].

In the simulation, GEANT4 was used to generate energy depositions from pair-production, double-escape events of 6.1 MeV gamma rays. These depositions were rcorded as the electron cloud, with subsequent diffusion and repulsion neglected. An example is shown in Figure 6.22.

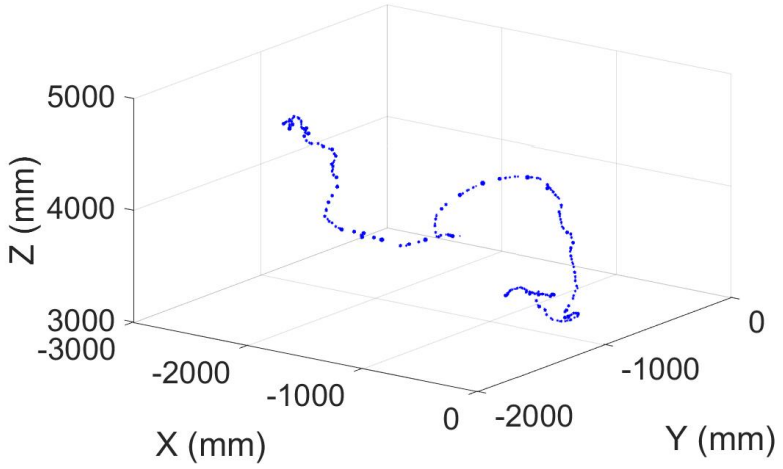

Figure 6.22: An example electrons cloud from GEANT4 simulation.

Assuming that the electric field in the detector is uniform, the electron clouds will drift towards the anode side at a constant speed. Electron clouds corresponding to single-pixel events were discriminated by projecting each electron cloud onto the X- and Y-plane and making sure all the charge is collected by only one pixel.

Using Maxwell, the weighting potential for each electrode in a 3-D CdZnTe de-

tector could be calculated. For each simulated single-pixel electron cloud, neglecting the effect of trapping, the expected amplitudes of signals induced on the anode and cathode could be calculated using the dot product between the cloud and the weighting potential in the 3-D space. For each event, the estimated depth of interaction is calculated by CAR

$$Z_{est} = 40\frac{S_C}{S_A} \tag{6.7}$$

where S_C and S_A are the simulated cathode and anode signal amplitudes considering the effect of weighting potential. Using this estimated depth, the reconstructed energy was simulated by

$$E_{est} = \frac{S_A}{1 - WP(Z_{est})} \tag{6.8}$$

where $WP(Z)$ represents the weighting potential in the center X/Y region above the collecting pixel at depth Z. For ease of understanding, Equation 6.7 and 6.8 are the simulation counterparts of 2.8 and 2.9. The simulation was used to predict the peak centroid and FWHM for each reconstructed depth of interaction. The results are shown in Figure 6.23. It should be noted each spectrum was blurred by a 15-keV-FWHM Gaussian curve to account for other effects degrading the resolution. The value of this width was chosen based on the measured peak width for Z-over-20 events (shown in Figure 6.20). In comparison, Figure 6.24 presents the measured single-pixel, 5089 keV events in one of the detectors.

The first-order agreement between Figure 6.20 and Figure 6.24 validates the hypothesis that in the near-anode region, the resolution degradation was mainly caused by the drastic change in the weighting potential profile. Still, two observations should be noted. First, the measured FWHM degradation near the anode region was even worse than the simulated results. This was expected, because the simulation was

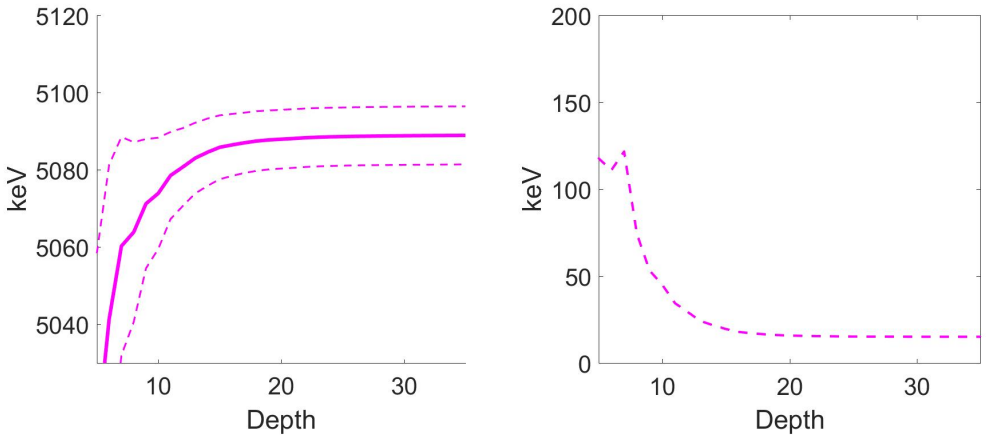

(a) Simulated peak vs. depth. (b) Simulated FWHM vs. depth.l filter

Figure 6.23: Simulated single-pixel, 5089 keV events peak information. In the left figure the solid line represents the peak centroid and the dashed lines represent the FWHM.

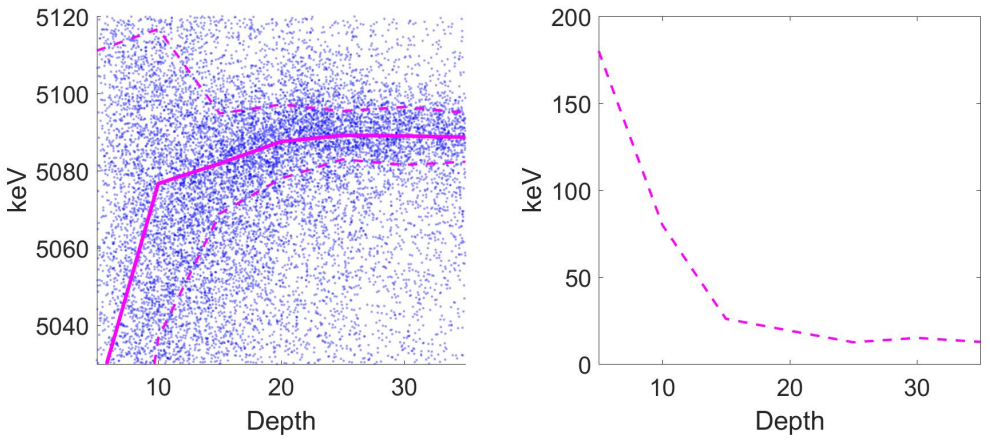

(a) Measured energy and peak vs. depth. (b) Measured FWHM vs. depth.l filter

Figure 6.24: Measured single-pixel, 5089 keV events peak information in Orion-α32. In the left figure the solid line represents the peak centroid and the dashed lines represent the FWHM. Each blue data point in the scatter plot represents one event.

still conducted using a simplified model. For example, the simulation assumes that the electric field was constant. However, in near-anode region, the electric field could change by a non-negligible extent, which further complicates the signal induction process. Second, in both the simulation and the measurement results, the reconstructed photopeak centroid decreased in the near-anode region. This trend originates from the fact that the gain-depth curves are concave downwards due to the weighting potential profile (shown in Figure 6.25). For ease of understanding, one could consider two simplified electron clouds. The first one is generated with 1 MeV equivalent charge in each depth bin 9, 10 and 11, while the second one is generated with 3 MeV equivalent charge in depth 10. Because of the concavity in Figure 6.25, less signal amplitude will be induced on the anode for the first electron cloud. In addition, because the weighting potential profile for the cathode electrode is linear (shown in Figure 1.3), when CAR is used to estimate the depths, the first cloud's depth will be over-estimated while the second cloud's depth is accurate. Based on Equation 2.9 and Equation 6.8, the energy will be further underestimated for the first cloud. The depth underestimation for near-anode electron clouds could be predicted using the simulation mentioned above. The result is presented in Figure 6.26 where Z_{true} is calculated using the energy-weighted mean depth for each electron cloud. This energy overestimation could also happen for lower-energy events, as proposed by Zhang [27]. At higher energies, this effect becomes more significant due to larger cloud sizes. It should also be noted although the systematic trend between the peak centroid and reconstructed depth was well predicted, correction for this trend could not bring about noticeable resolution improvement because the near-anode events resolution is very poor.

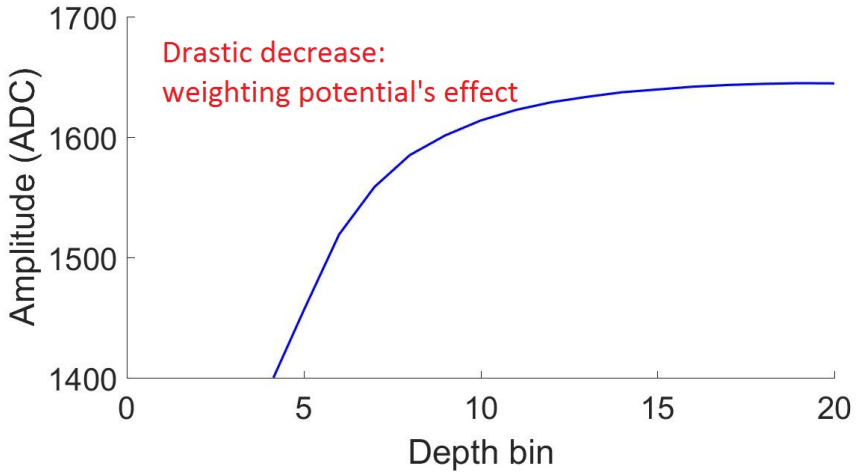

Figure 6.25: An example gain-depth curve in the near-anode region.

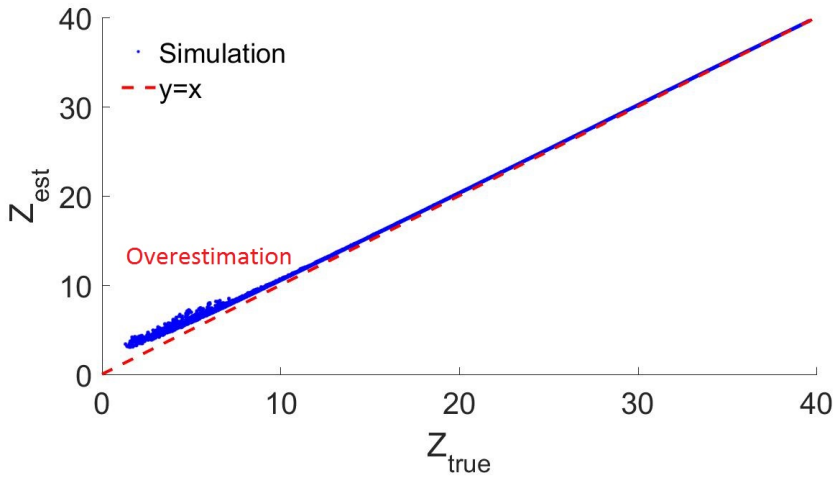

Figure 6.26: The simulation predicts overestimation of Z using CAR for 5089 keV, single-pixel events.

6.4.3 Imperfect Charge Leak Correction

In the third step of Figure 6.20, an "Omit leak" filter was used. Events with estimated charge leak larger than 4 keV were omitted. As discussed in Section 6.3.3, charge leak correction is not perfect at high energies due to variation of WPCT. As a result, events after the "Omit leak" filter showed 14 keV FWHM resolution, about 2 keV better than events before this filter (Figure 6.20). Events with estimated charge leak less than 4 keV are referred to as "no leak" events for simplicity hereafter. The threshold of 4 keV was chosen to suppress the effect of charge leak as much as possible, while make sure enough remaining events are available for further analysis.

6.4.4 Channel-by-Channel Non-Linearity

Although a channel-by-channel non-linearity correction is impractical for each detector, with the data from the long measurement of 350 hours, the gain of the system at 5089 keV can be measured and corrected on a channel-by-channel basis. This does not serve practical purposes directly, but helps improve the understanding of resolution underestimation.

Figure 6.27 presents the single-pixel events spectrum from Orion-α13, after corrections of neutron-induced trapping and charge leak. In the above 3 MeV range, the 5089 keV peak had the most single-pixel events. On average, about 130 events were recorded in the 5089 keV peak region ([5150, 5210] keV) in each channel. For gamma rays at lower energies, this amount of events under a mono-energetic peak are usually enough to estimate the peak centroid. However, in this measurement, multiple gamma rays were measured at the same time. A non-negligible background is present under the 5089 keV peak and the number of 130 counts included the background.

The precision of the measured 5089 keV peak centroid in each channel with about 130 counts under the peak must be verified. This precision could be estimated by bootstrapping [64]. The measured single-pixel events spectrum, as Figure 6.27 shows,

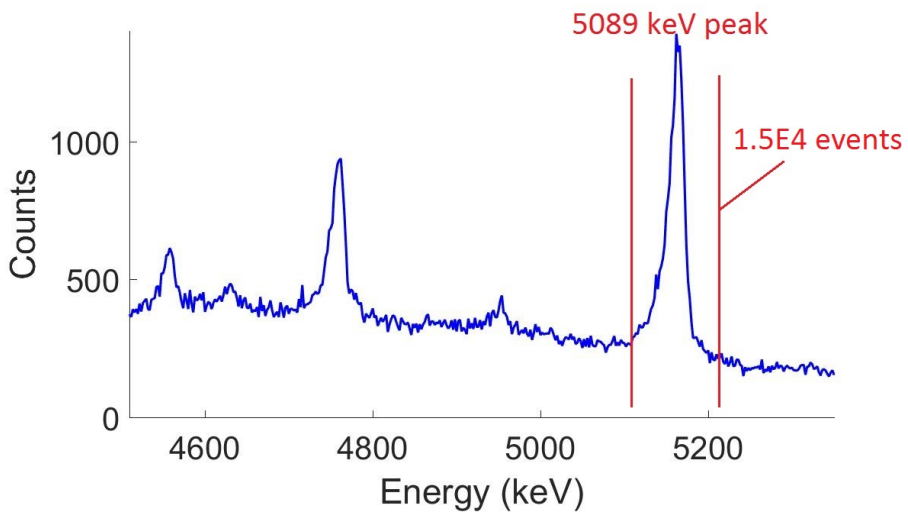

Figure 6.27: Single-pixel events spectrum in Orion-α13 from the 350-hour measurement, after correction for neutron-induced trapping and charge leak. About 1.5E4 events were recorded in the highlighted region without background subtraction.

was used as the approximated probability density function (PDF) of single-pixel events for each channel. Repeated simulations were conducted by randomly sampling from this PDF until 130 counts were accumulated in the 5089 keV peak region. The 5089 keV peak centroid was measured in each simulation by taking the average of all the samples that fall into the [5150, 5210] keV region. As Figure 6.28 presents, the repeated simulations showed 2 keV FWHM in the estimated photopeak centroids. This precision is sufficient for channel-by-channel gain correction.

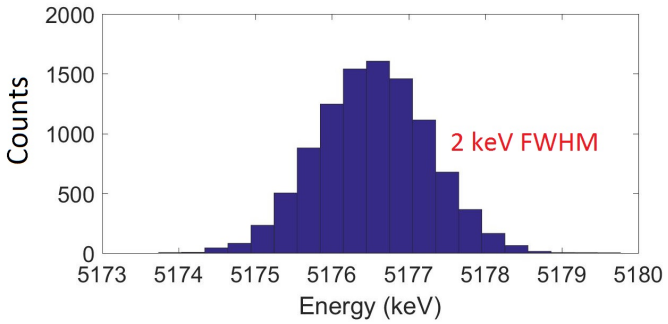

Figure 6.28: The boostrapping results showed 2 keV FWHM in repeated simulations of photopeak centroid estimation.

Figure 6.29 presents the measured 5089 keV peak centroids in Orion-α13. One

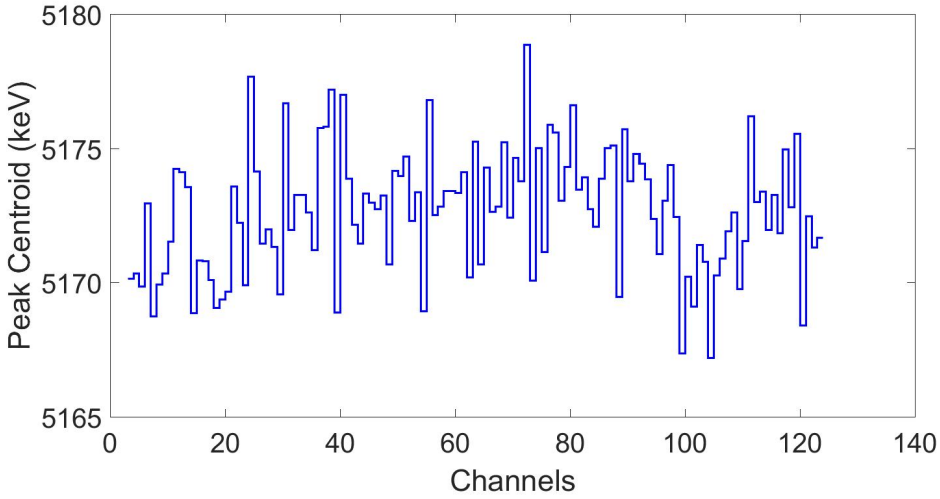

Figure 6.29: 5089 keV events peak centroid in each channel of Orion-α13.

could notice that the peak centroids could vary by up to 10 keV. By aligning the peak centroids at 5089 keV, one could observe a non-negligible improvement in energy resolution. Indeed, as Figure 6.30 presents, the single-pixel events spectra showed an improvement of 18 keV to 15 keV FWHM energy resolution for 5089 keV events in this detector. Because the 4.7 MeV peak events were not used to calibrate the non-linearity in the system, the improvement in this peak's resolution further confirms that the accuracy and precision of non-linearity correction. If the measured photopeak centroids for the 5089 keV were dominated by random noise, the resolution for the 4.7 MeV peak would not improve or degrade due to overfitting. As Figure 6.20 shows, the 5089 keV, single-pixel, cathode-side, no leak events showed 14 and 10 keV FWHM before and after peak alignment at 5089 keV.

6.4.5 Challenges for Edge-Pixel Events

The 5089 keV, single-pixel, cathode-side, no leak events spectra are presented in Figure 6.31. All nine detectors were combined for reasonable statistics. The data is shown separately for pixels in the center 9×9 region and the peripheral region.

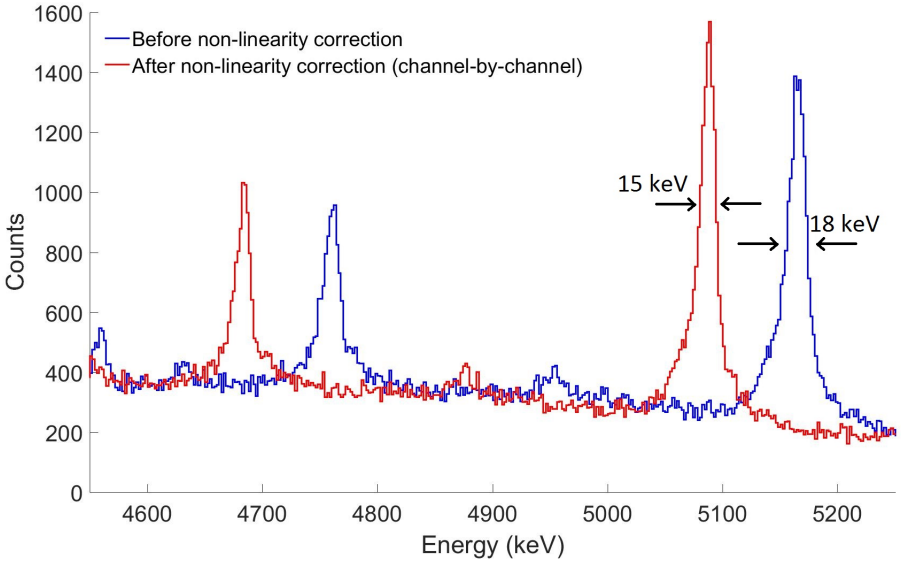

Figure 6.30: Single-pixel events spectra in Orion-α13 before and after channel-by-channel gain correction.

Both spectra were normalized to the total counts in the 5089 keV peak region to highlight differences in resolution. As expected, events from the edge pixels have worse resolution than those from the center 9×9 region. In the edge pixels, at most five neighbor pixels are read out for each single-pixel event. As a result, charge leak events are never well discriminated.

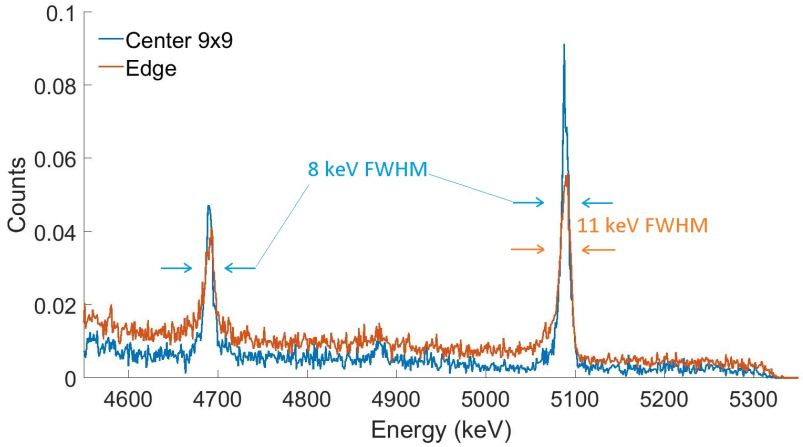

Figure 6.31: Non anode side, no leak, 5089 keV single-pixel events spectra for pixels in the center 9×9 and the peripheral regions.

The non anode-side, no leak, non-edge, single-pixel events reached about 8 keV

FWHM in both the 5.1 MeV peak and the 4.7 MeV peak. This value is very close to the theoretical expectation of 5 keV. It should be pointed out that the criterion of "no leak" events can only minimize the effect of charge leak. An event with a small amount of charge (several keV equivalent) leaked into one or more neighbor pixels does not necessarily get omitted in this selection. In addition, the linear model of neutron damage correction described in Equation 6.6 is not guaranteed to be perfect because annealing also takes place during the 15-day measurement. These two effects can still contribute to the single-pixel events resolution FWHM by a marginal value.

The above analysis does not directly contribute to the high-energy events reconstruction in current 3-D CdZnTe detectors. With all the imposed criteria for selection, the effective efficiency of the "best events" that achieve 8 keV FWHM is very close to zero. However, the analysis excludes the hypothesis that non-uniformity of trapping is the main reason that degrades high-energy events energy resolution. In addition, the analysis also shows that for single-pixel events, the resolution degradation cannot be explained using only one "dominating" factor. Instead, the degradation comes from various problems. Based on Figure 6.21, one could notice that the two most significant problems are anode-side resolution degradation and channel-by-channel non-linearity. Significant resolution improvement is expected only if these two problems are addressed.

6.5 Extra Challenges in Multi-Pixel Events

In Figure 6.19 it could be noticed that events with more triggered pixels show worse resolution. This degradation cannot be explained by the addition of electronic noise. Appendix A decomposes the peak width for two-pixel events in a similar way to Section 6.4. It is not included in this chapter to avoid redundancy. The analysis shows that the two main causes of two-pixel events resolution degradation are still anode-side events resolution degradation, and channel-by-channel non-linearity variation. With

more triggered pixels, however, it gets more difficult to decompose the resolution degradation factors in detail. Still, two important problems were identified.

6.5.1 WPCT and Energy Reconstruction

WPCT was found to be a challenge in multi-pixel events reconstruction. It degrades the energy resolution in the high-energy range through two mechanisms: variations of WPCT, and incorrect timing detection due to WPCT.

The current WPCT correction is not perfect in 3-D CdZnTe detectors. As discussed in Section 2.3, due to limited statistics, WPCT is only calibrated for three different types of two-pixel events: (1) both pixels are in the center 9x9 region, (2) both pixels are on the edge of the detector, and (3) one detector is on the edge and one is in the center. However, the effect of WPCT is different for each unique combination of pixels. As Figure 2.24 presents, the energy deficit from WPCT is more significant for pixel pairs that are closer to the peripheral region of a CdZnTe detector on the X- and Y-directions. At 662 keV, this systematic variation should not cause significant resolution degradation. However, WPCT is linear with the total energy: at higher energies the effect is more significant when quantified in keV. To show the effect of WPCT variation, a value r is derived by

$$r = \frac{\sum_{i=1}^{n} E_i \sqrt{{x_i}^2 + {y_i}^2}}{\sum_{i=1}^{n} E_i} \tag{6.9}$$

where n is the number of triggered pixels, E_i is the estimated energy in the i-th pixel, x_i and y_i represent the distance of the i-th pixel to the center of the detector. Using this calculation, a continuous feature is derived that estimates the effective distance of each event to the center of the detector on the X- and Y-directions. Figure 6.32 presents the total energy for the reconstructed 5089 keV, 4-pixel events energy compared against the values of r. It could be seen that for events closer to the center of the detector, energy is overestimated.

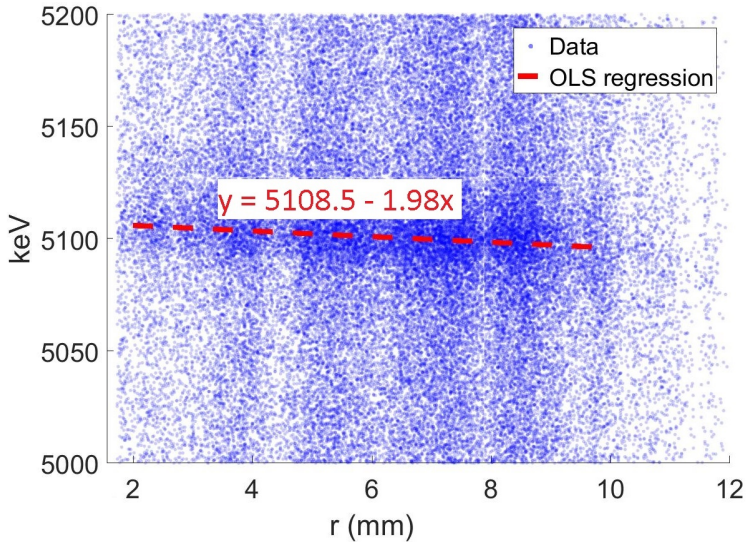

Figure 6.32: 5089 keV, four-pixel events energy vs. the derived, effective distance to the center of detector on the X- and Y-directions. The red dashed line is a linear regression to highlight the trend. It could be noticed the density of r is low for some values. This is because in Equation 6.9 x_i and y_i are discrete values corresponding to the center of each triggered pixel.

It should be noted although the trend in Figure 6.32 is significant, the feature r alone does not necessarily explain all the systematic WPCT variations in a 3-D CdZnTe detector. Because WPCT is a function of depth, in principle the WPCT should be corrected for each unique pair of voxels in the 3-D space. To make matters worse, because electron clouds are not infinitely small, the effective WPCT is also affected by electric field, trapping/de-trapping and deposited energy [13]. Using simulations to predict the systematic WPCT on a detector-by-detector basis is extremely challenging.

Another problem induced by WPCT is the inaccuracy of timing determination for side-neighbor events. Figure 2.13 already showed an example two-pixel event waveforms. The transient signals due to WPCT can cause under-estimation of timing difference between the cathode and anode signals. This propagates to underestimated depth of interaction [61]. Section II has introduced the WPCT calibration

and correction process in Figure 2.24 and Equation 2.11. For easier discussion they are presented again in Figure 6.33. It could be seen when the depth of interaction is underestimated the reconstructed energy is overestimated.

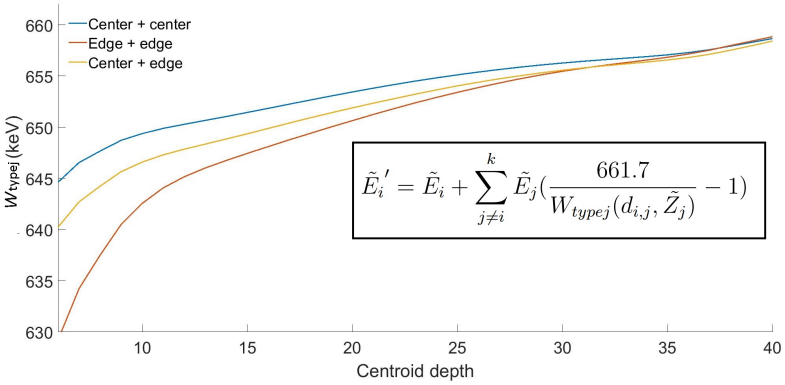

Figure 6.33: An example detector's WPCT calibration profile and the reconstruction algorithm.

To show the problem experimentally, Figure 6.34 compares the two-pixel, near-anode events spectra from a detector. Two types of events were chosen: Z_{diff} below 0 mm and over 1.5 mm. Z_{diff} is the difference of reconstructed depths in the primary and the secondary pixels. In a detector the depth ranges from 0 to 15 mm corresponding to the anode and cathode sides of a detector. Because of WPCT, the depth in the secondary pixel tends to be underestimated more significantly. As a result Z_{diff} is an estimation of the bias in depth estimation due to WPCT. It should be noted the true depth difference between the two parts of shared electron cloud can be non-zero because the electron cloud size can be several mm in the high-energy range. A large Z_{diff} indicates that there is a high likelihood that the depth is underestimated. Still, the two spectra in Figure 6.34 show significantly different peak centroids, indicating that the effect of biased depth estimation (due to WPCT) on energy resolution is non-negligible.

In Figure 6.33 it could be seen that the WPCT curves increase as a function of depth more quickly for near-anode events. In addition, for events near the anode the

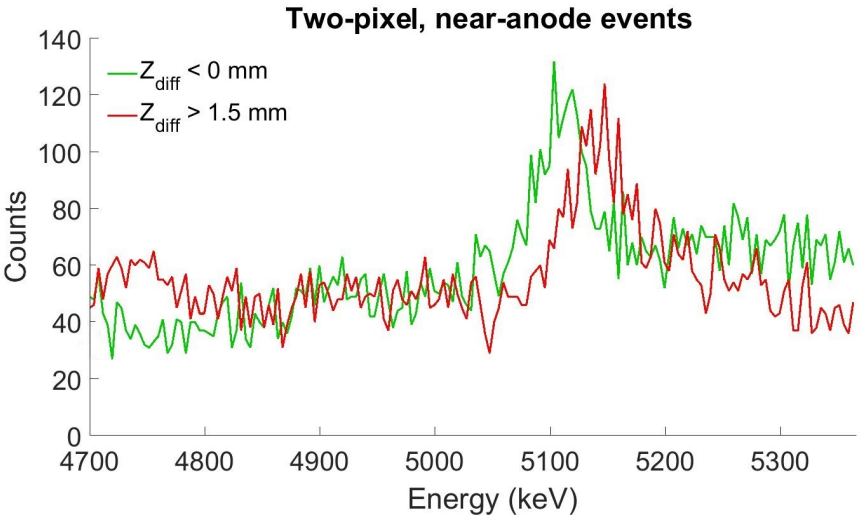

Figure 6.34: 5089 keV, four-pixel events spectra for different Z_{diff} values.

WPCT effect is also more significant. This means that the effect of WPCT on depth estimation should be corrected as a function of not only depth difference, but also the 3-D position of interaction.

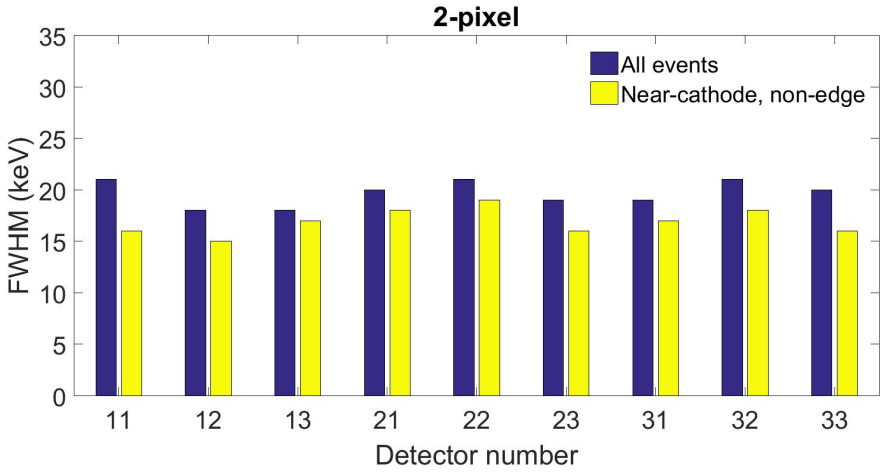

Figure 6.35: Resolution FWHM of 5089 keV, two-pixel events in each detector of the Orion-α system, and that from cathode-side, non-edge region in the same detector.

Figure 6.35, Figure 6.36 and Figure 6.37 present the two/three/four-pixel events resolution FWHM in each detector of the Orion-α system. For each type of events in each detector, the resolution is compared between events in the whole detector, and

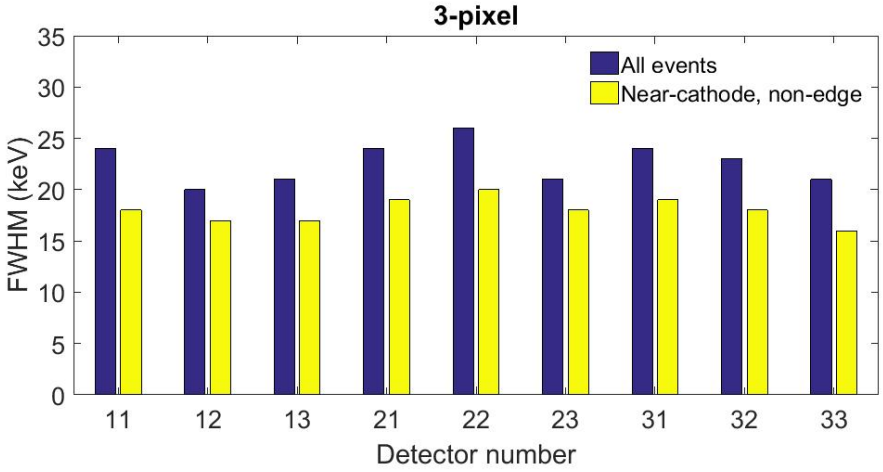

Figure 6.36: Resolution FWHM of 5089 keV, three-pixel events in each detector of the Orion-α system, and that from cathode-side, non-edge region in the same detector.

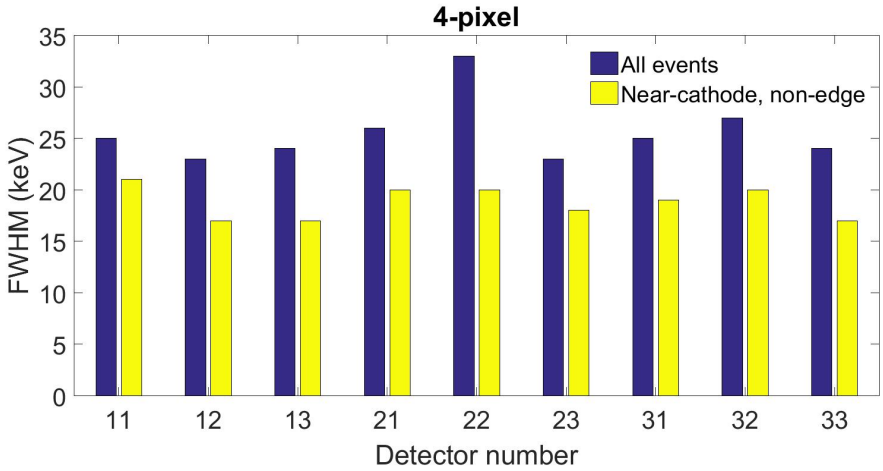

Figure 6.37: Resolution FWHM of 5089 keV, four-pixel events in each detector of the Orion-α system, and that from cathode-side, non-edge region in the same detector.

cathode-side, non-edge region events. A multi-pixel event is a cathode-side, non-edge event if the reconstructed depths are not in the near-anode half and no triggered pixels are in the peripheral region. This selection significantly improves the multi-pixel events resolution in the high-energy range, because the effect of WPCT changes more quickly as a function of interaction depth for near-anode events (Figure 6.33). With more triggered pixels, WPCT is more significant. As a result, the improvement is also most significant for four-pixel events.

Previously, attempts were made to correct for the above issues at 661.7 keV [65]. In the correction algorithm, the 661.7 keV photopeak centroid is measured for each unique combination of reconstructed depth, and ratio of energy deposited in the two pixels. This approach improves the two-pixel events resolution at 661.7 keV, but cannot be applied to above-3-MeV events because the electron cloud size is significantly larger and causes model mismatch.

Theoretically, the most accurate correction should be carried out using the detected high-energy interactions themselves. However, as discussed above, for each multi-pixel event the error of reconstructed energy is a function of multiple features including, but not limited to the X-, Y- and Z- locations of interaction and amount of energy deposited in each pixel. Because of limited efficiency in 3-D CdZnTe as well as the difficulty of acquiring commercially available high-energy gamma ray sources, specific calibrations for high-energy events on a detector-by-detector basis is very challenging.

The comparisons in Figure 6.35, Figure 6.36 and Figure 6.37 indicate that there is an alternative approach to address the energy resolution degradation caused by WPCT: in each detector, maximizing the region where the effect of WPCT is insignificant.

Chapter II showed that in pixelated CdZnTe detectors, for each anode pixel of interest, the weighting potential changes insignificantly in the cathode-side regions. An

intuitive explanation for this is that when an electron cloud drifts in the cathode-side region, the anode pixels "seem" identical. The weighting potential changes significantly only in the vicinity of the anode pixel. Hence, to reduce the effect of WPCT in each detector, the ratio between the anode pitch and the detector dimension should be decreased. In addition, to avoid raising more challenges in charge leak correction, the anode pixel pitch must not be further reduced. As a result, the most practical improvement should be increasing the detector size, while maintaining the pixel pitch.

The University of Michigan has already started to collaborate with both eV Products [66] and Redlen [12] to produce $4 \times 4 \times 1.5\,\mathrm{cm}^3$ CdZnTe detectors. An example crystal can be seen in Figure 6.38. These larger-volume CdZnTe detectors will be tested for high-energy events detection in the future, since they are expected to provide improved energy resolution in the high-energy range.

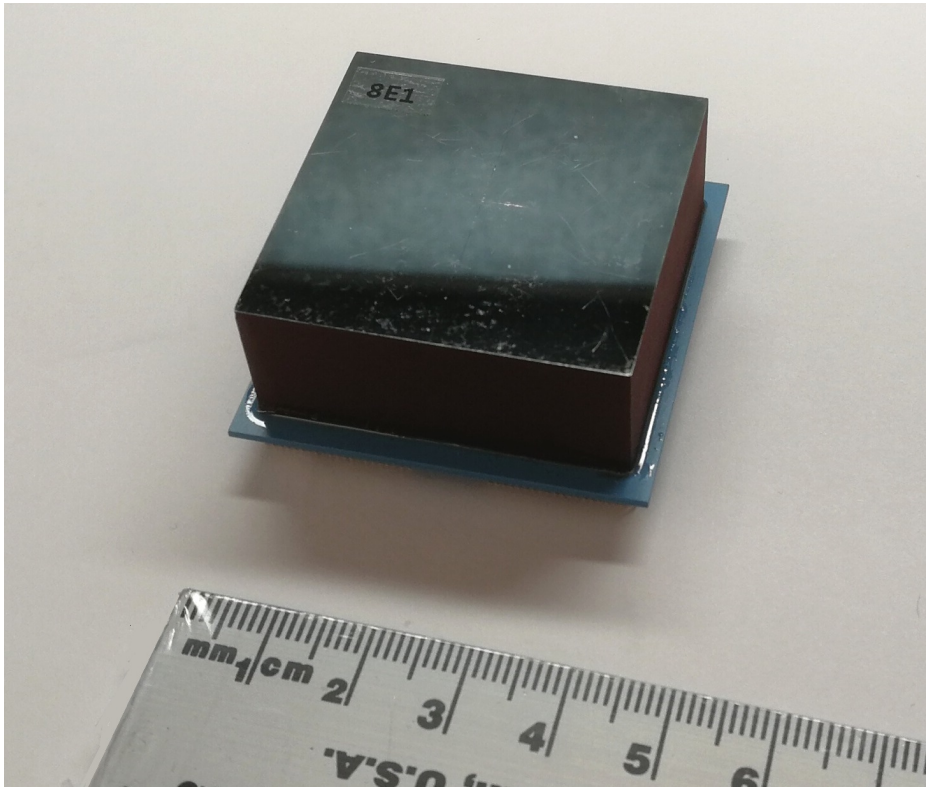

Figure 6.38: A $4 \times 4 \times 1.5\,\mathrm{cm}^3$ CdZnTe detector, delivered by eV Products. A ruler was included for scale.

6.5.2 Gain Deficit

"Gain deficit" is used to describe an issue on some 3-D CdZnTe detectors that have drastic variations of uncorrected photopeak positions for the gamma rays of the same energy [31]. Figure 6.39 presents the measured ^{137}Cs photopeak cutoffs in Orion-α22. The cutoffs are defined in Figure 2.3 of Section 2.3. The cutoff values directly reflect the uncorrected 661.7 keV gamma ray photopeak positions. It could be seen that many pixels in Orion-α22 showed cutoffs significantly lower than the others. These pixels are also referred to as "gain deficit" pixels.

1674	1674	1723	1728	1730	1729	1731	1729	1732	1730	1735
1674	1668	1723	1671	1733	1715	1733	1728	1728	1727	1730
1688	1667	1728	1737	1733	1736	1733	1689	1727	1729	1729
1671	1678	1732	1667	1739	1732	1736	1733	1729	1731	1727
1727	1726	1669	1673	1672	1722	1744	1742	1736	1734	1732
1729	1733	1738	1676	1743	1745	1740	1740	1729	1678	1727
1736	1729	1680	1735	1737	1742	1744	1737	1653	1728	1727
1733	1734	1735	1735	1740	1742	1737	1657	1732	1657	1727
1737	1676	1734	1733	1716	1739	1666	1661	1733	1730	1729
1737	1733	1682	1735	1734	1736	1734	1733	1734	1727	1729
1729	1730	1738	1705	1732	1734	1736	1736	1733	1734	1732

Figure 6.39: Uncorrected photopeak cutoffs (ADC) for 661.7 keV, single-pixel events in each pixel of Orion-α22.

Previously, gain deficit was treated as a secondary problem. Kaye argued that the pixels with gain deficit could still be energy corrected with the 3-D calibration algorithm described in Section 2.3 and that gain deficit only slightly degrades the signal-to-noise ratio [31]. However, in this work it was noticed that gain deficit could cause very significant issues for high-energy gamma ray reconstructions.

Figure 6.40 and Figure 6.41 present the reconstructed single-pixel and two-pixel SN events resolution FWHM in each pixel of Orion-α22. It should be noted for each

0.49	0.45	0.40	0.40	0.43	0.43	0.40	0.43	0.43	0.40	0.49
0.45	0.42	0.42	0.42	0.40	0.48	0.42	0.44	0.46	0.44	0.42
0.46	0.42	0.40	0.41	0.41	0.43	0.41	0.66	0.42	0.45	0.43
0.43	0.51	0.42	0.45	0.39	0.40	0.38	0.41	0.41	0.45	0.43
0.43	0.42	0.41	0.43	0.41	0.45	0.39	0.41	0.40	0.43	0.44
0.44	0.51	0.41	0.42	0.40	0.43	0.40	0.41	0.40	0.49	0.43
0.42	0.49	0.44	0.40	0.41	0.39	0.41	0.48	0.44	0.44	0.41
0.43	0.40	0.42	0.41	0.41	0.42	0.46	0.42	0.41	0.44	0.45
0.40	0.41	0.45	0.42	0.43	0.39	0.41	0.41	0.43	0.42	0.43
0.45	0.43	0.45	0.41	0.45	0.41	0.39	0.41	0.40	0.43	0.43
0.44	0.41	0.41	0.46	0.40	0.40	0.43	0.43	0.42	0.44	0.43

Figure 6.40: Single-pixel events energy resolution FWHM (%) in each pixel of Orion-α22.

0.73	0.87	0.97	0.78	0.76	0.72	0.74	0.84	0.78	0.66	0.72
0.87	0.97	1.08	0.88	0.86	0.80	0.89	0.89	0.93	0.83	0.84
0.83	0.95	0.86	0.81	0.90	0.86	0.94	1.01	1.00	0.97	0.85
0.91	1.03	1.13	1.10	1.06	0.88	0.96	0.93	0.91	0.99	0.86
0.82	0.88	0.99	0.89	1.16	0.85	0.83	0.82	0.84	0.96	0.94
0.74	0.75	0.98	0.96	1.02	0.74	0.83	0.87	1.06	1.08	1.03
0.66	0.85	0.95	0.95	0.80	0.90	0.93	1.05	1.22	1.12	0.93
0.68	0.81	0.90	0.88	0.85	0.87	0.99	1.11	1.19	1.20	0.91
0.75	0.96	1.02	1.03	0.88	0.95	1.17	1.12	1.10	0.96	0.85
0.73	0.93	0.97	0.92	0.81	0.82	0.90	0.89	0.88	0.79	0.73
0.77	0.77	0.85	0.84	0.79	0.72	0.80	0.77	0.71	0.73	0.73

Figure 6.41: Two-pixel SN events energy resolution FWHM (%) in each pixel of Orion-α22.

recorded two-pixel SN event, one count is added to the spectra of both pixels that share the energy. It could be noticed that although single-pixel events resolution is good except for a few bad pixels, the two-pixel SN events resolution is significantly degraded in the regions where gain deficit pixels are present. Interestingly, the degradation of two-pixel SN events resolution usually takes place when the energy is shared between a normal pixel and a gain deficit pixel. When both pixels have gain deficit issues, the energy resolution is still very good. An example could be seen in the upper left corner pixel. This pixel can only share its energy with two other SN pixels and all the three pixels have gain deficit issues. The recorded two-pixel SN events still showed 0.73 % FWHM resolution at 661.7 keV.

Apart from resolution degradation, when the energy is shared by two pixels that both have gain deficit, the reconstructed two-pixel SN events centroids are much higher than the expected 661.7 keV. Figure 6.42 presents the reconstructed two-pixel SN events peak centroid in each pixel. Unlike resolution degradation, energy overestimation happens as long as one of the two adjacent pixels have gain deficit issue. For example, the peak centroid of 661.7 keV, two-pixel SN events involving the upper left corner pixel was reconstructed to about 665 keV, even though the resolution is still very good.

With the digital readout system, analysis was conducted on waveforms directly read out from the anode pre-amplifiers. Figure 6.43 presents the measured 1.592 MeV, single-pixel events waveforms in detector Orion-α22. Each waveform is the concatenated result using eight neighbors and the collecting pixel. The waveform from the collecting pixel was normalized by 0.1 for easier observation. For easier analysis, only cathode-side (Z>30) events are shown.

It could be seen that in the pixels with gain deficit, the four SN pixels always have positive tail amplitudes. This indicates that in these pixels, a small amount of charge is always leaked into all the four SN pixels. Interestingly, for the same amount

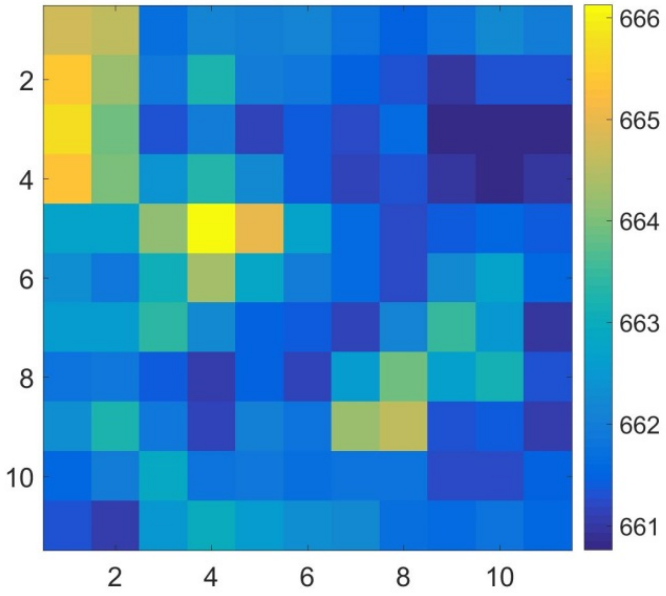

Figure 6.42: Two-pixel SN events peak centroid (keV) in each pixel of Orion-α22.

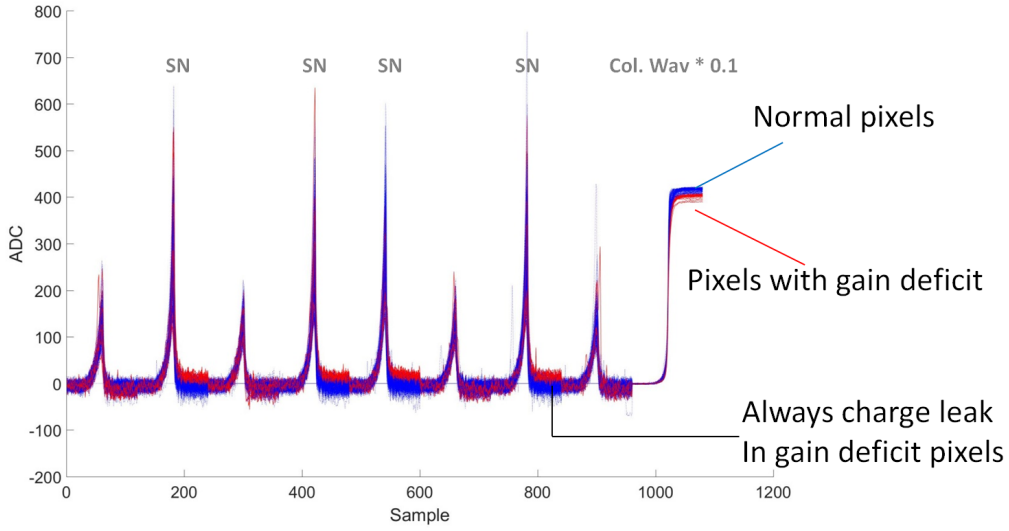

Figure 6.43: 1592 keV, single-pixel event waveforms for normal (blue) and gain deficit (red) pixels of Orion-α22.

of generated charge, the amount of leaked charge is almost constant. This conclusion is drawn based on the fact that the single-pixel events resolution does not degrade significantly for gain deficit pixels, as Figure 6.40 shows.

The above analyses on the waveforms are also consistent with the observations for two-pixel, SN events in Figure 6.41 and 6.42. In single-pixel events calibration, gain deficit pixels are calibrated using charge leak events. In two-pixel SN events that include at least one gain deficit pixels, a portion of the leaked charge is recovered implicitly because one of the adjacent pixel's waveforms are read out. As a result, the reconstructed two-pixel SN events spectrum peak centroid is higher than expected when at least one of the pixels have gain deficit issues.

As Kaye argued, gain deficit stems from problems happening on the anode surface because no depth dependence could be observed [31]. However, the exact mechanism could not be found. Over the course of this study, it was found that the gain deficit issue could be temporarily mitigated using a "heat shock". In this process, the detector is put in an environmental chamber and the ambient temperature was quickly increased from room temperature to 80 ^{o}C in ten minutes. Immediately after this, the ambient temperature was reduced to room temperature in ten minutes. In all the tested samples, it was found that the heat shock process significantly reduced the number of gain deficit pixels in each detector. Figure 6.44 presents the 661.7 keV photopeak cutoffs in the anodes of an example detector, 5R-36, before and after heat shock. It could be seen that about 50 % of the pixels had gain deficit issues. After the heat shock, the map of cutoffs became very uniform over all the pixels.

Unfortunately, it was observed that the gain deficit problem started to show up in the problematic pixels again over the following weeks. Still, the observations in this experiment provide useful information about the mechanism behind gain deficit issues. The heat shock takes only a very short period of time, hence the effect of ambient temperautre change should only significantly affect the surface of a 3-D

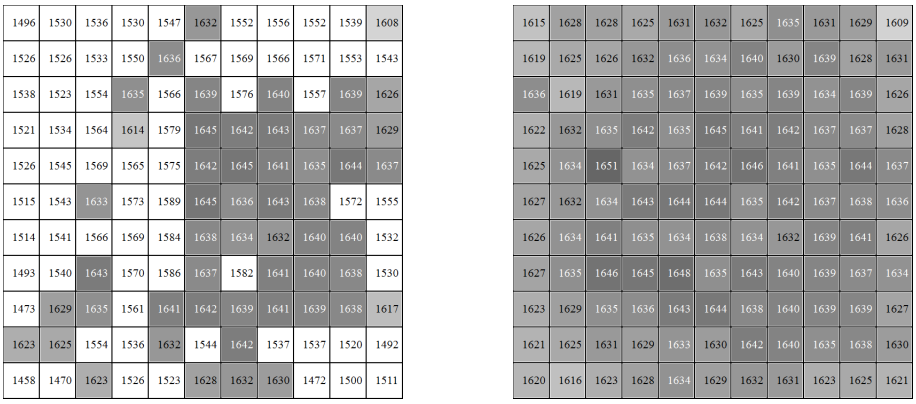

(a) Before heat shock (b) After heat shock

Figure 6.44: 661.7 keV photopeak cutoffs before and after the heat shock in detector 5R-36. Dark colors represent larger values.

CdZnTe detector. These observations indicate a possible hypothesis that the gain deficit is caused by thermal tension. In previous studies, Redlen reported that thermal tension might build up in the adhesive that connects the detector's anodes and the PCB board that carries the detector. The adhesive layer consists of a large number of pieces with different coefficients of thermal expansion. Because the adhesive is cured at temperatures between 50 to 80 ^{o}C, a thermal tension could show up at room temperature [67]. Perhaps, it is the thermal tension that degrades the connection by increasing the resistance, or inducing a capacitor, between the detector anode and the pre-amplifier. After a heat shock this thermal tension could be relieved temporarily.

The gain deficit issue is expected to affect high-energy events resolution more significantly because the fraction of multi-pixel events is expected to increase with larger electron cloud sizes. The more multi-pixel event, the more susceptible the system is to gain deficit because a gain deficit pixel is more likely to be involved in an event with many triggered pixels. Figure 6.45 presents the reconstructed 5089 keV, four-pixel events spectra in Orion-α22 and Orion-α13. Unlike Orion-α22, Orion-α13 does not have any gain deficit problems. It could be seen that in Orion-α22, many pixels spectra showed more than one peaks, or only a blurred hump at 5089 keV. This

is because in a four-pixel event, the charge can be shared by different combinations of neighbor pixels. The reconstructed peak centroid is significantly affected by the amount of pixels that have gain deficit issues. In contrast, Orion-α13 showed very uniform responses. A clear peak is formed in each pixel at 5089 keV. The gain deficit issue caused the poor resolution for 3- and 4-pixel events in Orion-α22 as shown in Figure 6.19. To conclude, detectors with gain deficit can degrade multi-pixel events resolution very significantly.

In recent years the gain deficit issue appear less frequently in Redlen detectors. Detectors with gain deficit are usually detected by Redlen directly and excluded from delivery. However, this issue still affects the yield significantly and hinders the cost of production from further decreasing. In the future, coordinated efforts should be made between Redlen and the University of Michigan to eliminate the underlying physical mechanism that causes gain deficit.

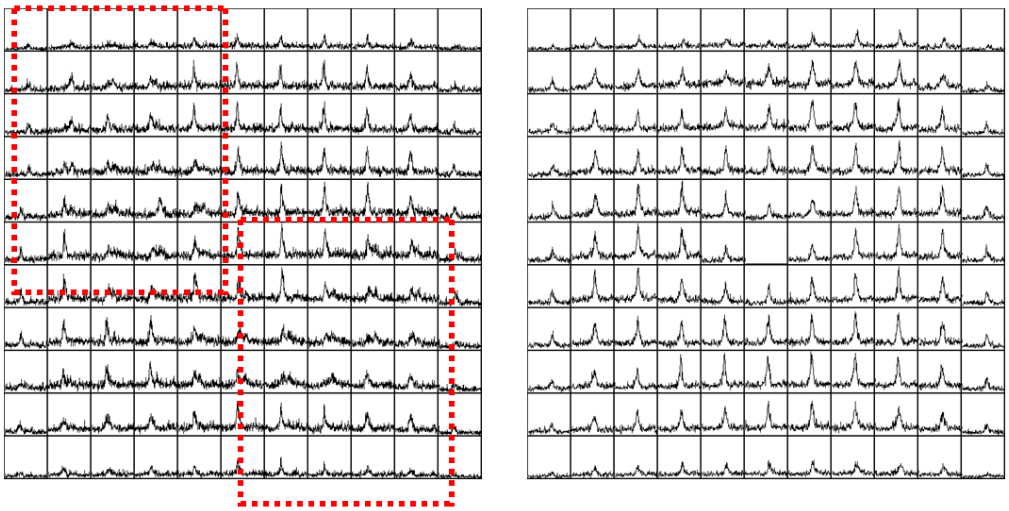

Figure 6.45: (Left) Four-pixel events spectra at 5089 keV for each pixel in Orion-α22. (Right) Four-pixel events spectra at 5089 keV for each pixel in Orion-α13.

6.6 Waveform Processing Options

The discussions above focused on events reconstruction after using simple subtraction to process the waveforms. This section attempts to justify the use of simple-subtraction in these measurements.

Chapter II mentioned that simple-subtraction works better than trapezoidal filters in charge sharing events, and vice versa for Compton scattering events. SRF fitting combines the advantages of both trapezoidal filter and simple-subtraction at the cost of more computation time. In the high-energy region, current 3-D CdZnTe detectors only detect pair-production, double-escape peaks. Most of the multi-pixel events corresponding to these energies were single interaction, charge sharing events. For charge sharing events, SRF fitting is not advantageous compared to simple subtraction. Figure 6.46 presents the high-energy, multi-pixel events spectra in Orion-α13. Both simple-subtraction and SRF fitting were used to process the waveforms. It could be noticed that identical peak widths were achieved, as expected.

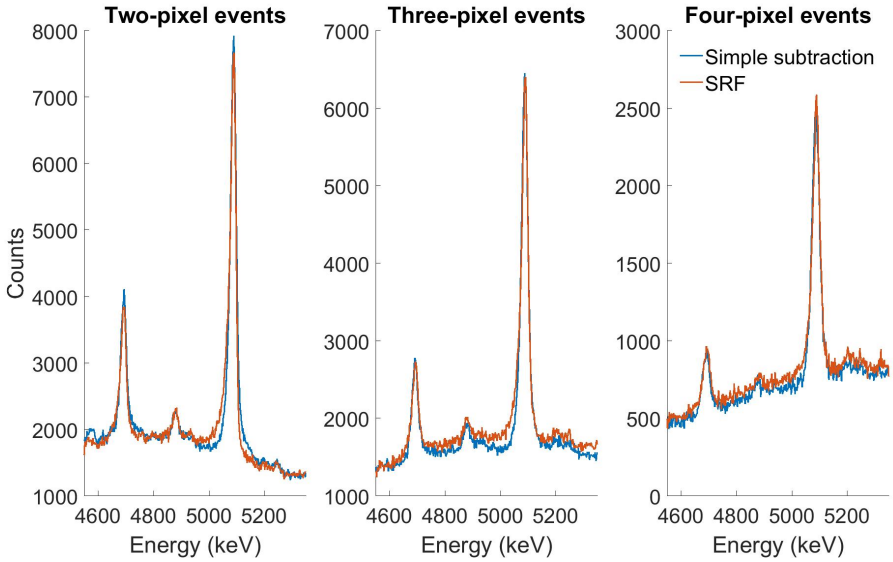

Figure 6.46: High-energy, multi-pixel events reconstruction results in Orion-α13. The waveforms were processed by SRF fitting and simple-subtraction separately. Identical peak widths were observed.

It should be noted that the spectra from SRF fitting have marginally more events

compared to those from simple-subtraction. This is because SRF fitting is more stable in estimating depth of interactions. In total, about 5% events from simple-subtraction were omitted in events reconstruction due to bad depth estimation, while 1% events were lost in data from SRF-fitting. However, this marginal decrease in omitted data using SRF fitting does not justify the drastic increase of processing time complexity.

At lower energies, simple subtraction proved better than trapezoidal filtering for charge sharing events because trapezoidal filtering is more susceptible to transient signals. This is still true for high-energy events. Figure 6.47 presents the reconstructed total energy, compared against "energy ratio" in three-pixel events detected in Orion-α13. The energy ratio is defined as the energy in the primary pixel, divided by the total energy in each event. A larger energy ratio means that the charge is more asymmetrically shared among the pixels. In these events, the transient signals on non-primary pixels are expected to be larger. As one could notice in Figure 6.47, events with larger energy ratios showed overestimation of energies when processed by trapezoidal filter. In contrast, simple-subtraction results were not significantly affected by this issue.

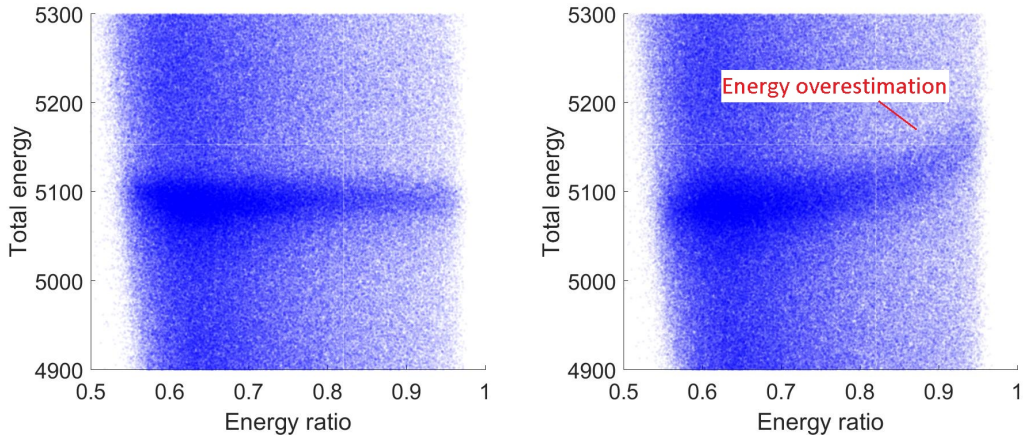

(a) Processed using simple-subtraction

(b) Processed using trapezoidal filter

Figure 6.47: Total energy vs. energy ratio in three-pixel events detected in Orion-α13.

Figure 6.46 indicates that simple-subtraction and SRF fitting have similar performance in the high-energy measurements, while simple-subtraction is much faster than SRF fitting. On the other hand, though trapezoidal filter is as fast as simple-subtraction, Figure 6.47 shows its results are at most as good as simple-subtraction, assuming that extra steps can be taken to correct for the artifact due to transient signals perfectly. Hence, simple-subtraction should be the first choice in processing high-energy waveforms in current 3-D CdZnTe detectors.

6.7 Summary

This chapter introduces experiments measuring high-energy, pair-production double-escape events in 3-D CdZnTe detectors. Multiple energy resolution degradation mechanisms were observed for both single-pixel and multi-pixel events.

The analyses first focused on single-pixel events. Neutron damage was observed in the detector and the effect on resolution could be corrected assuming the increase of trapping was constant over time. For non-anode-side, low charge leak, center 9×9 pixels, the single-pixel events could achieve 8 keV FWHM at 5089 keV using channel-by-channel non-linearity correction. Without the expensive channel-by-channel non-linearity correction, the non-anode-side, low charge leak events could achieve 14 keV FWHM. With all the non-anode-side events, single-pixel, 5089 keV events can achieve 16 keV after charge leak correction. The non-negligible size of electron cloud in the high-energy range further degrades the energy resolution in the anode side due to the drastic change in weighting potential. Overall, 20 keV FWHM is observed in single-pixel, 5089 keV events.

For all multi-pixel, high-energy events are subject to more problems due to WPCT. Because of limited 3-D CdZnTe detector efficiency for high-energy events and the high-dimensionality in this effect, it was challenging to develop a practical correction algorithm. Fortunately, larger-volume, pixelated CdZnTe detectors are under

development and they are expected to provide better results.

The corrected spectra from the 15-day measurement using Orion-α is shown in Figure 6.48. This represents the current state-of-the-art performance of 3-D CdZnTe high-energy gamma-ray detectors. Though the resolution is significantly better than scintillator detectors, there is still non-negligible room for improvement.

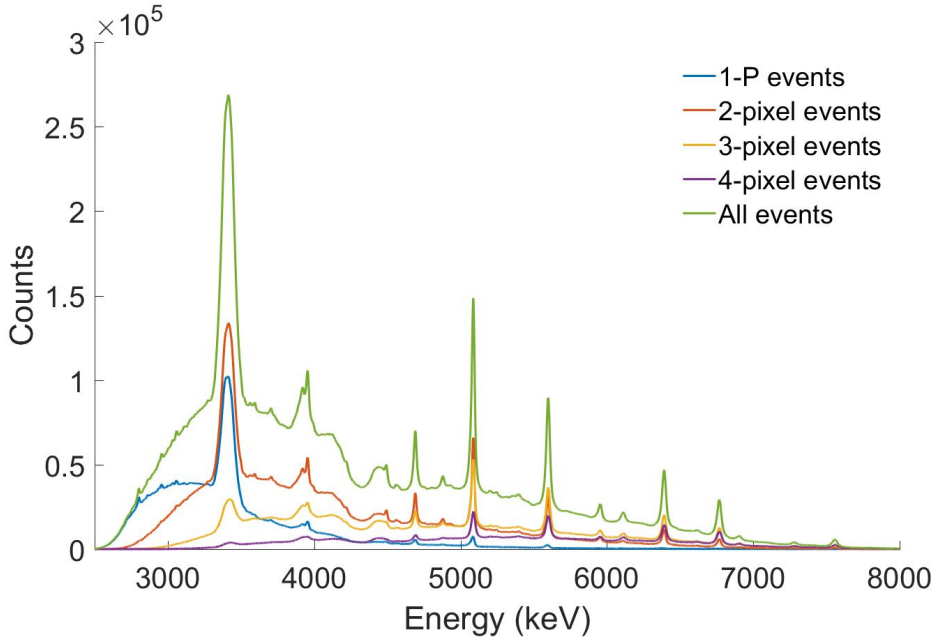

Figure 6.48: All events spectra from the 15-day measurement.

CHAPTER VII

Electron Cloud Distribution Estimation Method

Conventional waveform processing methods mentioned in Chapter II ignore the distribution of electron clouds due to limitation by electronic noise and pixel pitch. The pixel pitch in 3-D CdZnTe is 1.72 mm, much larger than typical electron cloud sizes from gamma ray interactions below 1 MeV. However, characterization of charge cloud distribution in semiconductor detectors can be very beneficial. For example, if the charge cloud distribution is known for gamma-ray interactions, the reconstructed Compton imaging cone for each event can be reduced to an arc, and the background can be greatly reduced [68]. Also, with the same energy, gamma ray and charged particles deposit energy in matter at different rates. Hence, charge cloud distribution estimation could help discriminate different types of interactions [69]. In addition, estimation of charge distribution can help the studies of charge collection in semiconductor detectors. With improved electronic noise in readout electronics, estimation of charge clouds in 3-D CdZnTe detectors becomes likely.

In 2012, Zhu tried to use maximum likelihood estimation (MLE) [70] to model the signal induction process in 3-D CdZnTe detectors. The method assumes in a 3-D position sensitive CdZnTe detector, the signals induced on electrodes are the summation of noise and a linear 4 transformation of the SRF matrix to charge clouds. Expectation-maximization (EM) was used to solve the problem. However, very slow

convergence was reported using the EM method. In addition, the result was biased because of the discretized modelling of the noise component in the system [18]. In this chapter, a similar signal model is used, but the problem was solved by constrained optimization [70]. This process is more robust because it requires less assumptions in the noise model. In addition, many mature solvers are available to speed up the calculations. To mitigate the ill-posedness in this inverse problem, two different regularization terms were introduced in the objective function. The method was tested using simulated electron clouds and a measured system response matrix in 3-D position-sensitive CdZnTe detectors. The average error in electron cloud estimation was significantly reduced by regularization. The method was applied to digitized waveforms for single-pixel muon interaction events in 3-D position-sensitive CdZnTe detectors.

7.1 Linear System Signal Model

This study focuses on single-pixel events where charge is collected by only one anode pixel. However, the same principle can be applied to other events with more triggered pixels. By the superposition principle, the charge signal induction in 3-D CdZnTe detector electrodes is a linear process. Assuming no noise is present and the electron cloud is continuous under the space of a pixel, the expected signal amplitude on the anode ($m(t)$) is given in Equation 7.1.

$$m(t) = \iiint_V p(x, y, z, t)c(x, y, z)\, dx\, dy\, dz \tag{7.1}$$

In Equation 7.1, t represents time, V represents the whole space under the collecting pixel. $p(x, y, z, t)$ represents the expected signal for one unit of point charge generated at position (x, y, z). $c(x, y, z)$ represents the distribution of charge under the whole pixel. It is also assumed no charge is leaked to the gap or neighbor pix-

els. The sub-pixel location of each gamma-ray interaction can be calculated using the algorithm introduced in Section 2.3. Due to electronic noise and the size of electron clouds, each pixel can only be divided into a limited number of sub-pixel voxels ($I \times J \times K$), where I, J and K represent the number of partitions in X, Y and Z directions respectively. In 3-D CdZnTe detectors, I and J could be as large as 11, while K is 40, as mentioned in Chapter II. The partitions are based on the limit of sub-pixel position sensing in 3-D CdZnTe [18]. The expected signal $p(i, j, k, t)$ for charge in each sub-pixel voxel (i, j, k) is calculated by taking the average over a large amount of photopeak events for a fixed energy. Equation 7.1 is then re-written in a discrete form:

$$m(t) = \sum_{b=1}^{B} p(i, j, k, t)c(i, j, k). \tag{7.2}$$

where t is also discrete because the VAD_UM ASICs read out digitized samples of each waveform. $B = I \times J \times K$ and it represents the total amount of sub-pixel voxels under the collecting pixel. For easier discussion Equation 7.2 is re-written again in matrix form:

$$\vec{m} = P\vec{c} + \vec{n}. \tag{7.3}$$

Signal $\vec{m}$ and charge distribution $\vec{c}$ are both column vectors with dimensions $M \times 1$ and $B \times 1$ respectively (M represents the discrete sampling times). Another $M \times 1$ vector $\vec{n}$ is also added to represent electronic noise that is zero-centered in the waveform. Each row in the $M \times B$ matrix P represents the expected signal for one unit of charge generated in each sub-pixel voxel. P is also called the system response functions (SRFs) in 3-D CdZnTe detectors [18].

For each event, information of interaction position is encoded in the measured waveforms in electrodes. Fig. 7.1 and Fig. 7.2 show examples of two sub-pixel voxels

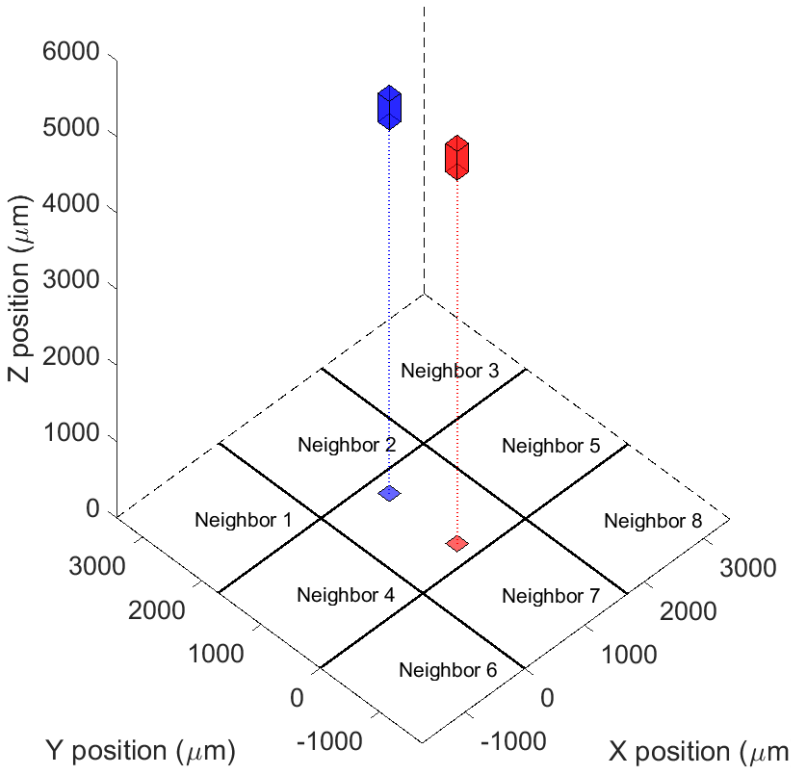

Figure 7.1: Examples of two sub-pixel voxels in the 3-D space and their corresponding projections onto the collecting anode pixel. For simplicity, the width of gaps between adjacent anode pixels is ignored. For each event, the digital ASIC could read out the waveforms from both the collecting anode pixel and all the eight neighbor pixels. The two voxels are both 5000 μm away from the collecting anode, but on opposite sides on the collecting anode along the Y direction.

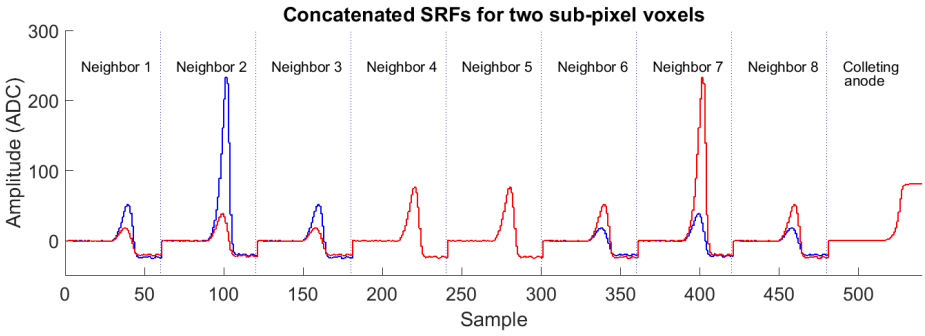

Figure 7.2: Examples of measured SRFs for the two sub-pixel voxels shown in Fig. 7.1. The same colour is used for each corresponding sub-pixel voxel and waveform pair. Each SRF is the concatenation of waveforms read out simutaneously from all nine anode pixels. The waveform in collecting anode was re-scaled by 0.1 for easier demonstration.

in 3-D CdZnTe detector and the corresponding measured SRFs. It can be noticed that the SRFs measured in neighbor pixels close to the sub-pixel voxel have higher amplitudes than the SRFs from other neighbor pixels.

7.2 Cloud Distribution Estimation

The process of electron cloud distribution estimation is given the measured waveform ($\vec{m}$) for an event, based on the SRFs (P), deduce the initial distribution of electron cloud $\vec{c}$ with the existence of noise $\vec{n}$. The deduction can be done by MLE. Assuming electronic noise $\vec{n}$ follows a multivariate Gaussian distribution with expectations at zero, for each event, $\vec{c}$ is adjusted until the likelihood of detecting $\vec{m}$ is maximized:

$$\begin{aligned}\hat{\vec{c}} &= \underset{\vec{c}}{\text{argmax}} \quad \exp[-\frac{1}{2}(P\vec{c}-\vec{m})^T\Sigma^{-1}(P\vec{c}-\vec{m})] \\ &= \underset{\vec{c}}{\text{argmin}} \quad [(P\vec{c}-\vec{m})^T\Sigma^{-1}(P\vec{c}-\vec{m})] \\ &= \underset{\vec{c}}{\text{argmin}} \quad [\vec{c}^T P^T\Sigma^{-1}P\vec{c} - 2\vec{m}^T\Sigma^{-1}P\vec{c}]\end{aligned} \tag{7.4}$$

The function to be minimized in Equation 7.4 is also known as the objective function. In Equation 7.4, Σ represents the covariance matrix of noise $\vec{n}$ and can be measured heuristically in the system. $\hat{\vec{c}}$ represents the estimation of electron cloud distribution. Two constraints are also necessary for this problem. First, the electron distribution should always be non-negative. Second, the total deposited charge under the collecting pixel should be a fixed number. These constraints are presented in Equation 7.5:

$$
\begin{aligned}
c(b) &\geqslant 0, \forall b \in [1, B] \\
\sum_{b=1}^{B} c(b) &= C
\end{aligned}
\tag{7.5}
$$

In Equation 7.5, b is the index of the sub-pixel voxel ranging from 1 to B. For each event, C is a constant representing the total amount of charge under the collecting pixel. It can be approximated by the reconstructed energy [18]. Equation 7.4 and Equation 7.5 describe a typical quadratic programming problem that can be solved by many available solvers. In this study, MATLAB *quadprog* and IBM $CPLEX$ functions were used [71, 72]. Both functions have identical solutions using the interior point method [70]. *quadprog* was convenient for prototyping, while $CPLEX$ was much faster using parallel computing.

7.3 Simulation Tests and Regularization

The tests of Equation 7.4 and 7.5 started with simulations. SRFs (P) were first generated using Maxwell [16] to calculate the weighting potential field and assuming that electrons move at a constant speed towards the collecting anode. The Maxwell calculation also neglects the trapping and de-trapping of electrons. It should be noted this calculated SRF matrix P is a "perfect" model due to the simplifications. The problems with realistic SRFs will be discussed in subsequent paragraphs. Each electron cloud ($\vec{c}$) was simulated by GEANT4 package [60], and assumed that the number of electron-hole pairs is linear with deposited energy. The corresponding measured waveform was simulated using Equation 7.3, where $\vec{n}$ was randomly selected from a database of measured noise from the detectors and re-scaled to simulate different noise levels. A constrained inverse problem is usually ill-posed [73]. As Figure 7.3 shows, the estimated cloud was not completely the same as the simulation. With increasing

noise, the estimated cloud becomes more inaccurate due to this ill-posedness.

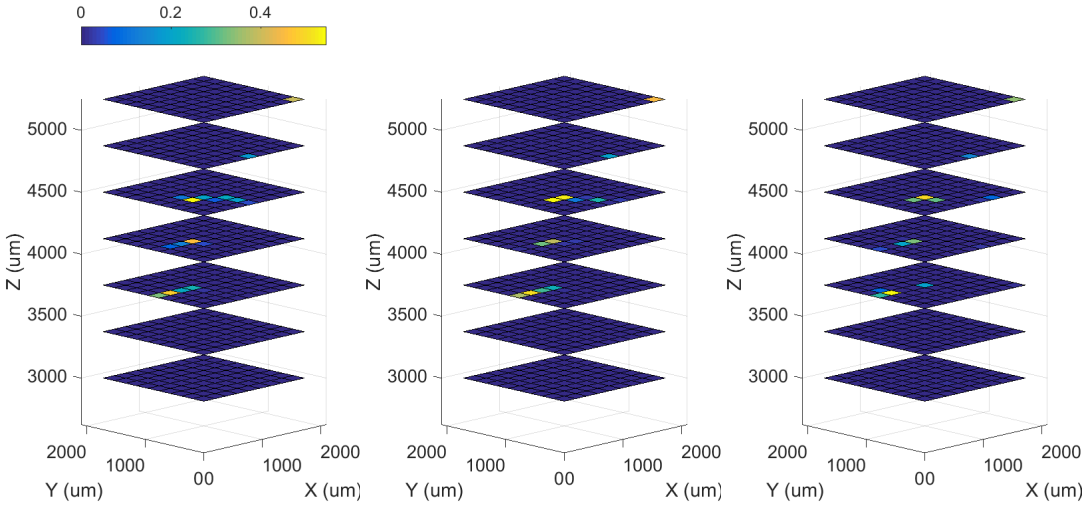

(a) Simulated cloud (b) Estimation w/ zero noise (c) Estimation w/ 2 keV noise

Figure 7.3: Estimated electron clouds with different noise (equivalent energy spectrum peak FWHM), compared with the original simulation. The space over the collecting pixel is separated into layers of discrete charge for easier observation. The agreement between estimation and simulated cloud decreases with increasing noise level.

In real scenarios, the estimation process is faced with two additional problems: model mismatch and increased ill-posedness.

Model mismatch means that the measured SRF matrix P is not exactly the same as the true SRF matrix. This problem results from several factors. First, previous studies showed that CdZnTe can have many non-uniform trapping/de-trapping sites [59]. Second, the electric field of 3-D CdZnTe detector is usually not uniform [33]. These two issues cause the true SRF to be slightly different in every pixel in a detector. However, practically SRFs must be measured using averaged waveforms from all the inner 9×9 pixels. As a result, a mismatch exists between the estimated SRFs and the true SRFs for each collecting pixel. In addition, the depths of interactions very close to the anodes are very inaccurate due to fast changes of weighting potential fields [27]. Last but not least, charge sharing [61] is not avoidable in the measurement of SRFs

(P) and causes more model mismatch when the electrons are generated near the edge and corner of the collecting pixel.

The ill-posedness of the estimation process increases in real scenarios because the true SRF matrix is no longer a "perfect" model that neglects trapping/de-trapping and uses uniform electric field. Instead, the problems described in the previous paragraph make the MLE model harder to solve with the existence of noise. To prove this, the simulation shown in Figure 7.3 was repeated, however the "perfect" SRF matrix P was replaced with the measured SRFs. As Figure 7.5 presents, when the measured SRFs were used with simulated electron clouds, the estimation becomes very inaccurate.

To improve the estimation results, regularization methods must be introduced [70]. The regularization can make use of assumptions that the electron cloud size should not be infinitely large, and the distribution is more likely to be continuous [27, 68]. Two different regularization approaches were then considered in this study: distance regularization and smoothing regularization.

The objective function in Equation 7.4 is updated by adding the two regularization terms:

$$\hat{\vec{c}} = \underset{\vec{c}}{\operatorname{argmin}} \quad [\vec{c}^T(P^T\Sigma^{-1}P + k_1\Lambda + k_2\Omega)\vec{c} - 2\vec{m}^T\Sigma^{-1}P\vec{c}] \tag{7.6}$$

where Λ is the distance regularization matrix, Ω is the smoothing regularization matrix, and k_1, k_2 represent the regularization coefficients respectively.

Λ is a $B \times B$ diagonal matrix

$$\Lambda = \begin{bmatrix} \lambda_{11} & 0 & \dots & 0 \\ 0 & \lambda_{22} & \dots & 0 \\ \vdots & \vdots & \ddots & \vdots \\ 0 & 0 & \dots & \lambda_{BB} \end{bmatrix} \tag{7.7}$$

where each diagonal element λ_{ii} is the squared Euclidean distance between position of i-th sub-pixel voxel, $\vec{x_i}$, and an initial estimation of the interaction position $\vec{x_0}$:

$$\lambda_{ii} = \|\vec{x_i} - \vec{x_0}\|_2^{\,2}. \tag{7.8}$$

The initial estimation is based on the sub-pixel position sensing technique [18]. This technique is briefly introduced in Section 2.2.4. It gives a fast, yet inaccurate estimation of the average electron cloud centroid. This regularization, also known as Tikhonov regularization [70], helps penalize estimations that have charge too far away from the initial guess.

Elements (ω_{ij}) in the smoothing regularization matrix (Ω) are calculated by

$$\omega_{ij} = \begin{cases} \sum_{n=1}^{B} \delta(\vec{x_n}, \vec{x_i}), & \text{if } i = j \\ -\delta(\vec{x_i}, \vec{x_j}), & \text{otherwise} \end{cases} \tag{7.9}$$

where $\delta(\vec{x_i}, \vec{x_j})$ is non-zero only when sub-pixel voxels i and j are adjacent to each other:

$$\delta(\vec{x_i}, \vec{x_j}) = \begin{cases} 1/\|\vec{x_i} - \vec{x_j}\|_2^{\,2}, & \text{if i and j are adjacent voxels} \\ 0, & \text{otherwise.} \end{cases} \tag{7.10}$$

The smoothing regularization described in Equation 7.9 and 7.10 is also known as a Total Variation regularization [70] that takes the physical sub-pixel voxel sizes into account. It helps penalize estimations that have big variations in charge from adjacent sub-pixel voxels.

It should be noted that both regularization methods can result in biased estimations. The higher energy deposited in an interaction, the more extended the electron cloud could be. As a result, the electron cloud size might be underestimated by the distance regularization. For the smoothing regularization, estimations with presence

of characteristic X-rays and Bremsstrahlung X-rays will be penalized. The optimal regularization coefficients k_1 and k_2 and corresponding estimation improvements might differ for various event types and deposited energies.

Fig. 7.4 shows results from regularization coefficients grid search for 2614 keV photoelectric events. 2 keV electronic noise was added to the waveforms. Summed square errors were calculated to evaluate the error between the ground truth simulated electron cloud and the corresponding estimation.

The summed square error calculation is shown in Equation 7.11 where c_i^p and $\hat{c_i^p}$ represent the simulated and estimated density in i-th sub-pixel voxel in the p-th electron cloud, respectively. A total of 100 electron clouds were simulated from GEANT4. The number of clouds is relatively small because solving each problem is time-consuming. The mean squared error (MSE) among the 100 electron clouds is calculated in 7.11.

$$SE_p = \sum_{i=1}^{B} \left(\frac{\hat{c_i^p}}{\sum_{i=1}^{B} \hat{c_i^p}} - \frac{c_i^p}{\sum_{i=1}^{B} c_i^p}\right)^2 \tag{7.11}$$

$$MSE = \frac{1}{100} \sum_{p=1}^{100} \sum_{i=1}^{B} \left(\frac{\hat{c_i^p}}{\sum_{i=1}^{B} \hat{c_i^p}} - \frac{c_i^p}{\sum_{i=1}^{B} c_i^p}\right)^2 \tag{7.12}$$

Each data point in Fig. 7.4 was the MSE from all the 100 electron clouds using each combinations of k_1 and k_2 regularization coefficients. It could be seen that the optimal regularization terms reduced the average summed square error by about 60%. Figure 7.5 presents an example showing that the regularization terms helped reducing the error of estimation significantly when the measured SRFs were used.

7.4 Verification Using Muon Events

Unfortunately, as Figure 7.3 shows, the current estimation can only partition the 3-D space into sub-pixel voxels with about 200 μm in lengths. With this precision,

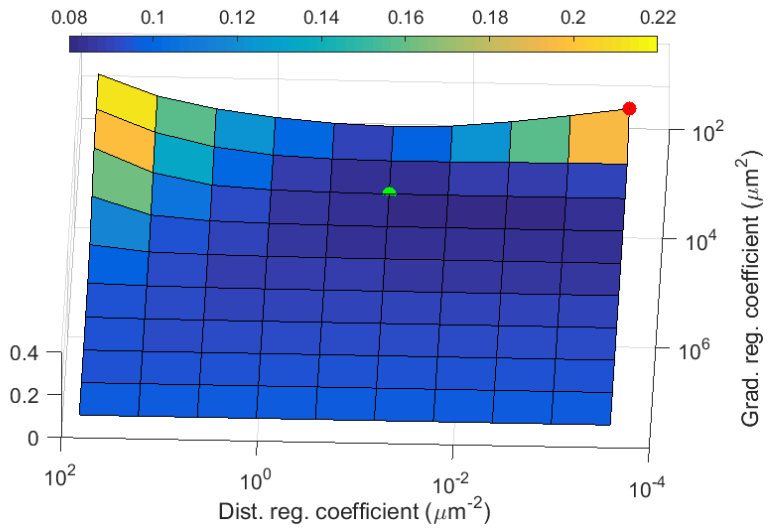

Figure 7.4: 100 electron clouds from 2614 keV photoelectric events were simulated from GEANT4. for each combination of regularization coefficients, the mean value of summed square error was calculated in the 100 electron clouds. The red dot represents the reconstructions without regularization, while the green dot represents the reconstructions with lowest mean square error.

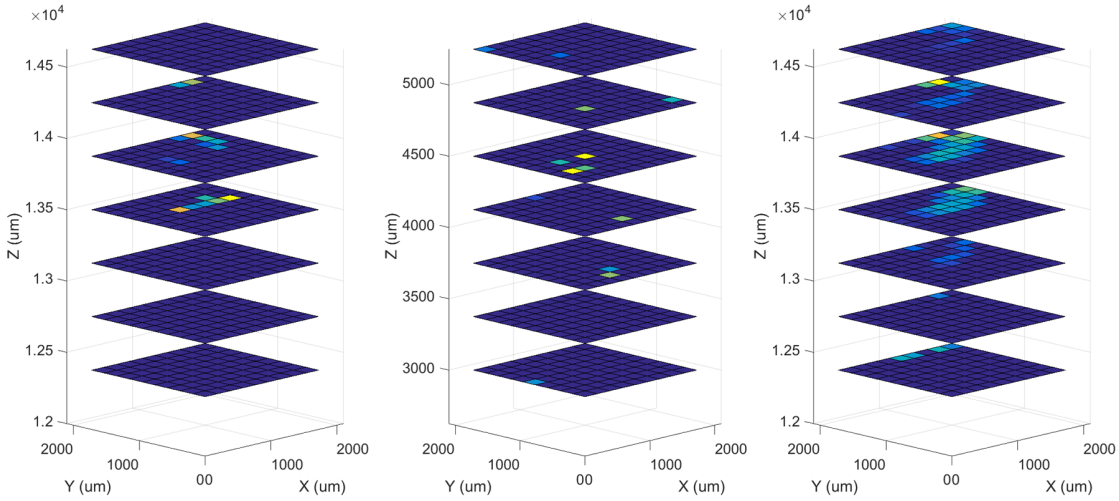

Figure 7.5: Left: a simulated electron cloud from a 2614 keV photoelectric effect. Middle: the reconstruction without regularization results into false hot spots. Right: the reconstruction with optimal regularization coefficients for 2614 keV interactions.

only the orientation of the electron clouds, instead of the incoming gamma ray's direction, could be estimated [18]. In addition, the ill-posedness shown in Figure 7.5 raises more challenges in the accuracy of estimation. As a result, the estimation method is not good enough to improve the Compton imaging capability in 3-D CdZnTe detectors. However, the estimation method could potentially be applied to distinguish interactions from high-energy (several MeV) particles. These events have very high signal-to-noise ratio and the estimation should be easy.

Measured waveforms from single-pixel, cosmic muon interaction events were used to evaluate the feasibility of the optimization method. Muon particles were used because they result in well understood charge cloud distributions. For energetic, cosmic muon interactions, the true electron cloud should exist along a line across the pixel from anode to cathode.. In addition, since muons have constant linear energy transfer (LET) in CdZnTe (7.28 MeV/cm) [74], the estimated electron cloud is expected to be uniform across the line.

Muon interaction waveforms were acquired from a long measurement due to the low natural flux. These events could be easily discriminated from gamma-ray events due to their high amplitude and unique waveform shapes. As Fig. 7.6 shows, the collecting anode SRF from photoelectric interactions showed rapid increase of amplitude because of the weighting potential profile discussed in Section 2.3. In contrast, the waveform from a muon event increased at a near constant rate because of the linear energy deposition resulted in uniform electron density distributed from the cathode to anode. This behavior can be thought of as many small, gamma-ray charge clouds constantly drifting through the region of rapid weighting potential change near the anode.

Equation 7.5 and Equation 7.6 were used to estimate the electron distributions for muon interactions. The distance regularization coefficient was set to zero, as kinematically muon can generate very extended electron clouds. The smoothing reg-

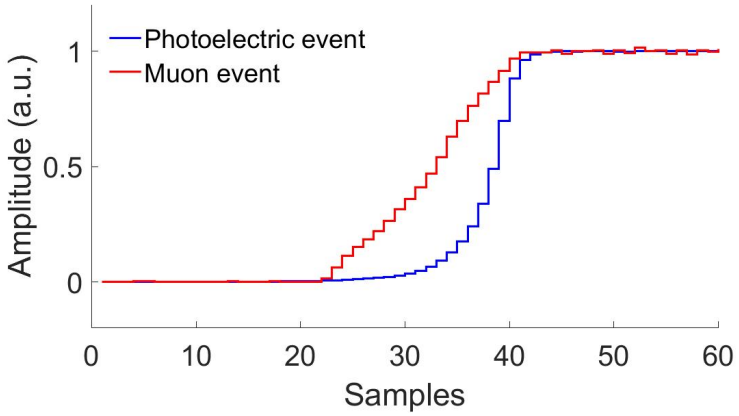

Figure 7.6: Collecting anode SRF from photoelectric interactions in the center of detector and a measured, single-pixel muon event waveform, normalized to their respective maximum amplitudes. The collecting anode gamma ray SRF increased radpidly, due to the small pixel effect, while the muon waveform amplitude increased at near-constant rates due to the unique electron cloud shape.

ularization coefficient was set to 5×10^2 μm^2. The coefficient was not based on a rigorous grid search, as the purpose of this experiment was a proof-of-concept demonstration. Fig. 7.7 shows an example of the estimated electron cloud for a single-pixel muon interaction. The reconstructed electron cloud was uniformly distributed along a line from the cathode to anode side. As discussed in Section 7.3, measured SRFs for subpixel voxels near the anode region have low accuracy. As a result, the reconstructed densities near the anode region were untrustworthy. Overall, the estimated distribution was consistent given how muons slow down in solids.

7.5 Summary

A maximum-likelihood estimation method was re-visited to estimate the electron cloud distributions in 3-D CdZnTe detectors on an event-by-event basis. The ill-posed, inverse problem was solved by quadratic optimization, with physics based regularization terms. These regularization terms were based on preceding expectations of the electron cloud distributions. The regularized optimization method was

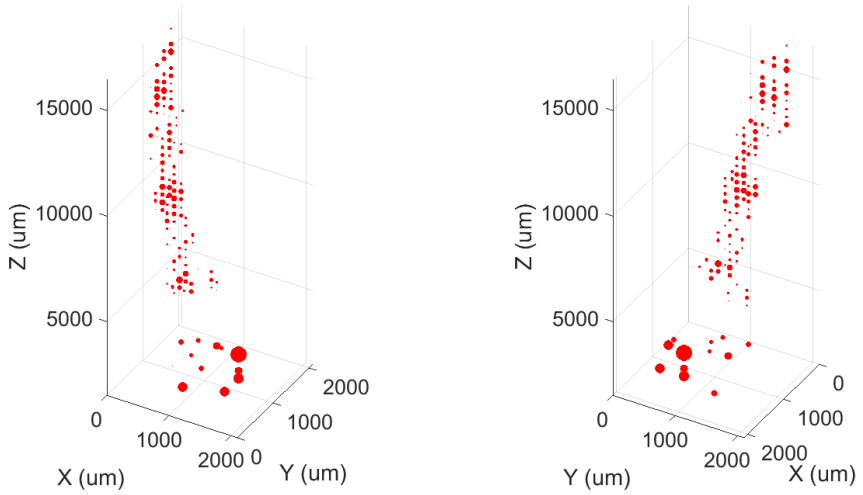

(a) View 1

(b) View 2

Figure 7.7: The electron cloud estimation result for one of the single-pixel muon events, viewed from two perpendicular angles. Each red dot represents the estimated electron charge density in the corresponding position. The larger size of the dot, the larger amount of estimated charge. Near the anode side, the estimation showed several hotspots due to the ill-posedness caused by drastic change of weighting potential for the collecting anode. In the rest region, the estimated charge cloud was uniform and linearly distributed, with a small angle to the Z direction.

then validated on single-pixel muon interactions in 3-D CdZnTe detectors, where the estimated electron clouds agreed with physics based expectations. The framework of MLE and regularized optimization should be easily applicable to all the other digital readout detectors with predictable system responses.

Unfortunately, the current method still faces several significant challenges in digital 3-D CdZnTe detectors. First, the ill-posedness is non-negligible, especially for electron clouds in the anode-region because of the drastic change of weighting potential profiles. Second, when the SRFs are measured, several factors cause a mismatch between the measured SRFs and the true SRFs for each collecting pixel. Both the ill-posedness and the model mismatch problems degrade the accuracy of the estimation method when electronic noise is present. Last but not least, the current method still only works for single-pixel events in 3-D CdZnTe detectors. These issues must be addressed in the future to make the estimation method practically useful.

CHAPTER VIII

Summary and Future Work

Compared with analog systems, the digital systems provide much richer information. Using the simple-subtraction method that is unique to digital systems, the signal amplitudes can be accurately estimated and used for $\mu_e\tau_e$ calculation.

The effects of ambient temperature change on digital 3-D CdZnTe detector systems were investigated. Algorithms were developed to compensate for these effects at as little cost as possible. The temperature-corrected calibrations were used to reconstruct gamma-ray interactions on-the-fly with the ambient temperature changing by up to 30 ^{o}C. These calibraitons showed good performance as well as long-term stability. Further analyses indicate that the resolution degradation in the experiments was from the temperature gradient between the temperature sensor and the readout electronics. This issue should be addressed in the development of future ASICs to achieve better performance.

3-D CdZnTe was tested in varying ambient temperatures. At 40 ^{o}C, 3-D CdZnTe can still demonstrate 0.53% FWHM energy resolution for single-pixel events at 662 keV. The degradation mainly comes from the increase of electronic noise, that is closely related to the leakage current in the detector. It is known that Schottky type contacts can help reduce the leakage in CdZnTe detectors significantly [75]. In the future, this type of contact should be applied to enhance the performance of 3-D

CdZnTe detectors at even higher temperatures.

The effect of fast neutron damage in 3-D CdZnTe detectors was studied in detail. Compared to previous publications, experiments were conducted extensively over a large number of high-performance, digital 3-D CdZnTe detectors. Non-negligible increase of cathode-side events trapping with -3000 V bias was observed with as low as 1E8 n/cm^2 fast neutron fluence and a monotonic trend was observed between the increase of trapping and the neutron fluence. It was observed that the annealing process of neutron damage could be accelerated from several months at room temperature, to several days at 80 ^{o}C. Interestingly, the high-temperature annealing also helped improve the material quality of a detector that was diagnosed as very bad when it was first delivered. In the future, more high-temperature annealing experiments should be conducted on the other detectors with bad material quality to improve their performance, and provide feedback to the detector manufacturers.

For the first time, gamma-ray peaks up to 7 MeV were clearly resolved in 3-D CdZnTe detectors. Using the digital readout systems, the high-energy gamma-ray events were reconstructed and showed energy resolution of about 22 keV FWHM. This value is much higher than the theoretical expectation considering only electronic noise and statistical fluctuations. Several mechanisms were found to degrade the performance of 3-D CdZnTe detectors at high energies. Among them, non-linearity and sub-optimal weighting potential profiles were found to be the main causes. In future ASICs development, better linearity must be required to improve the performance in the high energy range. With the same pixel pitch, larger CdZnTe detectors are expected to provide weighting potentials more suitable for high-energy gamma ray detection. The University of Michigan has already started to collaborate with both eV Products [66] and Redlen [12] to produce $4 \times 4 \times 1.5\,\mathrm{cm}^3$ CdZnTe detectors. These larger detectors should be tested for high-energy gamma-ray detection experiments in the future.

Regularized optimization was used to estimate the electron cloud density in radiation interactions. Single-pixel muon interactions were used to validate the feasibility of this method. However, as Zhu pointed out, electronic noise still affects the performance of this method in this ill-posed problem [18]. As a result, it is still not mature to provide information for better Compton imaging qualities [68]. However, this framework of constrained optimization, with regularization, should be easily applicable to other digital readout, high-performance radiation detectors such as orthogonal-strip HPGe detectors [4] and further improve their position resolution.

APPENDIX

APPENDIX A

Extra Discussions on High-Energy Event Reconstruction

A.1 Two-Pixel Events Results and Analyses

A.1.1 Decomposition of Degradation Mechanisms

Similar to single-pixel events, the 5089 keV, two-pixel events could also be decomposed to evaluate the peak width contribution from each factor. Because of electron cloud size, much more two-pixel events were recorded in the high-energy range compared to single-pixel events. Hence, the analysis could be carried out on a module-by-module basis. Figure A.1 and Figure A.2 present the results for event in Orion-α23, which are representative for the other modules as well. For comparison the 8-keV FWHM of the best single-pixel events at 5089 keV was also included.

In Figure A.1 and Figure A.2, the first several filters "Z>20", "Omit leak" and "Non-edge" have identical meanings to those for single-pixel events in Figure 6.20. It should be noted that "Z>20" was imposed by selecting events with the primary pixel's depth above 20. The primary pixel is the one that has more energy deposition than the other. The reconstructed depth in the secondary pixel is less trustworthy

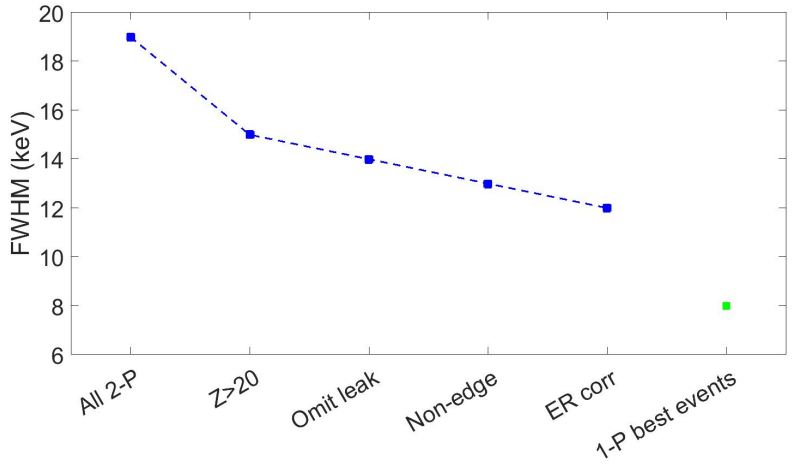

Figure A.1: 5089 keV, two-pixel event energy resolution FWHM, after each additional filtering and correction step.

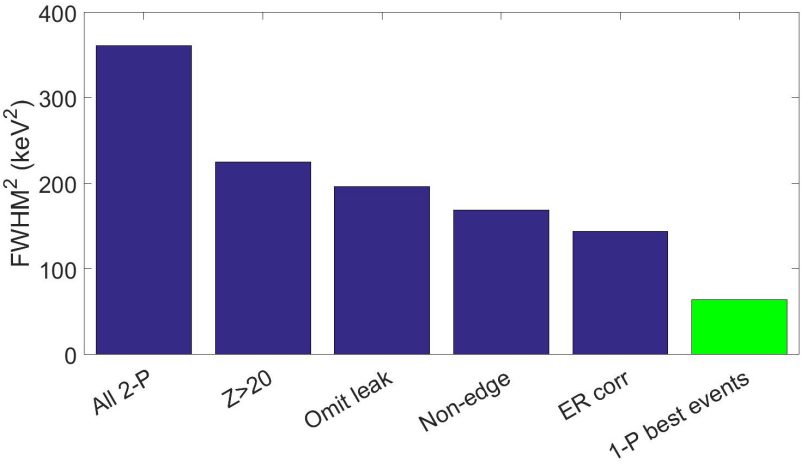

Figure A.2: 5089 keV, two-pixel event energy resolution FWHM, quantified as squared values, after each additional filtering and correction step.

due to WPCT [61]. It could be seen that the most significant resolution improvement still comes from the omission of anode-side (Z<20) events. The last two steps are discussed in detail below.

A.1.2 Energy vs. Energy Ratio

In Figure A.3, "ER" stands for "energy ratio". It is a derived value used to represent physical meanings. ER is calculated by

$$ER = \frac{E_1 - E_2}{E_1 + E_2} \tag{A.1}$$

where E_1 and E_2 represent the reconstructed energy in the primary and secondary pixels in each two-pixel event. $ER = 0$ means that the energy is equally shared by the two pixels, while $ER = 1$ means that all the energy is collected by the primary pixel. Figure A.3 presents the 5089 keV, two-pixel events after the fourth step in Figure A.1 compared against ER. It could be seen that the two-pixel events energy varies as a function of ER. The "ER correction" in the fifth step aligns the peak centroids for different ER values in two-pixel events and the resolution could be improved from 13 keV to 12 keV FWHM.

On the one hand, the "zig-zag" feature in Figure A.3 implies a very high possibility of imperfect non-linearity correction. As mentioned in Section 6.3.4, in the above-2.6 MeV range, only the 4.6-MeV and 5.1-MeV gamma-ray lines were available for non-linearity correction. This means for many two-pixel events the partitioned energy in the two pixels will have sub-optimal non-linearity correction. For instance, In Figure A.3, the slight "dip" at $ER = 0.4$ corresponds to charge sharing events with 3 and 2 MeV in the two adjacent pixels, yet the gamma-ray lines closest to 2 and 3 MeV, used to calibrate the non-linearity, are 1.6, 2.6 and 4.7 MeV. An imperfect non-linearity correction is expected. On the other hand, the trend in Figure A.3 also shows that the 5089 keV, two-pixel events with $ER = 1$ are reconstructed to be several keV

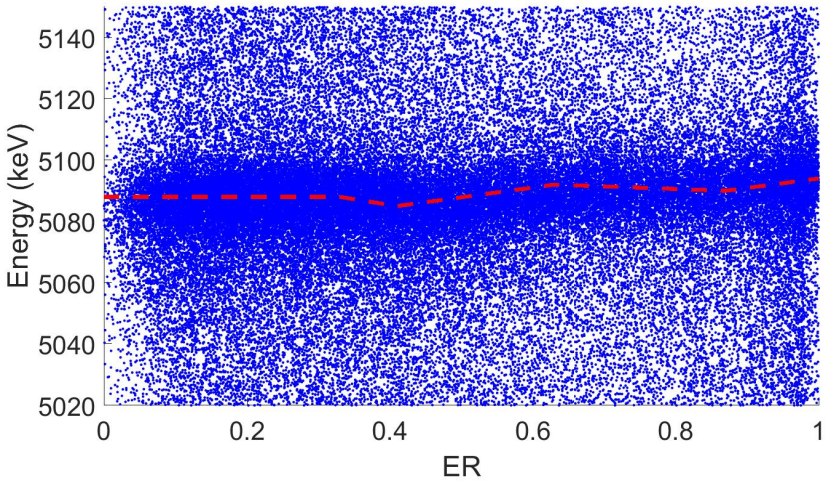

Figure A.3: 5089 keV, two-pixel, cathode-side, no-leak, non-edge events energy VS. ER. Each blue dot represents one event. The red dashed line highlights the peak centroid for varying ER values.

higher in energy compared to those with $ER = 0$. Such a trend is due to imperfect WPCT. A detailed discussion could be seen in [61]. To summarize, the observed systematic variation of two-pixel events energy as a function of ER indicates that the non-linearity correction and WPCT correction are imperfect.

A.1.3 Channel-by-Channel Non-Linearity

With the above analyses, the "best" 5089 keV, two-pixel events show 12 keV FWHM energy resolution. In comparison, Section 6.4 showed that the best 5089 keV, single-pixel events energy resolution is 8 keV FWHM. This difference cannot be explained by the addition of electronic noise in an extra channel. Instead, the hypothesis is that the main reason of this difference is the channel-by-channel non-linearity.

For single-pixel events, the best events reached 8 keV FWHM after peak alignment at 5089 keV. For two-pixel events, however, peak alignment is not feasible because the energy is shared by two pixels and the partitioning could be arbitrary. Unfortunately, there are not enough peaks in the high-energy range to carry out channel-by-channel

non-linearity correction. As a result, the effect of channel-by-channel non-linearity on two-pixel events resolution could only be estimated using simulation.

The simulation assumes that the contribution of peak width from each factor could be modelled as an independent random noise. To further simplify the model the noise is assumed to be a gaussian distribution. Under these assumptions the total peak width could be quantified as the square root of summed FWHMs from all the factors (indexed from 1 to n):

$$FWHM_{total} = \sqrt{\sum_{i=1}^{n} {FWHM_i}^2} \tag{A.2}$$

As Figure A.1 shows the peak alignment at 5089 keV improved the resolution of 5089 keV, single-pixel events from 14 keV to 10 keV FWHM. Hence the FWHM from the noise component corresponding to non-linearity at 5089 keV is about 10 keV based on Equation A.2. Another assumption in this simulation declares that the standard deviation, i.e. the FWHM of the noise component from the channel-by-channel non-linearity is a linear function of the energy in the range of [661.7, 5089] keV:

$$FWHM_{nonL}(E) = \begin{cases} \frac{E-661.7}{5089-661.7}, & \text{if } x < 0. \\ 0, & \text{otherwise.} \end{cases} \tag{A.3}$$

The above equations ignore the channel-by-channel non-linearity for energy below 661.7 keV because each 3-D CdZnTe detector is calibrated at 661.7 keV, and the energy range of [0, 661.7] keV is only a very small fraction of the 7-MeV dynamic range. It should be emphasized again that the model described above is not guaranteed to be true. It is extremely simplified, to give a first-order estimation conveniently.

Figure A.4 presents the histograms of the reconstructed energy in the primary and secondary pixels separately for 5089 keV, two-pixel events in Orion-α23. It could

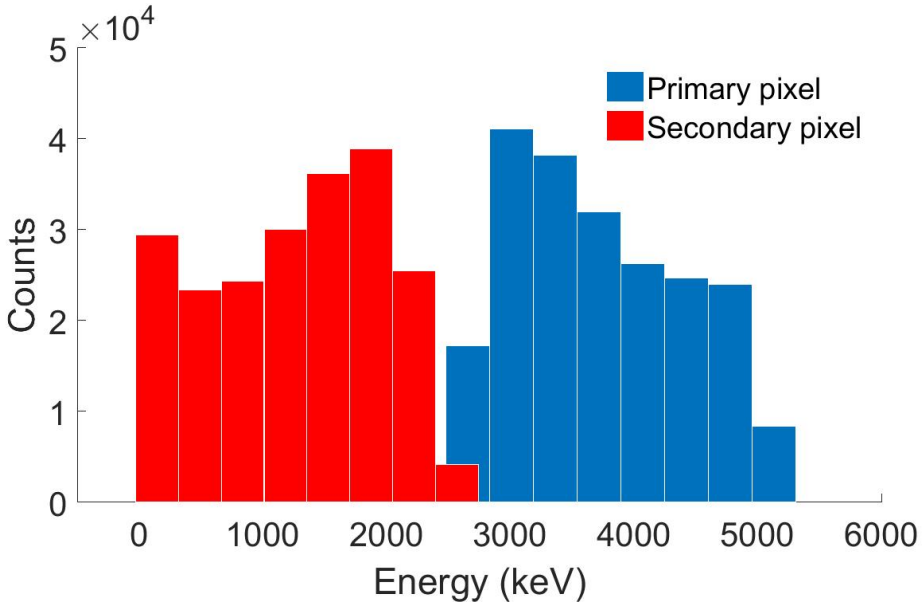

Figure A.4: Histograms of reconstructed in the two pixels separately for 5089 keV, two-pixel events in Orion-α23.

be noticed that not many events had equal energy partitions. This is because the measurement used a hardware threshold above 2.5 MeV to avoid triggering on low-energy events.

The histograms in Figure A.4 could be used as a PDF to randomly sample two-pixel events with various energy partitions. The energies in the two pixels were normalized to make sure the sum was exactly 5089 keV, to exclude any other factors degrading the energy resolution. In each event, a random Gaussian noise was added to each pixel based on the simulated energy deposition. The FWHM of the Gaussian noise was calculated as a function of the energy deposition as Equation A.3 shows. As Figure A.5 shows, in this simulation that only considers channel-by-channel variation of non-linearity, 8.5 keV FWHM is expected. Based on Equation A.2, assuming the 5089 keV, single-pixel best events have 8 keV FWHM resolution and the electronic noise from the extra channel is 3 keV FWHM equivalent, the 5089 keV, two-pixel best events energy resolution is predicted to be 12.05 keV FWHM. This value highly agrees with the measurement results in Figure A.1.

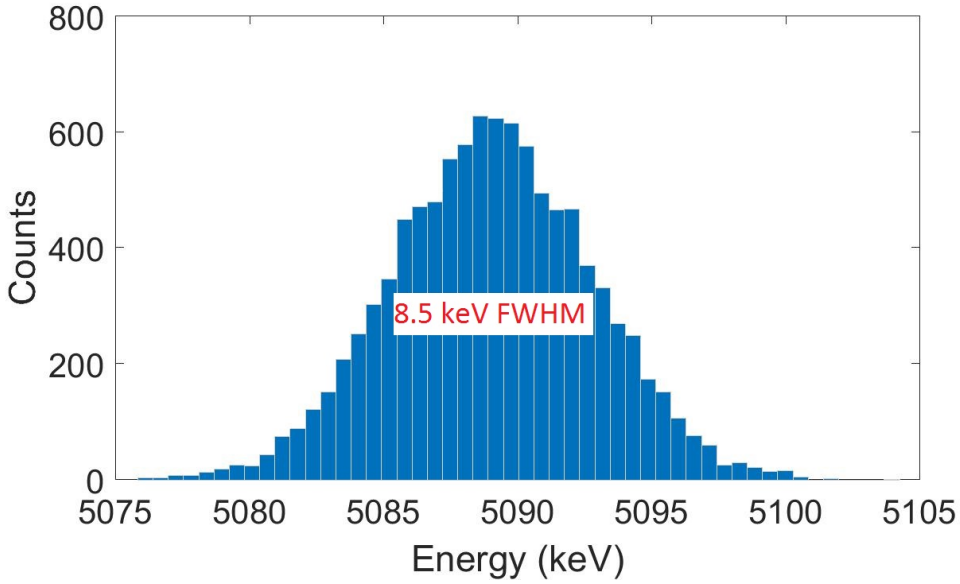

Figure A.5: Simulated 5089 keV, two-pixel events peak width only considering the contribution of channel-by-channel non-linearity variation.

The results from the simplified simulation indicate that for high-energy, two-pixel events, the resolution degradation also comes from multiple factors, while the two main causes are anode-side events resolution degradation, and channel-by-channel non-linearity variation. This is consistent with the error decomposition discussed in Section 6.4 for high-energy, single-pixel events.

BIBLIOGRAPHY

BIBLIOGRAPHY

[1] W. Shockley, "Currents to conductors induced by a moving point charge," *Journal of applied physics*, vol. 9, no. 10, pp. 635–636, 1938.

[2] S. Ramo, "Currents induced by electron motion," *Proceedings of the IRE*, vol. 27, no. 9, pp. 584–585, 1939.

[3] Z. He, "Review of the shockleyramo theorem and its application in semiconductor gamma-ray detectors," *Nucl. Inst. Meth. Phys. Res. A.*, vol. 463, no. 12, pp. 250 – 267, 2001.

[4] M. Amman *et al.*, "Three-dimensional position sensing and "eld shaping in orthogonal-strip germanium gamma-ray detectors," *Nucl. Instrum. and Meth. Phys. Res. Sect. A Accel. Spectrometers, Detect. Assoc. Equip.*, vol. 452, pp. 155–166, 2000.

[5] I. Abt *et al.*, "Pulse shape simulation for segmented true-coaxial HPGe detectors," *Eur. Phys. J. C.*, vol. 68, pp. 609–618, 2010.

[6] O. Frisch, "British atomic energy report br-49," *Atomic Energy Research Establishment: Harwell, UK*, 1944.

[7] Y. Eisen, "Current state-of-the-art industrial and research applications using room-temperature cdte and cdznte solid state detectors," *Nuclear Instruments and Methods in Physics Research Section A: Accelerators, Spectrometers, Detectors and Associated Equipment*, vol. 380, no. 1-2, pp. 431–439, 1996.

[8] P. Luke, "Unipolar charge sensing with coplanar electrodes-application to semiconductor detectors," *IEEE Trans. on Nucl. Sci.*, vol. 42, no. 4, pp. 207–213, 1995.

[9] Z. He, G. F. Knoll, D. K. Wehe, R. Rojeski, C. H. Mastrangelo, M. Hammig, C. Barrett, and A. Uritani, "1-d position sensitive single carrier semiconductor detectors," *Nucl. Instrum. and Meth. Phys. Res. Sect. A Accel. Spectrometers, Detect. Assoc. Equip.*, vol. 380, no. 1-2, pp. 228–231, 1996.

[10] A. Bolotnikov, J. Butcher, G. Camarda, Y. Cui, G. De Geronimo, J. Fried, R. Gul, P. Fochuk, M. Hamade, A. Hossain, *et al.*, "Array of virtual frisch-grid czt detectors with common cathode readout for correcting charge signals and

rejection of incomplete charge-collection events," *IEEE Trans. on Nucl. Sci.*, vol. 59, no. 4, pp. 1544–1551, 2012.

[11] Z. He, W. Li, G. Knoll, D. Wehe, J. Berry, and C. Stahle, "3-d position sensitive cdznte gamma-ray spectrometers," *Nucl. Instrum. and Meth. Phys. Res. Sect. A Accel. Spectrometers, Detect. Assoc. Equip.*, vol. 422, no. 1-3, pp. 173–178, 1999.

[12] "Redlen." `http://redlen.ca/`. Accessed: 2019-02-28.

[13] M. Streicher, *Applications of dgitized 3-D position-sensitive CdZnTe spectrometers for national security and nuclear nonproliferation*. PhD thesis, University of Michigan, 2017.

[14] H. Chen, S. Awadalla, K. Iniewski, P. Lu, F. Harris, J. Mackenzie, T. Hasanen, W. Chen, R. Redden, G. Bindley, *et al.*, "Characterization of large cadmium zinc telluride crystals grown by traveling heater method," *Journal of Applied Physics*, vol. 103, no. 1, p. 014903, 2008.

[15] J. Chu, *Advanced imaging algorithms with position-sensitive gamma-ray detectors*. PhD thesis, University of Michigan, 2018.

[16] "ANSYS." `https://www.ansys.com/`. Accessed: 2019-02-21.

[17] J. D. Eskin, H. H. Barrett, H. B. Barber, and J. M. Woolfenden, "The effect of pixel geometry on spatial and spectral resolution in a cdznte imaging array," in *Nucl. Sci. Symp. and Med. Imag. Conf. Rec., 1995., 1995 IEEE*, vol. 1, pp. 544–548, IEEE, 1995.

[18] Y. Zhu, *Digital signal processing methods for pixelated 3-D position sensitive room-temperature semiconductor detectors*. PhD thesis, University of Michigan, 2012.

[19] W. Li *et al.*, "A data acquisition and processing system for 3-D position sensitive CZT gamma-ray spectrometers," *IEEE Trans. on Nucl. Sci.*, vol. 46, pp. 1989–1994, 1999.

[20] "IDEAS." `https://ideas.no/`. Accessed: 2019-02-07.

[21] F. Zhang *et al.*, "Improved resolution for 3-D position sensitive CdZnTe spectrometers," *IEEE Trans. on Nucl. Sci.*, vol. 51, pp. 2427–2431, 2004.

[22] F. Zhang *et al.*, "New readout electronics for 3-D position sensitive CdZnTe/HgI_2 detector arrays," *IEEE Trans. on Nucl. Sci.*, vol. 53, pp. 3021–3027, 2006.

[23] F. Zhang *et al.*, "A prototype three-dimensional position sensitive CdZnTe detector array," *IEEE Trans. on Nucl. Sci.*, vol. 54, pp. 843–848, 2007.

[24] F. Zhang *et al.*, "Characterization of the H3D ASIC readout system and 6.0 cm 3-D position sensitive CdZnTe detectors," *IEEE Trans. on Nucl. Sci.*, vol. 59, pp. 236–242, 2012.

[25] G. F. Knoll, *Radiation detection and measurement*. John Wiley & Sons, 2010.

[26] P.-L. Hsu and H. Robbins, "Complete convergence and the law of large numbers," *Proceedings of the National Academy of Sciences of the United States of America*, vol. 33, no. 2, p. 25, 1947.

[27] F. Zhang, *Events reconstruction in 3-D position sensitive CdZnTe gamma-ray spectrometers*. PhD thesis, University of Michigan, 2005.

[28] J. J. Moré, "The levenberg-marquardt algorithm: implementation and theory," in *Numerical analysis*, pp. 105–116, Springer, 1978.

[29] Y. Zhu *et al.*, "Sub-pixel position sensing for pixelated, 3-D position sensitive, wide band-gap, semiconductor, gamma-ray detectors," *IEEE Trans. on Nucl. Sci.*, vol. 58, pp. 1400–1409, 2011.

[30] Z. He, W. Li, G. Knoll, D. Wehe, J. Berry, and C. Stahle, "3-d position sensitive cdznte gamma-ray spectrometers," *Nuclear Instruments and Methods in Physics Research Section A: Accelerators, Spectrometers, Detectors and Associated Equipment*, vol. 422, no. 1-3, pp. 173–178, 1999.

[31] W. Kaye, *Energy and position reconstruction in pixelated CdZnTe detectors*. PhD thesis, University of Michigan, 2012.

[32] H. Yang, *Applications of digital ASIC array system for noise analysis, nonlinearity correction, event classification and reconstruction*. PhD thesis, University of Michigan, 2013.

[33] W. Koehler *et al.*, "A correction factor to the two-bias method for determining mobility-lifetime products in pixelated detectors," *IEEE Trans. on Nucl. Sci.*, vol. 63, pp. 1832–1838, 2016.

[34] W. Koehler *et al.*, "Quantification of the conditioning phase in cooled pixelated TlBr detectors," *IEEE Trans. on Nucl. Sci.*, vol. 62, pp. 1785–1790, 2015.

[35] Y. A. Boucher, *Analysis of cadmium zinc telluride detector performance and characteristics for applications in gamma-ray imaging spectrometers.* PhD thesis, University of Michigan, 2013.

[36] B. W. Loo, F. S. Goulding, and D. Gao, "Ballistic deficits in pulse shaping amplifiers," *IEEE Transactions on Nuclear Science*, vol. 35, no. 1, pp. 114–118, 1988.

[37] J. Xia, M. Streicher, Y. Zhu, and Z. He, "Measurement of electron mobility-lifetime product in 3-d position-sensitive cdznte detectors using the vad_umv2. 2 digital readout system," *IEEE Transactions on Nuclear Science*, vol. 65, no. 11, pp. 2834–2837, 2018.

[38] Z. He, G. Knoll, and D. K. Wehe, "Direct measurement of product of the electron mobility and mean free drift time of CdZnTe semiconductors using position sensitive single polarity charge sensing detectors," *J. of Appl. Phys.*, vol. 84, no. 10, pp. 5566–5569, 1998.

[39] Y. Boucher, F. Zhang, W. Kaye, and Z. He, "New measurement technique for the product of the electron mobility and mean free drift time for pixelated semiconductor detectors," *Nucl. Instrum. and Meth. Phys. Res. Sect. A Accel. Spectrometers, Detect. Assoc. Equip.*, vol. 671, pp. 1–5, 2012.

[40] J. Mann, *Improving Cadmium Zinc Telluride Spectrometer Performance and Capabilities*. PhD thesis, University of Michigan, 2016.

[41] G. H. Golub and C. Reinsch, "Singular value decomposition and least squares solutions," in *Linear Algebra*, pp. 134–151, Springer, 1971.

[42] J. Xia, Y. Zhu, and Z. He, "Efficient temperature corrections for gamma-ray energy reconstruction in 3-d position-sensitive cdznte detectors," *Nuclear Instruments and Methods in Physics Research Section A: Accelerators, Spectrometers, Detectors and Associated Equipment*, 2018.

[43] "Thermotron." `https://thermotron.com/`. Accessed: 2019-03-04.

[44] J. Franc, P. Höschl, E. Belas, R. Grill, P. Hlıdek, P. Moravec, and J. Bok, "Cdte and cdznte crystals for room temperature gamma-ray detectors," *Nuclear Instruments and Methods in Physics Research Section A: Accelerators, Spectrometers, Detectors and Associated Equipment*, vol. 434, no. 1, pp. 146–151, 1999.

[45] T. G. Goodwillie, "Calculus iii: Taylor series," *Geometry & Topology*, vol. 7, no. 2, pp. 645–711, 2003.

[46] K. Kim, S. Hwang, P. Fochuk, L. Nasi, A. Zappettini, A. Bolotnikov, and R. James, "The effect of low-temperature annealing on a cdznte detector," *IEEE Transactions on Nuclear Science*, vol. 63, no. 4, pp. 2278–2282, 2016.

[47] "Redlen." `https://iseg-hv.com/en`. Accessed: 2019-02-28.

[48] Y. Eisen and A. Shor, "Fast neutron damage of a pixelated cdznte gamma ray spectrometer," *IEEE Transactions on Nuclear Science*, vol. 56, no. 4, pp. 1700–1705, 2009.

[49] L. M. Bartlett, C. M. Stahle, P. K. Shu, L. M. Barbier, S. D. Barthelmy, N. A. Gehrels, J. F. Krizmanic, P. Kurczynski, D. M. Palmer, A. M. Parsons, *et al.*, "Radiation damage and activation of cdznte by intermediate energy neutrons," in *Hard X-Ray/Gamma-Ray and Neutron Optics, Sensors, and Applications*, vol. 2859, pp. 10–17, International Society for Optics and Photonics, 1996.

[50] Z. He, G. F. Knoll, and D. K. Wehe, "Direct measurement of product of the electron mobility and mean free drift time of cdznte semiconductors using position sensitive single polarity charge sensing detectors," *Journal of Applied Physics*, vol. 84, no. 10, pp. 5566–5569, 1998.

[51] L. S. Varnell, W. A. Mahoney, E. L. Hull, J. F. Butler, and A. Wong, "Radiation effects in cdznte gamma-ray detectors produced by 199-mev protons," in *Gamma-Ray and Cosmic-Ray Detectors, Techniques, and Missions*, vol. 2806, pp. 424–432, International Society for Optics and Photonics, 1996.

[52] I. Kuvvetli, C. Budtz-Jørgensen, U. Korsbech, and H. Jensen, "Radiation damage measurements on czt drift strip detectors," *Nuclear Instruments and Methods in Physics Research Section A: Accelerators, Spectrometers, Detectors and Associated Equipment*, vol. 512, no. 1-2, pp. 98–105, 2003.

[53] C. Moss, C. Hollas, G. McKinney, and W. Myers, "Comparison of active interrogation techniques," in *IEEE Nuclear Science Symposium Conference Record, 2005*, vol. 1, pp. 329–332, IEEE, 2005.

[54] W. Bertozzi, J. A. Caggiano, W. K. Hensley, M. S. Johnson, S. Korbly, R. Ledoux, D. P. McNabb, E. Norman, W. H. Park, and G. A. Warren, "Nuclear resonance fluorescence excitations near 2 mev in u 235 and pu 239," *Physical Review C*, vol. 78, no. 4, p. 041601, 2008.

[55] J. Smeets, F. Roellinghoff, D. Prieels, F. Stichelbaut, A. Benilov, C. Fiorini, R. Peloso, M. Basilavecchia, T. Frizzi, J. Dehaes, *et al.*, "Prompt gamma imaging with a slit camera for real-time range control in proton therapy," *Physics in Medicine & Biology*, vol. 57, no. 11, p. 3371, 2012.

[56] V. Kiptily, G. Gorini, M. Tardocchi, P. de Vries, F. Cecil, I. Chugunov, T. Craciunescu, M. G. Johnson, D. Gin, V. Goloborod'ko, *et al.*, "Doppler broadening of gamma ray lines and fast ion distribution in jet plasmas," *Nuclear fusion*, vol. 50, no. 8, p. 084001, 2010.

[57] M. Kroupa, C. Granja, Z. Janout, M. Kralik, F. Krejci, A. Owens, S. Pospisil, F. Quarati, J. Solc, and M. Vobecky, "Wide energy range gamma-ray calibration source," *Journal of Instrumentation*, vol. 6, no. 11, p. T11002, 2011.

[58] H. Hughes, H. Egdorf, F. Gallmeier, R. Little, R. Prael, E. Snow, L. Waters, and M. White, "Mcnpx user's manual," tech. rep., TPO-E83-G-UG-X-00001, Rev. 0, 1999.

[59] A. Bolotnikov, G. Camarda, G. Carini, Y. Cui, K. Kohman, L. Li, M. Salomon, and R. James, "Performance-limiting defects in cdznte detectors," *IEEE Transactions on Nuclear Science*, vol. 54, no. 4, pp. 821–827, 2007.

[60] S. Agostinelli, J. Allison, K. a. Amako, J. Apostolakis, H. Araujo, P. Arce, M. Asai, D. Axen, S. Banerjee, G. Barrand, *et al.*, "Geant4a simulation toolkit,"

Nuclear instruments and methods in physics research section A: Accelerators, Spectrometers, Detectors and Associated Equipment, vol. 506, no. 3, pp. 250–303, 2003.

[61] J. C. Kim *et al.*, "Charge sharing in common-grid pixelated cdznte detectors," *Nucl. Instrum. and Meth. Phys. Res. Sect. A Accel. Spectrometers, Detect. Assoc. Equip.*, vol. 654, no. 1, pp. 233–243, 2011.

[62] Z. He *et al.*, "Effects of charge sharing in 3-d position sensitive cdznte gamma-ray spectrometers," *Nucl. Instrum. and Meth. Phys. Res. Sect. A Accel. Spectrometers, Detect. Assoc. Equip.*, vol. 439, no. 2-3, pp. 619–624, 2000.

[63] "STAT ONLINE." `https://onlinecourses.science.psu.edu/statprogram/reviews/statistical-concepts/hypothesis-testing`. Accessed: 2019-04-30.

[64] B. Efron, "Bootstrap methods: another look at the jackknife," in *Breakthroughs in statistics*, pp. 569–593, Springer, 1992.

[65] F. Zhang, W. R. Kaye, and Z. He, "Performance of 3-d position sensitive cdznte detectors for gamma-ray energies above 1 mev," in *2009 IEEE Nuclear Science Symposium Conference Record (NSS/MIC)*, pp. 2012–2016, IEEE, 2009.

[66] "Redlen." `https://www.kromek.com/`. Accessed: 2019-02-28.

[67] S. Taherion, H. Chen, P. Lu, S. Awadalla, and G. Bindley, "Optimizing the design parameters of adhesively bonded assemblies to enhance reliability and performance of the czt detectors," in *IEEE Nuclear Science Symposuim & Medical Imaging Conference*, pp. 3956–3958, IEEE, 2010.

[68] D. H. Chivers, A. Coffer, B. Plimley, and K.Vetter, "Impact of measuring electron tracks in high-resolution scientific charge-coupled devices within compton imaging systems," *Nucl. Instrum. and Meth. Phys. Res. Sect. A Accel. Spectrometers, Detect. Assoc. Equip.*, vol. 654, pp. 244–249, 2011.

[69] T. Gleixner, M. Filipenko, G. Anton, T. Ziegler, and T. Michel, "Rejection of alpha-particle background for neutrinoless double beta decay search with pixel detectors," *Journal of Instrumentation*, vol. 9, no. 10, p. P10015, 2014.

[70] S. Boyd and L. Vandenberghe, *Convex optimization*. Cambridge university press, 2004.

[71] "MATLAB." `https://www.mathworks.com/products/matlab.html`. Accessed: 2019-02-25.

[72] "CPLEX Optimizer — IBM." `https://www.ibm.com/analytics/cplex-optimizer`. Accessed: 2019-02-26.

[73] S. I. Kabanikhin, "Definitions and examples of inverse and ill-posed problems," *Journal of Inverse and Ill-posed Problems*, vol. 16, no. 4, pp. 317–357, 2008.

[74] C. Oldorf, *Operation of CdZnTe Semiconductor Detectors in Liquid Scintillator for the COBRA Experiment*. PhD thesis, Hamburg University, 2015.

[75] A. E. Bolotnikov, S. E. Boggs, C. H. Chen, W. R. Cook, F. A. Harrison, and S. M. Schindler, "Properties of pt schottky type contacts on high-resistivity cdznte detectors," *Nuclear Instruments and Methods in Physics Research Section A: Accelerators, Spectrometers, Detectors and Associated Equipment*, vol. 482, no. 1-2, pp. 395–407, 2002.